TECHNISCHE UNIVERSITÄT WIEN

DISSERTATION

Cavity Quantum Electrodynamics with Spin Ensembles: From the Semiclassical to the Quantum Regime

Ausgeführt zum Zwecke der Erlangung des akademischen Grades eines
Doktors der technischen Wissenschaften

unter der Leitung von
Privatdoz. Dr. rer. nat. Dmitry Krimer
und
Univ.-Prof. Dipl.-Ing. Dr. techn. Stefan Rotter
Institut für Theoretische Physik, E136

eingereicht an der
Technischen Universität Wien
Fakultät für Physik

von
Dipl.-Ing. Matthias Zens
Matr.-Nr. 0826022

_____   _____
Datum   Unterschrift

Erklärung zur Verfassung der Arbeit

Dipl.-Ing. Matthias Zens
Schelleingasse 26/3/21, 1040 Wien

Hiermit erkläre ich, dass ich diese Arbeit selbständig verfasst habe, dass ich die verwendeten Quellen und Hilfsmittel vollständig angegeben habe und, dass ich die Stellen der Arbeit - einschließlich Tabellen, Karten und Abbildungen -, die anderen Werken oder dem Internet im Wortlaut oder dem Sinn nach entnommen sind, auf jeden Fall unter Angabe der Quelle als Entlehnung kenntlich gemacht habe.

_____   _____
Ort, Datum   Unterschrift Dipl.-Ing. Matthias Zens

Abstract in german - Deutsche Kurzfassung

Spinensembles in einem Resonator bilden Schnittstellen zwischen Licht und Materie und spielen eine tragende Rolle bei der Entwicklung zukünftiger quantentechnologischer Bauelemente. Ein offenkundiger Vorteil ensemblebasierter Systeme ist die kollektive Verstärkung der Kopplungsstärke, welche eine starke Wechselwirkung zwischen den Licht- und Materiekomponenten ermöglicht. Besonders vielversprechend dabei sind Spinensembles in Festkörpern wie Stickstoff-Fehlstellen in Diamant, Phosphor-Atome in Silizium oder mit Seltenen Erden dotierte Kristalle aufgrund ihrer einfachen Handhabung und Integrierbarkeit. Solche Systeme sind jedoch fast zwangsläufig inhomogen verbreitert, da die verschiedenen Spins des Ensembles unterschiedliche lokale Umgebungen aufweisen, was zu einer spektralen Verteilung ihrer Übergangsfrequenzen führt. Diese sogenannte inhomogene Verbreiterung ist eine Hauptquelle für Dekohärenz in Festkörpersystemen und eine große Herausforderung für zukünftige technische Anwendungen.

In dieser Arbeit soll der notwendige theoretische Rahmen geschaffen werden um verschiedene Effekte von inhomogen verbreiterten Spinensemblen, die an eine einzelne Resonatormode gekoppelt sind und in zahlreichen quantenoptischen Systemen in sehr unterschiedlichen Parameterbereichen realisiert wurden, zu beschreiben und zu verstehen.

Für makroskopische Spinensembles, d.h. Ensembles, die aus einer großen Anzahl an Spins bestehen, können Quantenfluktuationen der einzelnen Spins typischerweise vernachlässigt werden, was eine semiklassische Beschreibung auf Basis der Maxwell-Bloch-Gleichungen ermöglicht. Hier untersuchen wir zwei prominente nichtlineare Effekte: optische Bistabilität, die einem Phasenübergang erster Ordnung entspricht, und kritische Verlangsamung. Insbesondere zeigen wir, dass das Einsetzen der Bistabilität nicht nur von der Breite der spektralen Spinverteilung abhängt, sondern auch stark von deren Form. Des Weiteren analysieren wir die Zeitdauer mit der sich die Resonatoramplitude ihrem stationären Zustand annähert. In der Nähe eines Phasenübergangs divergieren diese Einschwingzeiten exponentiell. Wir zeigen diese kritische Verlangsamung in einer Zusammenarbeit mit einem Experiment durchgeführt unter der Leitung von Jörg Schmiedmayer am Atominstitut der Technischen Universität Wien. Dabei wurden negativ geladenen Stickstoff-Fehlstellen in Diamant stark an einen supraleitenden Mikrowellenresonator gekoppelt und Einschwingzeiten von bis zu 11 Stunden beobachtet.

In mesoskopischen Spinensembles mit einer moderaten Anzahl von Spins werden Quantenfluktuationen wichtig und semiklassische Methoden versagen. Mit Hilfe einer Kumulanten-Entwicklung untersuchen wir den Übergang zwischen dem semiklassischen und dem quantenmechanischen Regime für inhomogen verbreiterte Spinensembles in einem Resonator. Darüber hinaus entwickeln wir eine zeitadaptive Methode basierend auf der Dichtematrix-Renormierungsgruppe, um die vollständige Quantendynamik von Spinensembles mit bis zu hundert Spins berechnen zu können. Mit Hilfe dieser Methode untersuchen wir mesoskopische Spinensembles, deren Spin-Verteilungen eine kammförmige Struktur bilden. Diese sogenannten atomaren Frequenzkämme haben vielversprechende Eigenschaften für Quantenspeicher. Zum einen zeigen wir, dass beliebige Multiphotonen-Zustände durch das kammförmige Spinensemble absorbiert und in periodischen Zeitabständen wieder in den Resonator emittiert werden. Zum anderen lässt sich mit einem solchen Spinensemble ein kohärenter Eingangspuls in eine periodische Serie von nicht-klassischen Lichtpulsen umwandeln.

Schließlich befassen wir uns mit Spin-Echos, die sowohl in der Kernspinresonanz als auch in der Elektronenspinresonanz eine fundamentale Rolle spielen. Insbesondere übertragen wir das Hahn-Echo in den Bereich der starken Kopplung, wo wir ein neues dynamisches Phänomen vorfinden, nämlich eine Folge von selbsterhaltenden periodischen Echos nach einer konventionellen Hahn-Echo-Sequenz. In Zusammenarbeit mit einem Experiment durchgeführt unter der Leitung von Hans Hübl an der Technischen Universität München, präsentieren wir die erste Realisierung dieser faszinierenden Multiecho-Signatur in einem Elektronenspinresonanz-Experiment mit Phosphor Atomen in Silizium.

Abstract

Spin ensembles inside a cavity act as light-matter interfaces that play an eminent role in the development of future quantum devices. An apparent asset of ensemble-based systems is the collective enhancement of the coupling strength, facilitating a strong interaction between the light and matter components. Particularly promising in this regard, due to their convenient handling and integrability, are solid state spin ensembles such as nitrogen-vacancy centers in diamond, phosphorous donors in silicon, or rare earth doped crystals. Such ensemble-based setups, however, are almost inevitably inhomogeneously broadened as the different spins of the ensemble typically have different local environments leading to a spectral distribution in their transition frequencies. This so-called inhomogeneous broadening is a major source for decoherence in solid state systems and a major challenge to be addressed for future technical applications.

In this thesis, we aim to provide the theoretical framework necessary to describe and understand various effects of inhomogeneously broadened spin ensembles coupled to a single-mode cavity—a system that has been realized in numerous different quantum optical setups and in very different parameter regimes.

For macroscopic spin ensembles, i.e., ensembles consisting of a vast number of spins, quantum fluctuations of the individual spins can typically be neglected, allowing a semiclassical description based on Maxwell-Bloch equations. Here, we study two prominent effects in the strongly nonlinear regime namely optical bistability, resembling a first-order phase transition, and critical slowing down. In particular, we show that the onset of bistability not only depends on the width of the spectral spin distribution but also strongly depends on its exact shape. Furthermore, we analyze the transient times of the cavity amplitude which show a power-law divergence when an external parameter is changed in the vicinity of the phase transition. This critical slowdown is demonstrated in collaboration with the group of Jörg Schmiedmayer at the Atominstitut of TU Wien. In the experiment, negatively charged nitrogen vacancy centers in diamond are strongly coupled to a superconducting microwave resonator showing transient times of up to 11 hours.

In mesoscopic spin ensembles with moderate numbers of constituents, quantum fluctuations gain importance, and semiclassical methods fail. We study this crossover between the semiclassical and the quantum regime using a cumulant expansion approach to study the semiclassical-to-quantum boundary for inhomogeneously broadened spin ensembles inside a cavity. In addition, we develop a time-adaptive variational renormalization group method to calculate the full quantum

dynamics of spin ensembles containing up to one hundred spins. With the aid of this method, we examine mesoscopic spin ensembles whose spin distributions form a comb-shaped structure. These so-called atomic frequency combs have promising properties for the storage of quantum information. On the one hand, we show that arbitrary multi-photon states are absorbed by the comb-shaped spin ensemble and re-emitted into the cavity at periodic time intervals. On the other hand, we demonstrate that by means of such a spin ensemble a coherent input pulse can be converted into periodic pulses of non-classical light.

Finally, we address spin echoes, which are a fundamental part in nuclear magnetic resonance as well as in electron spin resonance. Specifically, we transfer the Hahn echo to the strong coupling regime, where we find a new dynamical phenomenon featuring a periodic sequence of self-sustained echoes after a conventional Hahn echo pulse. In collaboration with the group of Hans Hübl at the Technical University Munich, a first demonstration of this intriguing multiecho signature is presented in an electron spin resonance experiment with phosphorus donors in silicon.

List of Publications

Publications covered in this thesis:

1. D. O. Krimer, M. Zens, S. Putz, and S. Rotter, "Sustained Photon Pulse Revivals from Inhomogeneously Broadened Spin Ensembles", *Laser & Photonics Reviews* 10, 1023 (2016).

2. A. Angerer, S. Putz, D. O. Krimer, T. Astner, M. Zens, R. Glattauer, K. Streltsov, W. J. Munro, K. Nemoto, S. Rotter, J. Schmiedmayer, and J. Majer, "Ultralong Relaxation Times in Bistable Hybrid Quantum Systems", *Science Advances* 3, e1701626 (2017).

3. H. S. Dhar, M. Zens, D. O. Krimer, and S. Rotter, "Variational Renormalization Group for Dissipative Spin-Cavity Systems: Periodic Pulses of Nonclassical Photons from Mesoscopic Spin Ensembles", *Physical Review Letters* 121, 133601 (2018).

4. D. O. Krimer, M. Zens, and S. Rotter, "Critical Phenomena and Nonlinear Dynamics in a Spin Ensemble Strongly Coupled to a Cavity. I. Semiclassical Approach", *Physical Review A* 100, 013855 (2019).

5. M. Zens, D. O. Krimer, and S. Rotter, "Critical Phenomena and Nonlinear Dynamics in a Spin Ensemble Strongly Coupled to a Cavity. II. Semiclassical-to-Quantum Boundary", *Physical Review A* 100, 013856 (2019).

6. S. Weichselbaumer, M. Zens, C. W. Zollitsch, M. S. Brandt, S. Rotter, R. Gross, and H. Huebl, "Echo Trains in Pulsed Electron Spin Resonance of a Strongly Coupled Spin Ensemble", *Physical Review Letters* 125, 137701 (2020).

7. M. Zens, D. O. Krimer, H. S. Dhar, and S. Rotter, "Periodic cavity state revivals from atomic frequency combs", *arXiv:*2107.05919 [quant-ph](2021). *currently under review at Physical Review Letters.*

Further contributions:

8. M. Zens and S. Rotter, "Superabsorption by time-reversing superradiance", (Invited News & Views article) *Nature Photonics* 15, 251-252 (2021).

Contents

Introduction

Cavity quantum electrodynamics (cavity QED) is the quantum theory of the interactions between light and matter inside a cavity. The origins of this field date back to the pioneering work of Purcell in the 1940s [1], realizing that coupling a spin system to a resonant electrical circuit can dramatically enhance the spontaneous emission rate of the spins. Following the first experiments with fluorescent molecules near a metallic mirror [2], both the enhancement and inhibition of spontaneous emission were demonstrated for atoms inside a cavity [3–5].

By selecting particular electromagnetic modes, the cavity enables a significant simplification in the theoretical treatment compared to conventional QED in free space. In 1963, Jaynes and Cummings introduced an exactly solvable model [6], describing the interaction of one atom with a single mode of the quantized field. This model, which now bears their name, became the paradigm model of cavity QED, describing numerous quantum optical phenomena [7]. Even more importantly, the cavity enables the control and a significant enhancement of the light-matter interaction. Cavity QED, therefore, became not only an ideal testing ground for fundamental physics [8–12] but also an invaluable tool for technological applications [13–15], especially concerning quantum information processing [16–18] with hybrid quantum systems [19, 20].

Hybrid quantum systems aim to combine the complementary functionalities of different quantum systems, e.g., photons, which are well suited for transmitting quantum information [21], and spins serving as long-lived quantum memories [22]. The cavity, in turn, acts as an interface or "quantum bus" for the input and output of information [19]—connecting light and matter. A prerequisite in this regard is the coherent exchange of information between the individual subsystems enabled by the so-called strong coupling regime [23, 24]. As the light-matter coupling strength exceeds all dissipation rates of the system, the atoms or spins can reabsorb an emitted photon before it is lost to the environment. Ultimately, this leads to coherent oscillations in the atomic excitations, known as quantum Rabi oscillations [25, 26], and a pair of resolvable peaks in the cavity transmission spectrum (polaritonic peaks), known as vacuum Rabi splitting [27]. The strong coupling condition, $\Omega \gg \kappa, \gamma_h, \gamma_p$, where Ω denotes the light-matter coupling strength and κ, γ_h, and γ_p describe various decay rates of the system, meanwhile has been realized in numerous physical setups, including single molecules in plasmonic nanocavities [28, 29], artificial atoms based on superconducting qubits [30, 31] and quantum dots [32], as well as solid-state spin ensembles [33–44].

In this thesis, we consider ensemble-based systems of which the most prominent representatives are negavitely charged nitrogen-vacancy (NV) defects in diamond [34–39], rare-earth doped crystals [42–44], and clouds of cold atoms [45, 46]. While our methods are general and widely applicable, we will mainly consider concrete experimental realizations with solid-state spin ensembles like NV centers in diamond [39] or phosphorus donors in silicon [41].

Ensembles of emitters, be they atoms, spins, or molecules, play an integral role in cavity QED and generally in quantum optics due to the cooperative enhancement of the coupling, which was noted already by Dicke in his seminal treatment of superradiance [47]. For a homogeneous ensemble of emitters inside a cavity, the collective coupling strength reads [36] $\Omega = g\sqrt{N}$, where N is the number of emitters in the ensemble and g their individual coupling strength. This cooperative enhancement is essential in many physical platforms to actually reach the strong coupling regime [33–42, 45, 46, 48]. Naturally, however, the individual constituents in an ensemble have slightly different local environments leading to differences in both their transition frequencies and coupling strengths. This inhomogeneous broadening can act as the main source for dephasing in ensemble-based systems [37, 38], drastically decreasing the coherence time, which plays a central role in restricting their performance in processing and storing quantum information [49–51]. Investigating and understanding the effects of inhomogeneous broadening is, therefore, a central task to overcome or even exploit the associated limitations for future applications [51].

First results in this direction were already made in the 1990s [52] with the remarkable observation that the width of the transmission peaks of a strongly coupled spin ensemble can be much narrower than expected from its inhomogeneous broadening. Even more remarkably, this effect, which was later called "cavity protection effect", only occurs if the wings of the spectral distribution of the emitters fall off faster than a Lorentzian [53, 54]. The cavity protection effect has been examined experimentally using an ensemble of NV defects in diamond [37], offering exciting prospects for coherent control schemes that allow a significant suppression of decoherence in strongly coupled hybrid quantum systems. Notably, a precise knowledge not only of the width but also the shape of the inhomogeneous spin broadening is crucial for a qualitative and quantitative understanding of this effect [38]. Along similar lines, it has been theoretically proposed [55] to suppress the decoherence of a spin ensemble by modifying the spectral spin distribution through the technique of spectral hole burning. Interestingly, it is sufficient to remove a small fraction of the emitters at well-chosen frequencies to substantially increase the coherence time of the spin-cavity system. This effect has recently been demonstrated in a proof-of-principle experiment [56].

The increasing experimental control in quantum optical experiments and new theoretical concepts, such as coherent spectral hole burning [57, 58], lead the way to create spectrally engineered spin ensembles with new functionalities [59, 60]. Prominent examples in this regard are atomic frequency combs [61, 62], i.e., spin

ensembles with a comb-shaped spectral spin distribution, which show promising features for future quantum memories [62–68].

The retrieval of information from an inhomogeneously broadened spin ensemble is also the central task of spin-echo techniques [69], as used in nuclear magnetic resonance (NMR) [70–72] and electron spin resonance (ESR) [73]. Both of these fundamental spectroscopic techniques are intimately connected with concepts from cavity QED. In particular, the development of superconducting resonators enabled the strong coupling of spin ensembles [33–40] and thereby high-sensitivity applications in ESR [22, 74, 75]. However, a detailed study of the fundamental pulse sequence in NMR and ESR—the Hahn echo [76]—in the strong coupling regime is still missing.

This thesis is divided into two parts. The first part, consisting of chapters 1 to 3, is devoted to the theoretical methods necessary to describe inhomogeneously broadened spin ensembles strongly coupled to a single cavity mode in different regimes. Chapter 1 covers the microscopic description of this system based on the Tavis-Cummings Hamiltonian. In particular, we focus on the driven and dissipative dynamics using a Lindblad master equation and the corresponding equations of motion for expectation values.

In Chapter 2, we introduce a Volterra integral approach and the semiclassical Maxwell-Bloch equations, both very effective methods for macroscopic spin ensembles where quantum fluctuations can be ignored.

Chapter 3 deals with methods for mesoscopic spin ensembles. Here, semiclassical approximations no longer apply and quantum fluctuations have to be taken explicitly into account. We first review the cumulant expansion approach, which allows us to calculate quantum corrections to the semiclassical expectation values. Then, we introduce a time adaptive variational renormalization group method that provides a full quantum description of the mesoscopic spin-cavity system. Note that this is only a selection and by no means an exhaustive list of methods for treating spin ensembles in cavity QED. Methods not covered in this work are, for example, stochastic wave function approaches [77, 78], phase space methods [78, 79], or master equations in the few-excitation limit [80, 81].

In the second part of this thesis, we apply the described methods to examine various effects of inhomogeneously broadened spin ensembles inside a cavity. The majority of recent studies on hybrid quantum systems based on solid-state spin ensembles have been carried out in the linear regime of few excitations [33–38]. In Chapter 4, we go beyond this limitation exploring the nonlinear regime of cavity QED. In particular, we provide a detailed analysis of optical bistability and critical slowing down in the presence of inhomogeneous broadening [82]. Our theoretical findings are augmented by an experimental realization with nitrogen-vacancy centers in diamond [39]. Furthermore, we examine the validity of the semiclassical Maxwell-Bloch equations in the vicinity of the bistable regime and establish a semiclassical-to-quantum boundary for spin ensembles in cavity QED [83].

4

Chapter 5 is devoted to spectrally engineered spin ensembles in the form of atomic frequency combs. Here, we first present the route from single-mode to multimode strong coupling, finding sustained photon pulse revivals from inhomogeneously broadened spin ensembles in the semiclassical regime [84]. Then we provide a fully quantum mechanical treatment of atomic frequency combs coupled to a cavity [85, 86].

Finally, in Chapter 6, we report on a novel phenomenon in electron spin resonance, transferring the conventional Hahn-echo to the strong coupling regime of cavity QED.

Part I.

Methods and theoretical framework

Chapter 1.

Light-matter interaction of spin ensembles inside a cavity

The microscopic description of the interaction between matter in the form of a single two-level system and a single quantized mode of light is given by the famous Jaynes-Cummings Hamiltonian [6]. For a derivation and a review of this fundamental model, we refer to one of the numerous excellent quantum optics textbooks [87–91]. In this chapter, we introduce the Tavis-Cummings Hamiltonian, which is a generalization of the Jaynes-Cummings Hamiltonian for many two-level systems and forms the basis for the rest of the thesis. Furthermore, we present the relevant master equation for the evolution of the open ensemble-cavity system and the corresponding equations of motion for expectation values. The methods for solving these equations are then discussed in the two subsequent chapters.

1.1. Tavis-Cummings Hamiltonian

Our starting point for the physical description of N two-level systems inside a single-mode cavity is the Tavis-Cummings Hamiltonian [92] given by ($\hbar = 1$)

$$H = \omega_c\, a^\dagger a + \frac{1}{2}\sum_{k=1}^{N}\omega_k\sigma_k^z + \sum_{k=1}^{N}[g_k\sigma_k^- a^\dagger + g_k^*\sigma_k^+ a] + i[\eta(t)a^\dagger e^{-i\omega_p t} - \eta^*(t)a e^{i\omega_p t}], \quad (1.1)$$

where $a^\dagger$ and a are the creation and annihilation operators of the single cavity mode satisfying the commutation relation

$$[a, a^\dagger] = 1, \quad (1.2)$$

and σ_k^z, $\sigma_k^+ \equiv (\sigma_k^x + i\sigma_k^y)/2$, $\sigma_k^- \equiv (\sigma_k^x - i\sigma_k^y)/2$ are the Pauli operators corresponding to the individual spins with

$$[\sigma_k^+, \sigma_j^-] = \sigma_k^z\,\delta_{kj} \quad \text{and} \quad [\sigma_k^z, \sigma_j^\pm] = \pm 2\sigma_k^\pm\,\delta_{kj}. \quad (1.3)$$

The first two terms in Eq. (1.1) correspond to the energy of the free cavity field and spin ensemble with frequencies ω_c and ω_k, respectively, while the third term

describes the Jaynes-Cummings type interaction between the individual spins and the cavity mode with coupling strength g_k. Since the two-level systems can absorb any phase by the re-definition $\tilde{\sigma}_k^+ \equiv e^{i\phi}\sigma_k^+$, the phase of the coupling is physically not important. Hence, g_k is often chosen as either real or imaginary for convenience; in this thesis, we use $g_k = g_k^*$. Note that, here, we neglect variations of the field over the dimensions of the spins (dipole approximation) as well as the counter-rotating terms, $\sigma_k^- a$ and $\sigma_k^+ a^\dagger$ (rotating-wave approximation). The latter requires that the coupling between the ensemble and the cavity is small compared to the transition frequencies ω_k. Another implicit assumption is that the spin ensemble is dilute, such that direct dipole-dipole interactions can be neglected. Finally, the last term in Eq. (1.1) is a classical external driving field of amplitude $\eta(t)$ and frequency ω_p, which is injected into the cavity. Without loss of generality, we typically take $\eta(t) = \eta^*(t)$.

It is often convenient to remove the explicit time dependence ($\propto e^{-i\omega_p t}$) of the external driving field by performing a transformation to a rotating frame with respect to the driving frequency ω_p:

$$\tilde{H} = U\,H\,U^\dagger + i\,\frac{\partial U}{\partial t}U^\dagger, \tag{1.4}$$

where

$$U = e^{i\omega_p t\left(a^\dagger a + \sum_k \frac{1}{2}\sigma_k^z\right)} \tag{1.5}$$

is a unitary transformation. After some calculation (see Appendix A), the Tavis-Cummings Hamiltonian in the frame rotating with ω_p is given by

$$\tilde{H} = \Delta_c\,a^\dagger a + \frac{1}{2}\sum_{k=1}^{N}\Delta_k\sigma_k^z + \sum_{k=1}^{N}g_k[\sigma_k^- a^\dagger + \sigma_k^+ a] + i\eta(t)[a^\dagger - a], \tag{1.6}$$

where $\Delta_c \equiv \omega_c - \omega_p$ and $\Delta_k \equiv \omega_k - \omega_p$ is the detuning of the cavity frequency ω_c and of the individual spin frequencies ω_k with respect to the external driving field of frequency ω_p.

It is worth mentioning that the Tavis-Cummings Hamiltonian without external driving belongs to the class of exactly solvable Richardson-Gaudin models [93] and can in principle be solved via a Bethe ansatz technique [94–96]. Since, in this thesis, however, we are dealing with realistic open systems, we will focus on the driven and dissipative dynamics of the spin-cavity system. Below, we present the corresponding master equation approach and the resulting equations of motion for expectation values.

1.2. Open system dynamics

In general, the cavity and spins in the ensemble are lossy due to the inevitable coupling to the surrounding environment. In this thesis, we describe the dynamics of the open spin-cavity system by a Lindblad master equation [97, 98]

$$\frac{d}{dt}\rho(t) = \mathcal{L}[\rho] = -i[H, \rho] + \mathcal{L}_D[\rho], \tag{1.7}$$

where $\rho(t)$ is the density matrix of the spin-cavity system and $\mathcal{L}_D$ is a dissipator given by

$$\mathcal{L}_D[\rho] = \kappa \left(2a\rho a^\dagger - a^\dagger a\, \rho - \rho\, a^\dagger a\right) + \gamma_h \sum_{k=1}^{N}(2\sigma_k^- \rho\, \sigma_k^+ - \sigma_k^+ \sigma_k^- \rho - \rho\, \sigma_k^+ \sigma_k^-)$$

$$+ \gamma_p \sum_{k=1}^{N}(\sigma_k^z \rho\, \sigma_k^z - \rho\,). \tag{1.8}$$

Here, the first term accounts for cavity losses with rate κ; the second term gives the radiative decay of the individual spins with rate γ_h, and the last term describes their non-radiative dephasing with rate $\gamma_p/2$. Note that with the definition of the decay rates in Eq. (1.8), κ corresponds to the half-width-at-half-maximum (HWHM) of the cavity linewidth and the spin decay rates can be related to the longitudinal and transverse decay times $T_1 = 1/(2\gamma_h)$ and $T_2 = 1/(\gamma_h + 2\gamma_p)$, respectively. In addition, it should be noted that we neglect thermal excitations in Eq. (1.8), always assuming $k_B T \ll \hbar\omega_c$, $\hbar\omega_k$.

The derivation of the Lindblad master equation (1.7) can be found in numerous textbooks [97–99] and will not be repeated here. It bases on the fundamental Born-Markov approximation, which is typically very well satisfied for spin-cavity systems. The Born approximation assumes that the combined density matrix of the system and of the environment can be factorized as $\rho_{tot}(t) = \rho(t) \otimes \rho_{env}(0)$, such that the state of the large environment $\rho_{env}(0)$ is not affected by the evolution of $\rho(t)$. The Markov approximation on the other hand assumes that the environment has a very short memory time, i.e., correlations between operators of the environment decay fast compared to the intrinsic time scale of the spin-cavity system.

Since the dimension of the system's Hilbert space grows exponentially with the number of spins, direct solutions of Eq. (1.7) are typically restricted to very few spins ($N \lesssim 10$) [100–102], very few excitations [103–105], or identical spins without inhomogeneous broadening [106–109]. While we will later introduce a method to solve the master equation (1.7) fully quantum mechanically for large spin ensembles of up to one hundred spins, another common approach is to directly solve for the expectation values of operators of interest instead [109–112]. The equation of motion for the expectation value of some operator O can be obtained by multiplying

the master equation (1.7) with O and taking the trace, which gives

$$\frac{d}{dt}\langle O\rangle = \mathrm{Tr}\left(-i[O,H]\rho + O\mathcal{L}_D[\rho]\right). \tag{1.9}$$

For the operators, a, σ_k^-, and σ_k^z, straightforward calculations yield

$$\frac{d}{dt}\langle a\rangle = -(\kappa + i\,\Delta_c)\langle a\rangle - i\sum_{k=1}^{N} g_k\langle\sigma_k^-\rangle + \eta\,, \tag{1.10a}$$

$$\frac{d}{dt}\langle\sigma_k^-\rangle = -(\gamma_h + 2\gamma_p + i\,\Delta_k)\langle\sigma_k^-\rangle + i\,g_k\langle\sigma_k^z a\rangle\,, \tag{1.10b}$$

$$\frac{d}{dt}\langle\sigma_k^z\rangle = -2\gamma_h(\langle\sigma_k^z\rangle + 1) + 2i\,g_k(\langle\sigma_k^- a^\dagger\rangle - \langle\sigma_k^+ a\rangle). \tag{1.10c}$$

We notice that the above set of differential equations is not closed. In particular, the equations of motion for the spin expectation values $\langle\sigma_k^-\rangle$ and $\langle\sigma_k^z\rangle$ depend on the expectation values $\langle\sigma_k^z a\rangle$ and $\langle\sigma_k^- a^\dagger\rangle$, respectively, which involve two operators. In the same way, the equations of motion for expectation values with two operators depend on expectation values with three operators, etc., as can be seen in the example:

$$\frac{d}{dt}\langle\sigma_k^z a\rangle = -\left(\kappa + 2\gamma_h + i\,\Delta_c\right)\langle\sigma_k^z a\rangle - 2\gamma_h\langle a\rangle + \eta\langle\sigma_k^z\rangle - i\sum_{\substack{j=1\\j\neq k}}^{N} g_j\langle\sigma_k^z\sigma_j^-\rangle + ig_k\langle\sigma_k^-\rangle$$
$$+ 2i\,g_k(\langle\sigma_k^- a^\dagger a\rangle - \langle\sigma_k^- a^\dagger a^\dagger\rangle^*\,). \tag{1.11}$$

This corresponds to the Bogoliubov-Born-Green-Kirkwood-Yvon (BBGKY) hierarchy [113], based on the fact that for a system of interacting particles, the dynamic of an expectation value involving n operators depends on expectation values involving $n + 1$ operators. The full set of equations for expectation values up to third-order is presented in Appendix B.

To solve for the corresponding dynamics, this infinite hierarchy of coupled differential equations has to be truncated. In the following two chapters, we discuss different approaches to obtain a closed set of equations for spin ensembles inside a cavity in various physical regimes. In addition, we present a novel variational renormalization group method [85] that enables a solution of the Lindblad master equation (1.7) directly for mesoscopic ensembles of up to one hundred spins.

Chapter 2.

Macroscopic spin ensembles

Ensembles of spins coupled to a cavity form a peculiar many-particle system in the sense that interactions among the individual spins are mediated by the common cavity mode leading to extremely long-range interactions and a suppression of fluctuations [47]. Since the quantum fluctuations decrease with $1/N$ [78, 114], semiclassical mean-field descriptions often provide an accurate description for macroscopic spin ensembles constituting a large number of spins. In this chapter, we first discuss the linear regime in which the number of excitations in the system is negligible compared to the number of spins—a situation that occurs in many experimental realizations [33–37, 43]. Then, we move beyond this few-excitation limit entering the nonlinear regime governed by the semiclassical Maxwell-Bloch equations.

2.1. Volterra integral equation[1]

A commonly used approximation in quantum optical setups involving spin ensembles is the assumption that the number of excitations in the system is small compared to the total number of spins within the ensemble. In this case, the infinite hierarchy of equations discussed in the previous section naturally truncates, resulting in a closed set of equations, which can be readily solved. To obtain this few-excitation limit, we note that

$$\sigma_k^z = -\mathbb{1} + 2\underbrace{\sigma_k^+ \sigma_k^-}_{\hat{n}_k^s},\tag{2.1}$$

where $\hat{n}_k^s = \sigma_k^+ \sigma_k^-$ gives the excitation probability for the k-th spin. If the number of spins in the ensemble is large compared to the total number of excitations in the system, we can assume that most spins are in their ground state $\langle \sigma_k^z \rangle \approx -1$, which is also known as Holstein-Primakoff approximation [115]. In particular, we obtain

$$\langle \sigma_k^z a \rangle = -\langle a \rangle + 2 \langle \sigma_k^+ \sigma_k^- a \rangle \approx -\langle a \rangle,\tag{2.2}$$

---

[1] In this section, we closely follow the derivation of the Volterra integral formalism given in ref. [38].

which can be inserted in Eq. (1.10b) to truncate the infinite hierarchy of equations. It is worth noting that the latter approximation (2.2) becomes exact in the single-excitation regime, since the product $\sigma_k^- a$ annihilates two excitations in total such that $\langle \sigma_k^+ \sigma_k^- a \rangle = 0$.

The equations of motion for the spin-cavity system in the few-excitation limit are then given by

$$\frac{d}{dt}\langle a \rangle = -(\kappa + i\,\Delta_c)\langle a \rangle - i \sum_{k=1}^{N} g_k \langle \sigma_k^- \rangle + \eta\,, \tag{2.3a}$$

$$\frac{d}{dt}\langle \sigma_k^- \rangle = -(\gamma_\perp + i\,\Delta_k)\langle \sigma_k^- \rangle - i\,g_k\langle a \rangle\,, \tag{2.3b}$$

with $\gamma_\perp \equiv \gamma_h + 2\gamma_p$. Equations (2.3a) and (2.3b) form a closed set of $2+2N$ (real valued) linear differential equations, which can be solved either directly by numerical integration for specified initial conditions or by setting up a single Volterra equation for the cavity amplitude, as detailed below. Note that, since the equations of motion (2.3a) and (2.3b) are linear, the cavity amplitude $\langle a(t) \rangle$ is always directly proportional to the driving amplitude η. Nonlinear phenomena, as presented in Section 4, are therefore absent in this formalism.

To set up a single Volterra equation for the cavity amplitude, we formally integrate Eq. (2.3b), which gives

$$B_k(t) = B_k(0)e^{-(\gamma_\perp + i\Delta_k)t} - ig_k \int_0^t d\tau\, e^{-(\gamma_\perp + i\Delta_k)(t-\tau)}A(\tau), \tag{2.4}$$

where we have introduced the shorthand notation $A(t) \equiv \langle a(t) \rangle$ and $B_k(t) \equiv \langle \sigma_k(t) \rangle$. Substituting Eq. (2.4) into Eq. (2.3a), we obtain

$$\frac{d}{dt}A(t) = -\,(\kappa + i\Delta_c)A(t) - i \sum_{k=1}^{N} g_k B_k(0)e^{-(\gamma_\perp + i\Delta_k)t} + \eta(t)$$

$$-\sum_{k=1}^{N} g_k^2 \int_0^t d\tau\, e^{-(\gamma_\perp + i\Delta_k)(t-\tau)}A(\tau). \tag{2.5}$$

Since we are considering macroscopic spin ensembles, in the following, we can go to the continuous limit (in frequency) introducing the spectral spin density

$$\rho(\omega) \equiv \sum_{k=1}^{N} g_k^2 \delta(\omega - \omega_k)/\Omega^2, \tag{2.6}$$

with $\Omega^2 \equiv \sum_{j=1}^{N} g_j^2$ being the collective coupling strength of the spin ensemble to the cavity, which ensures the normalization condition $\int d\omega\, \rho(\omega) = 1$. Using Eq. (2.6),

we can rewrite Eq. (2.5) as

$$\frac{d}{dt}A(t) = -(\kappa + i\Delta_c)A(t) - \Omega^2 \int_0^\infty d\omega \rho(\omega) \int_0^t d\tau e^{-i(\omega-\omega_p-i\gamma_\perp)(t-\tau)} A(\tau) + \eta(t), \quad (2.7)$$

where the second term of Eq. (2.5) was omitted assuming that all spins are initially in the ground state, $B_k(0) = 0$. Performing a transformation to a rotating frame with

$$\tilde{A}(t) \equiv A(t)e^{i(\Delta_c - i\kappa)t} \quad (2.8)$$

yields

$$\frac{d}{dt}\tilde{A}(t) = -\Omega^2 \int_0^\infty d\omega \rho(\omega) \int_0^t d\tau e^{-i(\omega-\omega_c-i(\gamma_\perp-\kappa))(t-\tau)} \tilde{A}(\tau) + \eta(t)e^{i(\omega_c-\omega_p-i\kappa)t}. \quad (2.9)$$

Next, we integrate Eq. (2.9), which gives

$$\tilde{A}(t) = \tilde{A}(0) - \Omega^2 \int_0^\infty d\omega \rho(\omega) \int_0^t dt' \int_0^{t'} d\tau e^{-i(\omega-\omega_c-i(\gamma_\perp-\kappa))(t'-\tau)} \tilde{A}(\tau)$$
$$+ \int_0^t dt' \eta(t')e^{i(\omega_c-\omega_p-i\kappa)t'}. \quad (2.10)$$

The double integral in the second term of Eq. (2.10) can be further simplified by

$$\int_0^t dt' \int_0^{t'} d\tau e^{-i(\omega-\omega_c-i\xi)(t'-\tau)} \tilde{A}(\tau) = \int_0^t dt' e^{-i(\omega-\omega_c-i\xi)t'} \int_0^{t'} d\tau e^{i(\omega-\omega_c-i\xi)\tau} \tilde{A}(\tau)$$

$$= \int_0^t dt' \underbrace{\frac{d}{dt'}\left(\frac{e^{-i(\omega-\omega_c-i\xi)t'}}{-i(\omega-\omega_c-i\xi)}\right)}_{v(t')} \underbrace{\int_0^{t'} d\tau e^{i(\omega-\omega_c-i\xi)\tau} \tilde{A}(\tau)}_{u(t')}$$

$$= i\frac{1}{(\omega-\omega_c-i\xi)}\int_0^t d\tau (e^{-i(\omega-\omega_c-i\xi)(t-\tau)} - 1)\tilde{A}(\tau), \quad (2.11)$$

where we introduced the shortened notation $\xi \equiv \gamma_\perp - \kappa$ and, in the last step, used partial integration. Equation (2.10) is then given by

$$\tilde{A}(t) = \tilde{A}(0) - i\,\Omega^2 \int_0^\infty d\omega \frac{\rho(\omega)}{(\omega-\omega_c-i\xi)}\int_0^t d\tau (e^{-i(\omega-\omega_c-i\xi)(t-\tau)} - 1)\tilde{A}(\tau)$$
$$+ \int_0^t d\tau\, \eta(\tau)e^{i(\omega_c-\omega_p-i\kappa)\tau}. \quad (2.12)$$

After performing the inverse transformation of Eq. (2.8), we finally arrive at the following Volterra equation for the cavity amplitude

$$A(t) = \int_0^t d\tau \mathcal{K}(t-\tau)A(\tau) + \mathcal{F}(t), \quad (2.13)$$

which contains the kernel function $\mathcal{K}(t - \tau)$,

$$\mathcal{K}(t - \tau) = \Omega^2 \int_0^\infty d\omega \, \frac{\rho(\omega) \left[e^{-i(\omega - \omega_c - i\xi)(t-\tau)} - 1 \right]}{i(\omega - \omega_c - i\xi)} \, e^{-i(\omega_c - \omega_p - i\kappa)(t-\tau)}, \qquad (2.14)$$

and the function $\mathcal{F}(t)$,

$$\mathcal{F}(t) = A(0) + \int_0^t d\tau \, \eta(\tau) e^{-i(\omega_c - \omega_p - i\kappa)(t-\tau)}, \qquad (2.15)$$

where $A(0)$ represents the initial cavity field and $\eta(t)$ an arbitrarily shaped input pulse. The Volterra equation (2.13) can be solved either by direct numerical integration or by the Laplace transformation technique (see refs. [38, 84] or Appendix F for details).

Remarkably, the Volterra integral formalism presented above is valid not only in the semiclassical but also in the quantum regime provided that the cavity is in a single-photon state [55]. In particular, the number of photons inside the cavity is given by $N(t) = \langle 1, \downarrow | a^\dagger(t) a(t) | 1, \downarrow \rangle$, where we assume that the initial state $|1, \downarrow\rangle$ contains a single photon in the cavity and all spins are unexcited. Using the completeness relation for the (at most) single-excitation space

$$\mathbb{1} = |0, \downarrow\rangle \langle 0, \downarrow| + |1, \downarrow\rangle \langle 1, \downarrow| + \sum_k |0, \uparrow_k\rangle \langle 0, \uparrow_k|, \qquad (2.16)$$

where $|0, \uparrow_k\rangle$ denotes a state with no photons in the cavity and a single excitation in the k-th spin (with all other spins unexcited), we obtain

$$\langle 1, \downarrow | a^\dagger(t) \mathbb{1} a(t) | 1, \downarrow \rangle = |\langle 0, \downarrow | a(t) | 1, \downarrow \rangle|^2 + |\langle 1, \downarrow | a(t) | 1, \downarrow \rangle|^2 + \sum_k |\langle 0, \uparrow_k | a(t) | 1, \downarrow \rangle|^2.$$
$$(2.17)$$

For each term in the expression above one can set up a Volterra equation formally equivalent to Eq. (2.13). Since the only initial condition, which does not vanish is given by $A(0) = \langle 0, \downarrow | a(0) | 1, \downarrow \rangle = 1$, the cavity photon number reduces to

$$N(t) = |\langle 0, \downarrow | a(t) | 1, \downarrow \rangle|^2 = |A(t)|^2, \qquad (2.18)$$

where $A(t)$ is exactly given as the solution of the Volterra equation (2.13) with the initial conditions $A(0) = 1$, $B_k(0) = 0$, and $\eta(t) = 0$.

2.2. Maxwell-Bloch equations

Two-level systems such as ensembles of spins are inherently nonlinear so that beyond a particular driving strength, the number of excitations in the ensemble can no

longer be neglected. As a significant number of spins get excited, the Holstein-Primakoff approximation ($\langle\sigma_k^z\rangle \approx -1$) used in the previous section no longer holds, and the infinite hierarchy of equations originating from Eqs. (1.10a)-(1.10c) has to be truncated by different means.

A prominent example of such a truncation scheme is the self-consistent field approximation [116], which relies on factorizing the expectation values containing field and spin operators, e.g.,

$$\langle\sigma_k^z a\rangle \approx \langle\sigma_k^z\rangle\langle a\rangle. \tag{2.19}$$

This factorization of expectation values is well justified in the limit of large spin ensembles where correlations between the cavity field and individual spins become negligible [78, 114]. The validity of this semiclassical approximation is discussed in more detail in Section 4.3.

Applying the above factorization, the equations of motion for the expectation values $\langle a\rangle$, $\langle\sigma_k^-\rangle$, and $\langle\sigma_k^z\rangle$ result in a closed set of nonlinear equations given by

$$\frac{d}{dt}\langle a\rangle = -(\kappa + i\,\Delta_c)\langle a\rangle - i\sum_{k=1}^{N} g_k\langle\sigma_k^-\rangle + \eta\,, \tag{2.20a}$$

$$\frac{d}{dt}\langle\sigma_k^-\rangle = -(\gamma_\perp + i\,\Delta_k)\langle\sigma_k^-\rangle + i\,g_k\,\langle\sigma_k^z\rangle\,\langle a\rangle\,, \tag{2.20b}$$

$$\frac{d}{dt}\langle\sigma_k^z\rangle = -\gamma_\parallel(\langle\sigma_k^z\rangle + 1) + 2i\,g_k(\langle\sigma_k^-\rangle\,\langle a^\dagger\rangle - \langle\sigma_k^+\rangle\,\langle a\rangle), \tag{2.20c}$$

where for convenience we introduced the decay rates $\gamma_\parallel \equiv 2\gamma_h = 1/T_1$ and $\gamma_\perp \equiv \gamma_h + 2\gamma_p = 1/T_2$, with T_1 and T_2 being known as the longitudinal and transverse relaxation time, respectively. Equations (2.20a)-(2.20c) are equivalent to the seminal Maxwell-Bloch equations, which play an integral part in semiclassical quantum optics describing phenomena like lasing [117], superradiance [47, 118, 119], optical bistability [120–123], or critical slowing down [39, 82, 124].

Importantly, the Maxwell-Bloch equations are nonlinear, which allows us to describe the dynamics and stationary states for large spin ensembles beyond the few-excitation limit. Furthermore, note that for a fixed spin distribution $\rho(\omega)$, the Maxwell-Bloch equations are invariant to changes in the number of spins N under the following transformation

$$g_k \to g_k/\sqrt{N}, \quad \langle a\rangle \to \langle a\rangle\,\sqrt{N}, \quad \eta \to \eta\,\sqrt{N}, \tag{2.21}$$

which can be used to reduce the number of spins in the numerical calculations.

In general, the Maxwell-Bloch equations form a closed set of $2+3N$ (real valued) equations, which can be solved for given initial conditions, e.g., using a standard Runge-Kutta method [125]. For the case of a homogeneous spin ensemble, i.e., when

all spins have the same transition frequency and coupling strength, the effective number of equations to be solved reduces to a total of five (three, if $\Delta_c = \Delta_k = 0$). However, for an inhomogeneous spin ensemble, the distribution of spin frequencies Δ_k and coupling strengths g_k must be taken into account explicitly (see Appendix C). As shown through several examples in this thesis, the accurate modeling of inhomogeneous broadening is essential for the description of many quantum optical phenomena.

Chapter 3.

Mesoscopic spin ensembles

As described in the previous chapter, semiclassical methods often give an accurate description in the limit of large spin ensembles. However, when the number of spins in the ensemble decreases, quantum fluctuations start to play a prominent role and have to be included in the theoretical model. We then speak of mesoscopic spin ensembles—here the number of spins is too large for a direct integration of the master equation and not yet large enough to permit a semiclassical description.

While being theoretically challenging, the mesoscopic regime offers the unique possibility to synergistically combine the collective behavior of spin ensembles with the nonclassical features of individual spins. First results in this direction include the observation of the unconventional photon blockade [126, 127], superbunching [128], and collective dark states [129].

In this chapter, we discuss two complementary approaches to describe the dynamics of mesoscopic spin ensembles inside a cavity. First, we review the cumulant or cluster expansion method [83, 130], which allows us to calculate corrections to the semiclassical Maxwell-Bloch equations. Then we introduce a variational renormalization group method [85] to obtain the full quantum dynamics for spin-cavity systems consisting of up to one hundred spins.

3.1. Cumulant expansion method[2]

The factorization of the expectation values [Eq. (2.19)], which lead to the Maxwell-Bloch equations in the previous chapter, eliminates any correlations between the cavity field and the individual spins in the ensemble. To preserve these correlations, the corresponding hierarchic equations of motion must be truncated at some higher order, which can be done systematically using the generalized cumulant expansion method [83, 109–112, 130, 131].

---

[2] The cumulant expansion method for the inhomogeneous Tavis-Cummings system was developed during my diploma thesis [130] and is presented here only for completeness since this method forms the basis for the publication [83], which is the topic of Section 4.3.

The cumulant for the product of l operators $\hat{X}_1 \hat{X}_2 \ldots \hat{X}_l$ is defined as [131]

$$
\langle \mathcal{O}(\hat{X}_1 \hat{X}_2 \ldots \hat{X}_l) \rangle_c \equiv \frac{\partial}{\partial \lambda_1} \frac{\partial}{\partial \lambda_2} \cdots \frac{\partial}{\partial \lambda_l} \ln \left\langle \mathcal{O}(e^{\lambda_1 \hat{X}_1 + \lambda_2 \hat{X}_2 + \ldots + \lambda_l \hat{X}_l}) \right\rangle \bigg|_{\lambda_1 = \ldots = \lambda_l = 0} ,
$$

$$(3.1)$$

where $\mathcal{O}$ specifies the ordering of the operators. In the following, we denote an expectation value involving l operators as an l-th order expectation value; similarly, we denote a cumulant of l operators as an l-th order cumulant. Using the definition (3.1), the expressions for cumulants up to fourth order are given by

$$
\langle \hat{A} \rangle_c = \langle \hat{A} \rangle , \tag{3.2a}
$$

$$
\langle \hat{A}\hat{B} \rangle_c = \langle \hat{A}\hat{B} \rangle - \langle \hat{A} \rangle \langle \hat{B} \rangle , \tag{3.2b}
$$

$$
\langle \hat{A}\hat{B}\hat{C} \rangle_c = \langle \hat{A}\hat{B}\hat{C} \rangle - \langle \hat{A}\hat{B} \rangle \langle \hat{C} \rangle - \langle \hat{A}\hat{C} \rangle \langle \hat{B} \rangle - \langle \hat{B}\hat{C} \rangle \langle \hat{A} \rangle + 2 \langle \hat{A} \rangle \langle \hat{B} \rangle \langle \hat{C} \rangle , \tag{3.2c}
$$

$$
\begin{aligned}
\langle \hat{A}\hat{B}\hat{C}\hat{D} \rangle_c = \langle \hat{A}\hat{B}\hat{C}\hat{D} \rangle &- \Big(\langle \hat{A} \rangle \langle \hat{B}\hat{C}\hat{D} \rangle + \langle \hat{B} \rangle \langle \hat{A}\hat{C}\hat{D} \rangle + \langle \hat{C} \rangle \langle \hat{A}\hat{B}\hat{D} \rangle \\
&+ \langle \hat{D} \rangle \langle \hat{A}\hat{B}\hat{C} \rangle + \langle \hat{A}\hat{B} \rangle \langle \hat{C}\hat{D} \rangle + \langle \hat{A}\hat{C} \rangle \langle \hat{B}\hat{D} \rangle + \langle \hat{A}\hat{D} \rangle \langle \hat{B}\hat{C} \rangle \Big) \\
&+ 2 \Big(\langle \hat{A}\hat{B} \rangle \langle \hat{C} \rangle \langle \hat{D} \rangle + \langle \hat{A}\hat{C} \rangle \langle \hat{B} \rangle \langle \hat{D} \rangle + \langle \hat{A}\hat{D} \rangle \langle \hat{B} \rangle \langle \hat{C} \rangle \\
&\quad + \langle \hat{B}\hat{C} \rangle \langle \hat{A} \rangle \langle \hat{D} \rangle + \langle \hat{B}\hat{D} \rangle \langle \hat{A} \rangle \langle \hat{C} \rangle + \langle \hat{C}\hat{D} \rangle \langle \hat{A} \rangle \langle \hat{B} \rangle \Big) \\
&- 6 \langle \hat{A} \rangle \langle \hat{B} \rangle \langle \hat{C} \rangle \langle \hat{D} \rangle .
\end{aligned} \tag{3.2d}
$$

Note that the first-order cumulant [Eq. (3.2a)] is given by the expectation value of the operator itself and the second-order cumulant [Eq. (3.2b)] corresponds to the co-variance of two operators. While the expressions for higher-order cumulants become more complicated, Eq. (3.1) ensures that a cumulant can always be represented by a combination of expectation values of equal or lower order.

In the cumulant expansion method, we exploit this latter property to system-atically truncate the infinite hierarchy of equations encountered in Section 1.2 by neglecting cumulants above a certain order. Specifically, by setting all cumulants of n-th order to zero, the expectation values of n-th order are fully determined by lower-order expectation values. This allows us to truncate the hierarchy presented in Appendix B to obtain a closed set of equations, which can be solved, e.g., by standard Runge-Kutta integration [125]. In the following, we label the cumulant expansion by the highest order of cumulants included in the equations of motion. With this nomenclature, the semiclassical Maxwell-Bloch equations (2.20a)-(2.20c), which contain only first-order moments, correspond to a first-order cumulant ex-pansion (CE1).

The second-order cumulant expansion (CE2) consists of the equations of motion for expectation values up to the second-order (see Appendix B): $\langle a \rangle$, $\langle \sigma_k^- \rangle$, $\langle \sigma_k^z \rangle$,

$\langle \sigma_k^z a \rangle$, $\langle \sigma_k^z \sigma_j^- \rangle$, $\langle \sigma_k^- a^\dagger \rangle$, $\langle \sigma_k^+ \sigma_j^- \rangle$, $\langle \sigma_k^- a \rangle$, $\langle a^\dagger a^\dagger \rangle$, $\langle a^\dagger a \rangle$, $\langle \sigma_k^z \sigma_j^z \rangle$, $\langle \sigma_k^- \sigma_j^- \rangle$. The equations (B.1)-(B.12) form a closed set, if all third-order expectation values therein are expressed by lower-order expectation values through Eq. (3.2c) (assuming $\langle \hat{A}\hat{B}\hat{C} \rangle_c = 0$),

$$\langle \hat{A}\hat{B}\hat{C} \rangle = \langle \hat{A}\hat{B} \rangle \langle \hat{C} \rangle + \langle \hat{A}\hat{C} \rangle \langle \hat{B} \rangle + \langle \hat{B}\hat{C} \rangle \langle \hat{A} \rangle - 2 \langle \hat{A} \rangle \langle \hat{B} \rangle \langle \hat{C} \rangle . \qquad (3.3)$$

Similarly, for the third-order cumulant expansion (CE3), we extend the set of equations by equations of motion for third-order expectation values (see Appendix B), $\langle \sigma_k^z a^\dagger a \rangle$, $\langle \sigma_k^- a^\dagger a \rangle$, $\langle \sigma_k^- a^\dagger a^\dagger \rangle$, $\langle \sigma_k^z aa \rangle$, $\langle \sigma_k^- aa \rangle$, $\langle a^\dagger aa \rangle$, $\langle aaa \rangle$, $\langle \sigma_k^z \sigma_j^z a \rangle$, $\langle \sigma_k^- \sigma_j^- a^\dagger \rangle$, $\langle \sigma_k^+ \sigma_j^- a \rangle$, $\langle \sigma_k^z \sigma_j^- a^\dagger \rangle$, $\langle \sigma_k^z \sigma_j^- a \rangle$, $\langle \sigma_k^- \sigma_j^- a \rangle$ and replace fourth-order expectation values by

$$\begin{aligned}
\langle \hat{A}\hat{B}\hat{C}\hat{D} \rangle = &\Big(\langle \hat{A} \rangle \langle \hat{B}\hat{C}\hat{D} \rangle + \langle \hat{B} \rangle \langle \hat{A}\hat{C}\hat{D} \rangle + \langle \hat{C} \rangle \langle \hat{A}\hat{B}\hat{D} \rangle \\
&+ \langle \hat{D} \rangle \langle \hat{A}\hat{B}\hat{C} \rangle + \langle \hat{A}\hat{B} \rangle \langle \hat{C}\hat{D} \rangle + \langle \hat{A}\hat{C} \rangle \langle \hat{B}\hat{D} \rangle + \langle \hat{A}\hat{D} \rangle \langle \hat{B}\hat{C} \rangle \Big) \\
&- 2\Big(\langle \hat{A}\hat{B} \rangle \langle \hat{C} \rangle \langle \hat{D} \rangle + \langle \hat{A}\hat{C} \rangle \langle \hat{B} \rangle \langle \hat{D} \rangle + \langle \hat{A}\hat{D} \rangle \langle \hat{B} \rangle \langle \hat{C} \rangle \\
&\quad + \langle \hat{B}\hat{C} \rangle \langle \hat{A} \rangle \langle \hat{D} \rangle + \langle \hat{B}\hat{D} \rangle \langle \hat{A} \rangle \langle \hat{C} \rangle + \langle \hat{C}\hat{D} \rangle \langle \hat{A} \rangle \langle \hat{B} \rangle \Big) \\
&+ 6 \langle \hat{A} \rangle \langle \hat{B} \rangle \langle \hat{C} \rangle \langle \hat{D} \rangle ,
\end{aligned} \qquad (3.4)$$

where we used Eq. (3.2d) and $\langle \hat{A}\hat{B}\hat{C}\hat{D} \rangle_c = 0$. Note that third-order expectation values containing only spin operators are not included and are truncated on the level of Eq. (3.3), which is justified since correlations among three spins play only a minor role as compared to correlations between spins and the collective cavity mode.

In principle, also higher orders of the cumulant expansion can be easily implemented with the help of program packages as presented in refs. [132–134]. In this work, however, we restrict ourselves to the second and third order presented above. Note that for inhomogeneous broadening, the number of real-valued equations for these orders of the cumulant expansion is already $4N^2 + N(N-1)/2 + 5N + 5$ and $13N^2 + N(N-1)/2 + 5N + 9$, respectively. For a systematic study of the importance of different terms considered in the cumulant expansion see ref. [112].

3.2. The variational renormalization group[3]

So far we have considered methods based on equations of motion for expectation values. While the cumulant expansion allows us to compute corrections to semi-

---

[3] The major credit for the development of this method goes to Himadri S. Dhar, who worked in our group as a Marie Skłodowska-Curie fellow and is now at the Indian Institute of Technology Bombay (ITT Bombay). A detailed description of the method can be found also in the supplementary material of our joint publication [85], from where also parts of the text are taken.

classical expectation values, it does not provide access to the full quantum state of the spin-cavity system. In this section, we introduce a time-adaptive variational renormalization group method [85] that allows us to calculate the full quantum dynamics of the driven and dissipative spin-cavity system containing as many as one hundred spins.

Over the past few decades variational renormalization group methods based on a tensor-network formalism [135–137] have been very successful in describing the ground state and unitary dynamics of one-dimensional many-body quantum systems. Meanwhile, these methods have been extended to higher-dimensional systems [135, 137] as well as to finite temperature states [138, 139] in quantum spin lattices. In contrast to quantum spin models with short-range spin-spin interactions, which are typically the target of conventional tensor network methods [135–139], the interactions among spins in our spin-cavity system are mediated only via the common cavity mode. This allows us to treat the spin ensemble coupled to the cavity as a central spin problem [140]. In our approach, however, the cavity plays the role of the central quantum system interacting with the spin ensemble that acts like a fermionic bath. Hence, the spin ensemble is renormalized and truncated at each step in a time-adaptive manner, similar to a time-evolving block decimation (TEBD) [141, 142] or a time-dependent density matrix renormalization group (t-DMRG) method [143, 144], while the cavity state is always stored exactly. The novelty of our approach is that the time-adaptive renormalization is done directly in the superoperator space of the Lindblad master equation (1.7), instead of the more widely implemented approach where the renormalization is applied at the level of the unitary time evolution in the much larger system-environment Hilbert space [145–147].

The starting point for our method is the Lindblad master equation (1.7), which acts on the larger space of operators rather than the Hilbert space of the quantum system itself [148]. It is therefore convenient to map the spin-cavity system to a higher-dimensional complex vector space, such that a $d{\times}d$–dimensional density matrix, ρ, is vectorized to a $d^2{\times}1$–dimensional superket, $|\rho\rangle = \mathbf{vec}(\rho)$. Also, a $d \times d$ operator, $\hat{O}$, which acts on ρ, is given by the higher-dimensional, $d^2{\times}d^2$ superoperator, $\hat{\mathcal{O}}$, which now acts on $|\rho\rangle$. In particular, we can make the following replacements: $\rho \to |\rho\rangle$, $\hat{O}\rho \to (\hat{O} \otimes \mathbb{1}_d)\,|\rho\rangle = \hat{\mathcal{O}}\,|\rho\rangle$, and $\rho\hat{O} \to (\mathbb{1}_d \otimes \hat{O}^T)\,|\rho\rangle = \hat{\mathcal{O}}'\,|\rho\rangle$, where $\mathbb{1}_d$ is the d–dimensional identity matrix. The time evolution of the spin-cavity system can then be written by the matrix equation

$$\frac{d}{dt}\,|\rho\rangle = \tilde{\mathcal{L}}\,|\rho\rangle\,, \tag{3.5}$$

where

$$\tilde{\mathcal{L}} = -i(H \otimes \mathbb{1}_d - \mathbb{1}_d \otimes H^T) + 2\kappa\tilde{\mathcal{L}}_{\hat{a}_c} + \sum_{k=1}^{N} 2\gamma_h \tilde{\mathcal{L}}_{\sigma_k^-} + \sum_{k=1}^{N} \gamma_p \tilde{\mathcal{L}}_{\sigma_k^z}, \tag{3.6}$$

with

$$\tilde{\mathcal{L}}_{\hat{x}} = \hat{x} \otimes \hat{x}^* - \frac{1}{2}\hat{x}^\dagger \hat{x} \otimes \mathbb{1}_d - \frac{1}{2}\mathbb{1}_d \otimes \hat{x}^T \hat{x}^*. \tag{3.7}$$

Since the spins interact only with the single cavity mode, we can map the spin-cavity system to a central body problem [140] and rewrite the terms in H and $\tilde{\mathcal{L}}_{\hat{x}}$ as a sum of individual spin-cavity terms

$$\tilde{\mathcal{L}} = \sum_{k=1}^{N} \tilde{\mathcal{L}}_k = \sum_{k=1}^{N} \left[-i(H_k \otimes \mathbb{1}_d - \mathbb{1}_d \otimes H_k^T) + 2\gamma_h \tilde{\mathcal{L}}_{\sigma_k^-} + \gamma_p \tilde{\mathcal{L}}_{\sigma_k^z} + \frac{2\kappa}{N}\tilde{\mathcal{L}}_{\hat{a}_c} \right]. \tag{3.8}$$

The time evolution of the system is then performed using the second-order Suzuki-Trotter decomposition [149]

$$\mathcal{V}(\Delta t) = e^{\sum_k \tilde{\mathcal{L}}_k \Delta t} \approx e^{\tilde{\mathcal{L}}_N \frac{\Delta t}{2}} e^{\tilde{\mathcal{L}}_{N-1} \frac{\Delta t}{2}} \cdots e^{\tilde{\mathcal{L}}_2 \frac{\Delta t}{2}} e^{\tilde{\mathcal{L}}_1 \Delta t} e^{\tilde{\mathcal{L}}_2 \frac{\Delta t}{2}} \cdots e^{\tilde{\mathcal{L}}_{N-1} \frac{\Delta t}{2}} e^{\tilde{\mathcal{L}}_N \frac{\Delta t}{2}}, \tag{3.9}$$

by sequentially applying the time evolution on the k-th spin and the cavity while the remaining spins are kept in the renormalized subspace. A full time step Δt, therefore, consists of a double sweep through the spin ensemble, starting from the N-th spin to the 1-st spin and then back to the N-th spin, similar to a conventional TEBD or t-DMRG method [141–144].

The key step in typical renormalization group methods is the truncation of the reduced density matrix space to make the exponentially large Hilbert space of the many-body system numerically tractable [136]. In our case, this translates to the renormalization of the reduced superoperator space of the open spin-cavity system. We use the Schmidt decomposition [136] dividing the system into two blocks, A and B, such that A contains N_1 spins, and B contains the remaining $N - N_1$ spins and the cavity:

$$|\rho\rangle = \sum_{\tilde{k}=1}^{\mathcal{K}} \alpha_{\tilde{k}} |\tilde{k}_A\rangle |\tilde{k}_B\rangle. \tag{3.10}$$

Here, $\{\alpha_{\tilde{k}}\}$ are the Schmidt coefficients in descending order, and $|\tilde{k}_A\rangle$ and $|\tilde{k}_B\rangle$ are the eigenvectors of the reduced superoperators, $\mathcal{R}_A = \text{Tr}_B(|\rho\rangle\langle\rho|)$ and $\mathcal{R}_B = \text{Tr}_A(|\rho\rangle\langle\rho|)$, respectively. For pure states, the Schmidt rank $\mathcal{K}$ determines the entanglement between the bipartitions A and B. However, since $|\rho\rangle$ is a vectorized density matrix, $\mathcal{K}$ in this case can be interpreted as a measure of total correlations [150]. Theoretically, $\mathcal{K}$ is bounded by $1 \leq \mathcal{K} \leq r$, where $r = \min[\text{rank}(\mathcal{R}_A), \text{rank}(\mathcal{R}_B)]$. While r can grow exponentially with the number of spins in the ensemble, for most physical situations $\mathcal{K}$ is small and the Schmidt coefficients $\alpha_{\tilde{k}}$ decay rapidly with $\tilde{k}$ [139]. This corresponds to the case of a weakly correlated system that, in a sense, does not occupy the entire exponentially growing Hilbert space. Thus, by retaining only the $\mathcal{D}$ highest Schmidt coefficients $\alpha_{\tilde{k}}$, we can effectively describe the system

in a renormalized space of significantly reduced dimension, i.e.,

$$|\rho\rangle \approx \sum_{\tilde{k}=1}^{\mathcal{D}} \alpha_{\tilde{k}} |\tilde{k}_A\rangle |\tilde{k}_B\rangle, \tag{3.11}$$

with $\mathcal{D} \ll r$.

The accuracy of the renormalization depends on the choice of $\mathcal{D}$ and is exact for weakly or uncorrelated systems. Note that, starting from an uncorrelated ensemble, where all spins are in their ground state, correlations among spins typically build up only slowly via their interaction with the common cavity mode. For the calculations in this work, we chose $\mathcal{D} \lesssim 200$, and often even a value much lower than this was already sufficient to get an accurate account for the dynamics of mesoscopic spin ensembles. A more detailed description of the numerical implementation of our method and a benchmark against exact solutions for few spins is provided in the supplemental material of ref. [85].

Part II.

Applications and results

Chapter 4.

Optical bistability and critical phenomena

Nonlinear phenomena are ubiquitous in nature and range from galaxy formation and fluid dynamics to neuronal signaling and the spread of infectious diseases [151–154]. What all nonlinear systems have in common is that their output is not directly proportional to their input. A paradigm example in this regard is *optical bistability* — the phenomenon of two distinct stable stationary states that coexist for the same parameter values. Here, the transmission through a cavity does not solely depend on the system parameters but also on the initial condition from which the system approaches the stationary state giving rise to a hysteresis cycle. Besides this stationary effect, bistability is also associated with an interesting transient effect known as *critical slowing down*, which is characterized by extremely long relaxation times that can exceed the system's intrinsic time scales by orders of magnitude. Both phenomena are hallmark effects in nonlinear optics and have been extensively studied since the early days of quantum optics up until now [39, 82, 83, 102, 120, 121, 155–166]. A good overview can be found, for example, in the classic review article by Lugiato [123] or in the textbook by Lugiato, Prati, and Brambilla [167].

In this chapter, we first theoretically examine optical bistability on the example of amplitude bistability in a driven spin-cavity system. We investigate the onset of this effect for different shapes of the spectral spin distribution [82] and present a specific realization in a solid-state spin ensemble based on negatively charged nitrogen-vacancy centers in diamond strongly coupled to a single-mode microwave cavity [39]. For this setup, a critical slowing down of the cavity photon number on the order of 11 hours was demonstrated—a time scale much longer than ever observed for this effect. We provide a detailed theoretical study of this critical slowing down using the Maxwell-Bloch equations presented in Section 2.2. Thereby, we analyze the transient times of the cavity field amplitude finding a universal power-law divergence.

While a semiclassical description based on the Maxwell-Bloch equations is well justified for large spin ensembles, it may lose this validity as the number of spins in the ensemble becomes smaller. The actual system size at which this happens

depends strongly on the experimental realization and the system parameters at hand. At the end of this chapter, we introduce a universal procedure to determine the validity of the Maxwell-Bloch equations setting up a semiclassical-to-quantum boundary. We show that in the vicinity of the bistable regime even apparently large spin ensembles consisting of up to tens of thousands of spins can defy a semiclassical description [83].

4.1. Optical bistability[4]

Optical bistability arises from the interplay between a nonlinear medium and the feedback provided by cavity mirrors, which enables the co-existence of two stable stationary states of different transmission for the same parameter values. Over the past decades, this phenomenon has been realized in various systems including saturable absorbers [155, 165], atomic ensembles [160–162], superconducting qubits [166], and integrated semiconductor devices [163]. In addition to its relevance for technological applications in all-optical switches or logic gates [169, 170], optical bistability is also a paradigm example of a driven dissipative phase transition far from thermal equilibrium [156–159].

In the following, we consider a macroscopic ensemble of two-level systems strongly coupled to a single cavity mode. To observe bistability, we study the stationary transmission through the cavity under constant driving η. Using the standard input-output theory [171, 172], the transmission is proportional to the cavity probability amplitude $|\langle a \rangle|^2$, whose stationary value $|\langle a_{st} \rangle|^2$ can be calculated from the Maxwell-Bloch equations (2.20a)-(2.20c) by setting all time derivatives to zero. Assuming resonant driving ($\omega_p = \omega_c = \omega_s$) as well as a symmetric spin distribution, the steady-state equation for the cavity amplitude $\langle a_{st} \rangle$ is given by (see Appendix D)

$$\langle a_{st} \rangle \left(1 + \sum_k \frac{C_k}{1 + |\langle a_{st} \rangle|^2/n_k} \right) = \frac{\eta}{\kappa}. \tag{4.1}$$

Here, C_k and n_k are the cooperativity parameter and the photon saturation number of the k-th spin, respectively, defined as

$$C_k \equiv \frac{g_k^2}{\gamma_\perp \kappa (1 + \Delta_k^2/\gamma_\perp^2)} \tag{4.2}$$

---

[4] The results presented in this section are based on two joint publications [39, 82] from which also parts of the text and figures are taken. The theoretical results were obtained by Dmitry O. Krimer and myself, whereas the experiment was conducted by Andreas Angerer, Stefan Putz, Thomas Astner, Ralph Glattauer, and Kirill Streltsov under the supervision of Jörg Schmiedmayer and Johannes Majer from the Vienna Center for Quantum Science and Technology, Atominstitute, TU Wien. The experimental results of ref. [39] are also presented in the PhD theses of Andreas Angerer [168] and Stefan Putz [51].

and

$$n_k \equiv \frac{\gamma_\perp \gamma_\parallel}{4g_k^2}(1 + \Delta_k^2/\gamma_\perp^2). \tag{4.3}$$

The cooperativity C_k [Eq. (4.2)] is a dimensionless parameter and gives the ratio of the coupling strength of the spins to the decay rates of the system. Similarly, the saturation parameter n_k [Eq. (4.3)] provides a measure for the number of photons initiating a nonlinear response from the spins.

Optical bistability of homogeneous spin ensembles

Before we examine the onset of bistability for inhomogeneously broadened spin ensembles, let us revisit the simpler case of a homogeneous ensemble, where $\Delta_k = 0$ and $g_k = g$ for all spins. The steady-state equation (4.1) then simplifies to

$$\langle a_{st} \rangle \left(1 + \frac{C}{1 + |\langle a_{st} \rangle|^2/n_0} \right) = \frac{\eta}{\kappa}, \tag{4.4}$$

where

$$C \equiv \sum_k C_k = \frac{g^2 N}{\gamma_\perp \kappa} \tag{4.5}$$

is the collective cooperativity[5] for a homogeneous spin ensemble of N spins and

$$n_0 \equiv \frac{\gamma_\perp \gamma_\parallel}{4g^2} \tag{4.6}$$

is the homogeneous photon saturation parameter.

Figure 4.1.1(a) presents the solutions of Eq. (4.4) for the stationary cavity probability amplitude $|\langle a_{st} \rangle|^2$ versus the driving amplitude η for three different collective cooperativity values $C = 4$, 8, and 16. In our simulations we change the cooperativity by adjusting the coupling strengths g while leaving all other parameters unchanged ($\kappa/2\pi = 0.8$ MHz, $\gamma_\perp/2\pi = 250$ kHz, $\gamma_\parallel/2\pi = 100$ Hz). For large driving amplitudes, the spin ensemble saturates such that the stationary spin expectation values vanish and the ensemble effectively decouples from the cavity. At the same time, the cavity probability amplitude approaches the transmission of an empty cavity ($\propto \eta^2/\kappa^2$), as the second term on the left-hand side of Eq. (4.4) (also known as reaction field) vanishes due to $|\langle a_{st} \rangle|^2 \gg n_0$. In the literature, this high transmission branch is also known as the independent-atom branch since it does not depend on the cooperativity parameter [78]. For small driving amplitudes, the transmission is suppressed as compared to the empty cavity case due to the reaction field induced cooperatively by the spin ensemble given in the second term on the left-hand side of Eq. (4.4) [121, 123]. As the solutions at low transmission

---

[5] Note that in the literature, one also finds other definitions of collective cooperativity, which differ from the one above by a factor of 1/2 [102, 123].
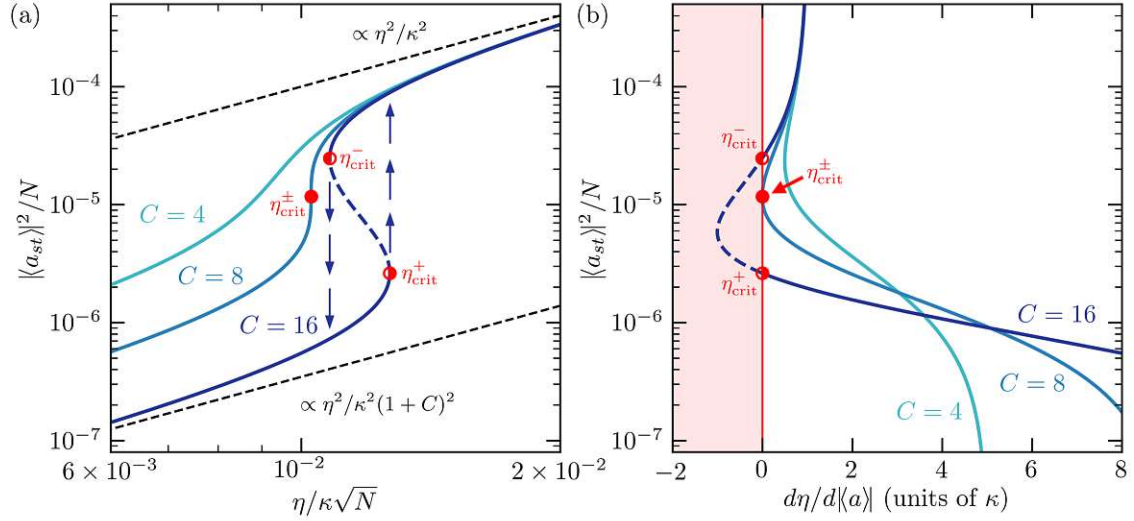
Figure 4.1.1.: Input-output relations for a homogeneous spin ensemble. (a) Stationary probability amplitude $|\langle a_{st}\rangle|^2$ as a function of the driving amplitude η calculated from Eq. (4.4) for $C = 4$, 8, and 16 ($\kappa/2\pi = 0.8$ MHz, $\gamma_\perp/2\pi = 250$ kHz, $\gamma_\parallel/2\pi = 100$ Hz). The stationary solutions display two distinct branches, one of high transmission and one of low transmission. The high transmission branches are almost independent of the cooperativity value C and approach the empty cavity case $\propto \eta^2/\kappa^2$ (upper dashed black line) for large driving amplitudes. The low transmission branches, located in the domain of small driving amplitudes, converge to the value $\eta^2/\kappa^2(1+C)^2$ (lower dashed black line for $C = 16$). Optical bistability occurs for $C > 8$, where two stable solutions (solid lines) and one unstable solution (dashed blue line) coexist within a certain parameter range. The bistable behavior is associated with a first-order phase transition at the critical points $\eta_{\mathrm{crit}}^\pm$ (red half filled circles) characterized by a discontinuous jump from one transmission branch to another (indicated by the blue arrows). (b) Stationary probability amplitude $|\langle a_{st}\rangle|^2$ versus the derivative of the inverse input-output curve $d\eta/d|\langle a_{st}\rangle|$. The critical points $\eta_{\mathrm{crit}}^\pm$ are defined by $d\eta/d|\langle a_{st}\rangle| = 0$ (vertical red line), which corresponds to an infinite slope in the input-output relation presented in (a). For $C > 8$, the derivative $d\eta/d|\langle a_{st}\rangle|$ becomes negative within the bistable interval corresponding to an unstable stationary state (dashed blue line).

strongly depend on the cooperativity parameter C, this low transmission branch is sometimes called the cooperative branch [78]. In the weak driving limit, where the cavity probability amplitude is much smaller than the photon saturation number $|\langle a_{st}\rangle|^2 \ll n_0$, the suppressed transmission follows the linear relation

$$\langle a_{st}\rangle (1 + C) = \eta/\kappa. \tag{4.7}$$

However, if the cavity probability amplitude approaches the photon saturation number, the system's response to the external driving field becomes strongly non-linear and even bistable for sufficiently large cooperativities. The threshold cooper-

ativity of bistability for homogeneous spin ensembles driven on resonance is $C = 8$ [121]. Above this value, there is always a finite interval of η where three solutions (two stable and one unstable) exist simultaneously, as can be seen in Fig. 4.1.1(a) for $C = 16$. Starting at weak driving, here, the steady-state solutions for increasing η follow the low transmission branch up to some critical driving strength η_{crit}^+ at which the system undergoes a first-order phase transition jumping to the high transmission branch [158]. Along the other direction, the steady states follow the high transmission branch before they jump back to the low transmission branch at η_{crit}^-, resulting in a hysteresis cycle.

The bistable region is located between the two critical points $\eta = \eta_{\mathrm{crit}}^-$ and $\eta = \eta_{\mathrm{crit}}^+$, which are determined from the condition that the derivative of the inverse input-output relation $d\eta/d|\langle a_{st}\rangle|$ vanishes (i.e., $d|\langle a_{st}\rangle|/d\eta$ is infinite — a signature of a first-order transition),

$$d\eta/d|\langle a_{st}\rangle| = \kappa \left(1 + C \frac{1 - |\langle a_{st}\rangle|^2/n_0}{(1 + |\langle a_{st}\rangle|^2/n_0)^2} \right) = 0. \tag{4.8}$$

Note, that Eq. (4.8) has a solution only when the cooperativity parameter C is above the threshold value $C_{th} = 8$. The solution is given by the simple analytic form

$$|\langle a_{st}\rangle|_{\mathrm{crit}}^2 = \frac{C - 2}{2} \pm \frac{1}{2}\sqrt{C^2 - 8C}, \tag{4.9}$$

from which the critical driving amplitudes $\eta_{\mathrm{crit}}^\pm$ can be found by substituting $|\langle a_{st}\rangle|_{\mathrm{crit}}^2$ back into the steady-state equation (4.4). We present the cavity probability amplitude $|\langle a_{st}\rangle|^2$ versus the derivative $d\eta/d|\langle a_{st}\rangle|$ in Fig. 4.1.1(b). In the limit of large photon numbers ($|\langle a_{st}\rangle|^2 \gg n_0$), the derivative $d\eta/d|\langle a_{st}\rangle|$ tends towards the cavity decay rate κ for any C. In the opposite limit ($|\langle a_{st}\rangle|^2 \ll n_0$), the derivative is given by $d\eta/d|\langle a_{st}\rangle| = \kappa(1 + C)$. Notably, $d\eta/d|\langle a_{st}\rangle|$ is always positive for cooperativities $C < 8$. Only above this threshold value Eq. (4.8) can be fulfilled, which gives rise to the critical points $\eta_{\mathrm{crit}}^\pm$ and a bistable region. The negative derivative $d\eta/d|\langle a_{st}\rangle| < 0$ within the bistable interval for $C = 16$ can be associated with the unstable steady-state solution depicted in Fig. 4.1.1(a).

Optical bistability and inhomogeneous broadening

The assumption of a homogeneous spin ensemble leads to comparatively simple analytic solutions and a first understanding of the phenomenon of bistability. However, to provide a realistic description for an actual experimental realization, we must include inhomogeneous broadening in the form of a spectral spin density $\rho(\omega)$, which allows for a distribution of spin frequencies $\Delta_k \neq 0$ and coupling strengths g_k (Appendix C). Naturally, the bistability curves given by the steady-state equation (4.1) depend not only on the width of the inhomogeneous broadening but also on

its exact shape [122, 173, 174]. In the following, we explore the onset of bistability for different shapes of the spectral spin distribution $\rho(\omega)$. The critical points delimiting the bistable regime can be obtained from the condition

$$d\eta/d|\langle a_{st}\rangle| = \kappa \left(1 + \sum_k \frac{C_k}{1 + |\langle a_{st}\rangle|^2/n_k} \left(1 - \frac{2|\langle a_{st}\rangle|^2/n_k}{1 + |\langle a_{st}\rangle|^2/n_k}\right)\right) = 0, \qquad (4.10)$$

which we solve numerically for a Lorentzian, a Gaussian, and a q-Gaussian spin density. The latter is a generalized Gaussian given by Eq. (4.12), which depends on the shape parameter q, restoring a Gaussian in the limit $q \to 1$ and a Lorentzian for $q = 2$. Here we take $q = 1.39$ to model an ensemble of nitrogen-vacancy centers in diamond [36]—the physical platform for which we present a realization of optical bistability at the end of this section.
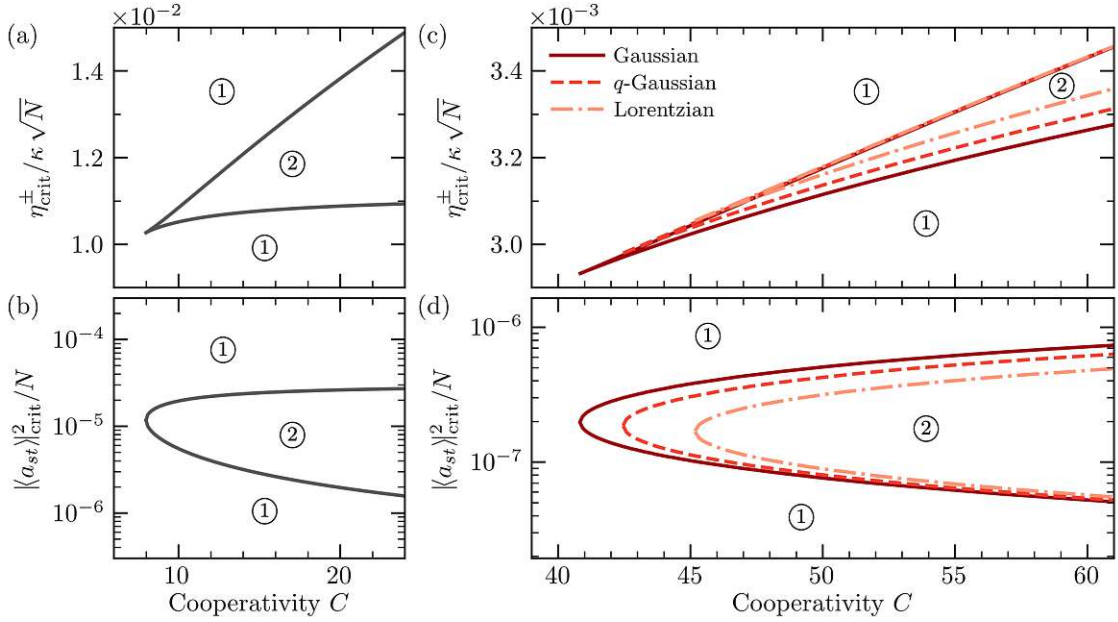
Figure 4.1.2.: Comparison of the onset of bistability for homogeneous (left panels) and inhomogeneous spin ensembles (right panels). Pairs of the critical values of the driving amplitude $\eta_{\mathrm{crit}}^{\pm}$ and the corresponding cavity probability amplitude $|\langle a_{st}\rangle|^2_{\mathrm{crit}}$ (defined by the condition $d\eta/d|\langle a_{st}\rangle| = 0$) as a function of the collective cooperativity C for homogeneous spin ensembles (a,b) and for inhomogeneous spin ensembles (c,d). For the latter, we show results for Gaussian, q-Gaussian ($q = 1.39$), and Lorentzian spin distributions of the same widths $\gamma_{inh}/2\pi = 9.4$ MHz (FWHM). All other parameters are the same as in Fig. 4.1.1 ($\kappa/2\pi = 0.8$ MHz, $\gamma_\perp/2\pi = 250$ kHz, $\gamma_\parallel/2\pi = 100$ Hz). The bistable region ② lies within the critical values, while outside this area there is only a single stationary state ①.

The results of the numerical calculations are displayed in Fig. 4.1.2 along with the analytic results of a homogeneous spin ensemble [Eq. (4.9)]. In particular, we

compare the critical values of the driving amplitude $\eta_{\text{crit}}^{\pm}$ and the corresponding cavity probability amplitude $|\langle a_{st} \rangle|_{\text{crit}}^2$ as a function of the collective cooperativity parameter

$$C \equiv \sum_k C_k = \sum_k \frac{g_k^2}{\gamma_\perp \kappa (1 + \Delta_k^2/\gamma_\perp^2)}. \tag{4.11}$$

Note that we increase C by increasing the individual coupling strengths g_k, while we leave all other parameters constant. Figure 4.1.2 demonstrates that the bistable area bounded by the critical values reduces dramatically due to the inhomogeneous broadening. Furthermore, the bistability threshold, being $C_{th} = 8$ for the homogeneous spin ensemble, becomes 40.8 for the Gaussian, 42.2 for the q-Gaussian (with $q = 1.39$), and 45.2 for the Lorentzian spin distribution, respectively. This shift of the bistability onset towards higher threshold values results from the tails of the spin distribution, which are broader for the Lorentzian than for the q-Gaussian and the Gaussian distribution. Spectrally more distant spins are effectively less and less coupled to the cavity and, therefore, larger cooperativity values are required to observe bistability.

Experimental realization of optical bistability with nitrogen-vacancy centers in diamond

Finally, in collaboration with an experiment performed in the group of Jörg Schmiedmayer [39], we present a realization of optical bistability in a cavity QED system composed of a superconducting microwave resonator coupled to a long-lived electronic spin ensemble formed by negatively charged nitrogen-vacancy (NV) centers in diamond.

NV centers are point defects in diamond with a C_{3v} symmetry consisting of a substitutional nitrogen atom with an adjacent lattice vacancy [175, 176]. Due to their excellent properties such as stability, long coherence times, or the possibility for optical preparation and read-out, NV centers are exciting for numerous tasks in quantum information processing [177–182] and nanoscale sensing [183–191]. The property that is most relevant for us, in the following, is its paramagnetic ground state with electron spin angular momentum $S = 1$, where the states $m_s = \pm 1$ and $m_s = 0$ are separated by ~ 2.88 GHz in zero magnetic field [see Fig. 4.1.3(a)]. Applying a homogeneous magnetic field allows to selectively Zeeman tune the $m_s = 0 \rightarrow m_s = \pm 1$ transition into resonance with a microwave cavity. The combined spin-cavity system is then well described by the Tavis-Cummings Hamiltonian (1.1) [36].

Figure 4.1.3(b) shows the experimental setup, which consists of a neutron-irradiated diamond sample containing a large ensemble of $\sim 10^{12}$ NV centers placed on top of a superconducting $\lambda/2$ transmission line resonator. The experiment is performed in a ^{3}He/^{4}He dilution refrigerator at temperatures below 25 mK to ther-
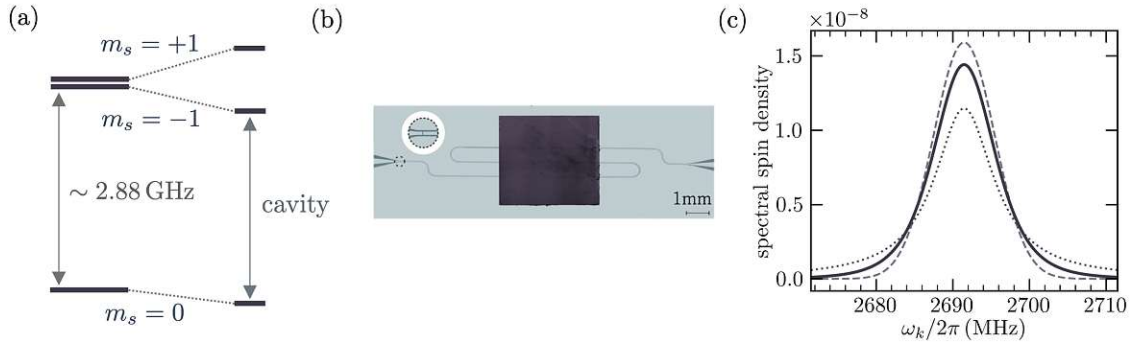
Figure 4.1.3.: (a) Energy level scheme of the NV center's optical ground state ($S = 1$) with a zero-field splitting of ~ 2.88 GHz [176]. Using the Zeeman shift of the $m_s = \pm 1$ states under a magnetic field, the NV center forms a tunable two-level system that can be made resonant with a microwave cavity. (b) Photograph (taken from ref. [39]) of the experimental setup consisting of a superconducting transmission line cavity with an enhanced neutron-irradiated diamond on top of it (black), containing a large ensemble of NV centers ($N \approx 10^{12}$). (c) The ensemble of NV centers is inhomogeneously broadened with a q-Gaussian spectral spin distribution ($q = 1.39$) of width $\gamma_{inh}/2\pi = 9.4$ MHz (FWHM) centered at the cavity frequency $\omega_c/2\pi = 2.691$ GHz. For comparison we show a Gaussian (dashed line) and a Lorentzian distribution (dotted line) of the same width.

mally polarize the spins in their ground state (99% fidelity). For details on the experimental setup see references [39, 51, 168]. The transition frequencies of the individual spins of the NV ensemble deviate slightly from each other due to their different local environments. The main reasons for this inhomogeneous broadening are excess nitrogen P1 impurities, uncharged NV centers, and lattice stress in the host material [192, 193]. We model the inhomogeneous broadening of the spin ensemble by a q-Gaussian spectral spin density [194, 195],

$$\rho(\omega) = D \left[1 - (1 - q)(\omega - \omega_s)^2 / \Delta^2 \right]^{1/(1-q)}, \tag{4.12}$$

depicted in Fig. 4.1.3(c), where q is a dimensionless shape parameter, $\gamma_{inh} = 2\Delta\sqrt{(2^q - 2)/(2q - 2)}$ is the full-width-at-half-maximum (FWHM), and D is a normalization constant. For the ensemble of NV centers, the shape parameter of the spectral spin density is given by $q = 1.39$ [36]. The spin's transverse relaxation rate is estimated as $\gamma_\perp/2\pi = 33$ kHz and the longitudinal relaxation rate as $\gamma_\parallel/2\pi = 3.6$ mHz [39, 192].

Previous experiments studied this system in the weak driving regime, where the number of spin excitations is negligible compared to the total number of spins [34–38, 196]. Here, we go beyond this linear regime and examine the transmission through the cavity under strong driving, which depends nonlinearly on the driving amplitude and can show bistable behavior for large enough cooperativities. The cooperativity in the experiment is changed either by modifying the cavity decay rate

or by changing the number of spins in the cavity. The latter is achieved by bringing a different number of subensembles into resonance with the resonator. Note that, due to the crystallographic diamond structure, four different NV subensembles exist (pointing in the [1, 1, 1] direction). By applying a magnetic field ($B \approx 30$ mT) with either 0° or 45° relative to the [1, 0, 0] direction in the NV resonator plane, four or two NV subensembles can be tuned into resonance with the cavity mode.
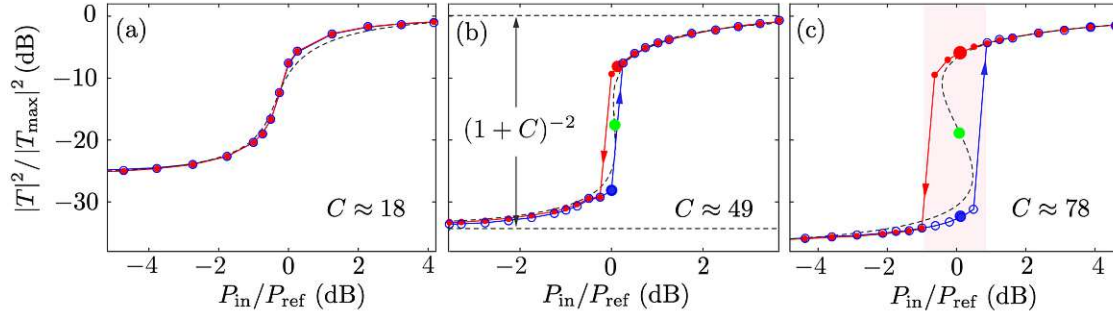
Figure 4.1.4.: Measurement of the normalized stationary transmission through the cavity as a function of increasing (blue) and decreasing (red) input power P_{in}. From (a) to (c) the collective cooperativity value C in the experiment is increased either by increasing the number of spins in resonance with the cavity or by decreasing the cavity decay rate κ, respectively. In (a), $C = 18$ and $\kappa/2\pi = 1.2$ MHz with only two subensembles being in resonance with the cavity. For (b), $C = 49$ as the cavity decay rate is decreased to $\kappa/2\pi = 0.44$ MHz. A small bistability area is visible where the system evolves to a different steady-state either on the high (red) or low transmission branch (blue) depending on the history of the system. The third, unstable steady-state is never reached (green). (c) The collective cooperativity is further increased to $C = 78$ by using four subensembles in resonance with the cavity and $\kappa/2\pi = 0.44$ MHz. For all three cases, the steady-state behavior is well reproduced by a full numerical calculation taking inhomogeneous broadening into account (dashed black lines). Figure adapted from ref. [39].

Figure 4.1.4 presents the transmitted intensities through the cavity under resonant driving for three cooperativity values $C = 18$, 49, and 78. The transmission is defined by $|T|^2 = P_{\mathrm{out}}/P_{\mathrm{in}}$ as a function of the input drive intensity $P_{\mathrm{in}} \approx \eta^2/\kappa$ and outgoing intensity $P_{\mathrm{out}} \approx |\langle a \rangle|^2 \kappa$. The drive power is raised in a stepwise manner, which is slow enough to allow the system to reach a steady state for each input intensity P_{in}. For small input intensities, the cavity field is not sufficient to saturate the spin ensemble ($\langle \sigma_k^z \rangle = -1$) and the transmission is given by $|T|^2 \approx 1/(1+C)^2$. As the input power increases, the spins start to saturate, and the transmission increases nonlinearly following Eq. (4.1). At a collective cooperativity of $C = 18$ there is no bistability and the transmission is a continuous function of the input intensity P_{in} [Fig. 4.1.4(a)]. Increasing the cooperativity to $C = 49$, which is above the threshold value of bistability ($C_{th} = 42.2$), allows us to observe the onset of

bistable behavior [Fig. 4.1.4(b)]. For increasing driving intensities, the system's response undergoes a first-order phase transition at $P_{\text{in}} = P_{\text{crit}}^{+}$ jumping from low to high transmission. If the driving intensities are reduced again, the system jumps back to low transmission values at $P_{\text{in}} = P_{\text{crit}}^{-} < P_{\text{crit}}^{+}$, which gives rise to a hysteresis cycle. At a cooperativity of $C = 78$, we observe optical bistability within a 2-dB range of the driving intensity [Fig. 4.1.4(c)]. Note that, within the bistable range, the transmission on the low and high transmission branches differs by three orders of magnitude for the same parameter value. Here, the system's response solely depends on its history, i.e., the direction from which this parameter point was approached.

4.2. Critical slowing down[6]

So far, we have only dealt with the steady-states of the driven spin-cavity system. In the following, we examine the transient dynamics towards these stationary states. The time scale needed to reach a steady-state is typically given by the inverse loss rates of the system. However, close to the critical points $\eta_{\text{crit}}^{\pm}$ of bistability, these transient times become much longer than all intrinsic time scales [121]. In what follows, we focus on the dynamics of spin ensembles for which nonradiative processes constitute the dominant dephasing mechanism, i.e., $\gamma_h \ll \gamma_p$, and therefore $\gamma_{\parallel} \ll \gamma_{\perp}$. Furthermore, we assume that the cavity decay rate κ is orders of magnitude larger than the longitudinal relaxation rate so that $\gamma_{\parallel} \ll \kappa$. Both inequalities are very well satisfied for impurity spins in solids, such as nitrogen vacancy (NV) centers in diamond.

To obtain the temporal evolution of the system, we solve the Maxwell-Bloch Eqs. (2.20a)-(2.20c) in time. If not specified otherwise, our numerical calculations are performed with a set of parameters typical for the experiments with NV centers presented in the previous section. In particular, we consider a q-Gaussian ($q = 1.39$) spin distribution of width $\gamma_{inh}/2\pi = 9.4$ MHz (FWHM). The collective cooperativity value is set to $C = 78$, with $\kappa/2\pi = 0.8$ MHz and $\gamma_{\perp}/2\pi = 250$ kHz. The longitudinal relaxation rate $\gamma_{\parallel}/2\pi = 100$ Hz is chosen to be orders of magnitude smaller than that measured in real experiments with NV centers. This is done to artificially reduce the integration time in our numerical calculations and, thus, to considerably diminish computational efforts. This, however, causes no qualitative changes for our results. Figure 4.2.1(a) and (b) show typical results for

---

[6] The results presented in this section are based on two joint publications [39, 82] from which also parts of the text and figures are taken. The theoretical results were obtained by Dmitry O. Krimer and myself, whereas the experiment was conducted by Andreas Angerer, Stefan Putz, Thomas Astner, Ralph Glattauer, and Kirill Streltsov under the supervision of Jörg Schmiedmayer and Johannes Majer from the Vienna Center for Quantum Science and Technology, Atominstitute, TU Wien. The experimental results of ref. [39] are also presented in the PhD theses of Andreas Angerer [168] and Stefan Putz [51].
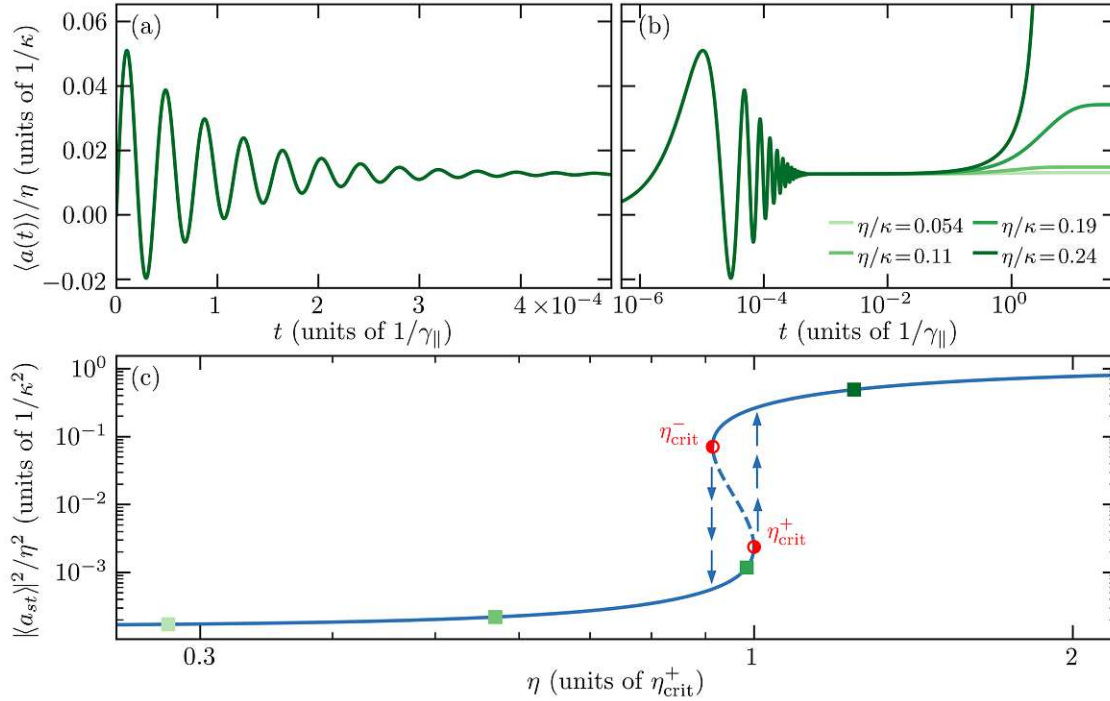
Figure 4.2.1.: (a,b) Transient dynamics of the cavity amplitude $\langle a(t) \rangle$ towards the steady-states [depicted in (c)] under the action of an external drive with constant amplitude $\eta/\kappa = 0.054, 0.11, 0.19, 0.24$ (light to dark green). The driving amplitude is switched on at $t = 0$, and time is given in units of $1/\gamma_\parallel$. Our numerical results are presented on (a) a linear time scale and (b) a logarithmic time scale to cover a much longer time interval. (c) Stationary solutions for the cavity probability amplitude $|\langle a_{st} \rangle|^2$ as a function of the driving amplitude η (log-log scale). Solid and dashed curves are stable and unstable solutions, respectively. The two critical points $\eta_{\text{crit}}^{\pm}$ at which they meet are saddle-node bifurcations. Under smooth sweeping of the amplitude η through the bistable region, the system shows a hysteresis behavior indicated by arrows. Green symbols are the stationary solutions to which the system eventually settles for the values of η from (a) and (b).

the case when a constant external driving field η is suddenly switched on at time $t = 0$ with the spins being initially in their ground state and no photons inside the cavity. The dynamics show two well-separated time scales: A fast time scale ($\sim 1/\kappa, 1/\gamma_\perp$) on which Rabi oscillations are clearly resolved [Fig.4.2.1(a)] and a much slower time scale ($\sim 1/\gamma_\parallel$) on which the system finally settles at its stationary state [Fig.4.2.1(b)]. The Rabi oscillations indicate that the system is in the strong-coupling regime due to the strong collective coupling of the ensemble to the cavity [35, 37]. The decoherence caused mainly by inhomogeneous broadening of the spin ensemble finally lets the oscillations disappear giving rise to a transient steady-state

regime at rather long times. Interestingly, this initial dynamics is purely linear as the ratio of the cavity amplitude to the amplitude of the driving signal, $\langle a(t) \rangle / \eta$, remains practically unaltered even for moderate values of η [all curves for different values of η lie on top of each other in Fig.4.2.1(a)]. As shown in Fig.4.2.1(b), only at much later times ($\sim 1/\gamma_\parallel$) the value of the cavity amplitude deviates from its linear steady-state value, starting to approach its ultimate stationary state with a strong dependence on η.

Figure 4.2.1(c) depicts the system's stationary states which we discussed already in the previous section. Recall that within the bistable interval, which is delimited by the critical points $\eta_{\text{crit}}^\pm$, three solutions to the steady-state Eq. (4.1) (two stable and one unstable) exist. In the classification of dynamical systems, $\eta_{\text{crit}}^\pm$ represent saddle-node bifurcations [197]. Here, two steady-state solutions merge and mutually annihilate such that outside the bistable interval, only a single solution remains. As demonstrated in Fig. 4.2.1(b), the stationary states are typically approached on a time scale given by the slowest inverse decay rate of the system, which in our case is $1/\gamma_\parallel$. Close to the saddle-node bifurcation points $\eta_{\text{crit}}^\pm$, however, this process can slow down dramatically so that the system settles at its steady-state on a time scale much larger than $1/\gamma_\parallel$. Before addressing this critical slowdown, we must introduce the concept of adiabatic elimination (see Appendix E) [198, 199]. This becomes necessary to solve the dynamics at extremely long time scales.

Adiabatic elimination

Taking into account that $\gamma_\parallel \ll \kappa, \gamma_\perp, \Omega$, we expect that all long-lived processes occur on time scales of the order of $\gamma_\parallel$. This allows us to eliminate the cavity amplitude $\langle a \rangle$ and the spin lowering expectation value $\langle \sigma_k^- \rangle$ from Eqs. (2.20a)-(2.20c), as these expectation values adiabatically follow the evolution of the z component of the spin operator expectation value $\langle \sigma_k^z \rangle$ at large times when $t \gg 1/\kappa, 1/\gamma_\perp, 1/\Omega$.

We first introduce the dimensionless time $\tau = \gamma_\parallel t$ and rewrite Eqs. (2.20a)-(2.20c) as

$$\frac{\gamma_\parallel}{\kappa} \frac{d}{d\tau} \langle a \rangle = -(1 + i\frac{\Delta_c}{\kappa}) \langle a \rangle - \frac{i}{\kappa} \sum_{k=1}^{N} g_k \langle \sigma_k^- \rangle + \frac{\eta}{\kappa} \tag{4.13}$$

$$\frac{\gamma_\parallel}{\gamma_\perp} \frac{d}{d\tau} \langle \sigma_k^- \rangle = -(1 + i\frac{\Delta_k}{\gamma_\perp}) \langle \sigma_k^- \rangle + i\frac{g_k}{\gamma_\perp} \langle \sigma_k^z \rangle \langle a \rangle \tag{4.14}$$

$$\frac{d}{d\tau} \langle \sigma_k^z \rangle = -(\langle \sigma_k^z \rangle + 1) - 4\frac{g_k}{\gamma_\parallel} \text{Im}(\langle \sigma_k^- \rangle \langle a^\dagger \rangle). \tag{4.15}$$

Next, from the inequalities $\gamma_\parallel/\kappa \ll 1$ and $\gamma_\parallel/\gamma_\perp \ll 1$, we infer that the time derivatives $d\langle a \rangle/d\tau$ and $d\langle \sigma_k^- \rangle/d\tau$ give only vanishing contributions at large times compared to the right-hand side of Eqs. (4.13)-(4.14). Straightforward calculations (see

Appendix E) then yield a single equation for $\langle \sigma_k^z \rangle$, which determines the dynamics of the whole coupled spin-cavity system at large time scales $\sim 1/\gamma_\parallel$:

$$\frac{d}{d\tau} \langle \sigma_k^z \rangle = -(1 + \langle \sigma_k^z \rangle) - \frac{\eta^2}{\kappa^2} \frac{\langle \sigma_k^z \rangle}{n_k(1 - \sum_l C_l \langle \sigma_l^z \rangle)^2}, \quad (4.16)$$

where the cooperativity parameter C_k and the photon saturation number n_k for the k-th spin are given by Eqs. (4.2) and (4.3), respectively. Furthermore, we used that the cavity is on resonance with the driving field $\omega_c = \omega_p$ and assumed that the spin distribution is always symmetric with respect to its central frequency $\omega_s = \omega_c$. The cavity amplitude is then given by

$$\langle a \rangle = \frac{\eta}{\kappa(1 - \sum_k C_k \langle \sigma_k^z \rangle)}. \quad (4.17)$$

From the derivation of the adiabatic elimination, it is clear that the above equations can not capture the fast initial dynamics showing a coherent energy exchange (Rabi oscillations) between the spin ensemble and the cavity. For large times, however, the fast variables $\langle a \rangle$ and $\langle \sigma_k^- \rangle$ adiabatically follow the evolution of $\langle \sigma_k^z \rangle$ and Eqs. (4.16) accurately account for the evolution of the entire system. At every instant of the slow time τ, the value of the cavity amplitude $\langle a \rangle$ and the spin operator $\langle \sigma_k^- \rangle$ are then determined by the spin components $\langle \sigma_k^z \rangle$.
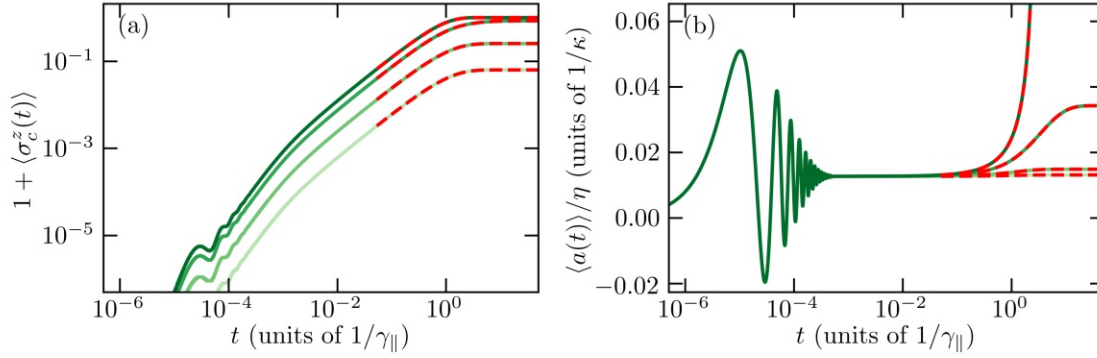
Figure 4.2.2.: (a) Expectation value of the central spin operator $\langle \sigma_c^z(t) \rangle$ ($\omega_k = \omega_c$), and (b) the cavity amplitude $\langle a(t) \rangle$ versus time t (in units of $1/\gamma_\parallel$) under the action of an external drive with constant amplitude. The values of η are chosen to be the same as those in Fig. 4.2.1(b). Here, we compare the numerical solutions of the full Maxwell-Bloch equations (solid lines) with the numerical solutions of Eqs. (4.16) and (4.17) obtained under adiabatic elimination (red dashed lines).

In Fig. 4.2.2, the results of the calculations under adiabatic elimination are compared with those obtained in the framework of the full Maxwell-Bloch equations (2.20a)-(2.20c). In the former case, Eqs. (4.16) are numerically solved with initial

conditions $\langle \sigma_k^z \rangle = -1$ (spin ensemble is in the ground state) and $\langle a \rangle$ is correspondingly found from Eq. (4.17). As can be seen from the figure above, the adiabatic elimination indeed is a good approximation for the system's evolution at large times after the transient oscillatory behavior disappears.

Besides the fact that calculations for long times become numerically less demanding, adiabatic elimination also provides additional insight into the dynamics of the bistable system. Although the derivative $d\langle a \rangle / d\tau$ was omitted in Eq. (4.13) owing to the vanishing prefactor as mentioned above, the slow variation of $\langle a \rangle$ can still be captured by differentiating the reduced Eq. (4.17) with respect to τ yielding

$$\frac{d}{d\tau}\langle a \rangle = \frac{\kappa}{\eta}\langle a \rangle^2 \sum_k C_k \frac{d\langle \sigma_k^z \rangle}{d\tau}, \tag{4.18}$$

where $d\langle \sigma_k^z \rangle / d\tau$ is determined by Eq. (4.16). If we now assume that all spins are in resonance, $\Delta_k = 0$ and $\langle \sigma_k^z \rangle = \langle \sigma^z \rangle$, Eq. (4.18) can be further simplified so that we obtain a single ordinary differential equation for the cavity amplitude [39],

$$\frac{d}{d\tau}\langle a \rangle = \langle a \rangle - \frac{\kappa}{\eta}(1+C)\langle a \rangle^2 + \frac{4\kappa C}{N\gamma_\parallel}\langle a \rangle^3 - \frac{4\kappa^2 C}{N\gamma_\parallel \eta}\langle a \rangle^4, \tag{4.19}$$

where C is the collective cooperativity of a homogeneous spin ensemble given by Eq. (4.5). Note that exactly at the critical points $\eta_{\mathrm{crit}}^\pm$, two steady states (one stable and one unstable fixed point) coalesce with each other, being solutions of the nonlinear algebraic equation $\dot{x} = f(x) = 0$ (the dot stands for the time derivative). When the control parameters are slightly detuned from this point, the system passes the corresponding region in phase space $(x, \dot{x})$ very slowly due to the proximity of the critical point. In the literature, this phenomenon is often referred to as a saddle-node "ghost" [197] since the phase trajectories are considerably delayed in their flow towards their actual stationary state.

In the presence of inhomogeneous broadening, we cannot set up a single differential equation for the cavity amplitude like Eq. (4.19) but have to resort to the full Maxwell-Bloch equations or their reduced form after adiabatic elimination [Eqs. (4.16) and (4.17)], respectively. Despite the more complicated form of the dynamic equations, we expect a similar critical slowing down in the case with inhomogeneous broadening.

Critical slowing down

In the following, we present the quench dynamics—i.e., the dynamics after a sudden parameter change—in the vicinity of the critical points $\eta_{\mathrm{crit}}^\pm$ from Fig. 4.2.1(c). Specifically, in Fig. 4.2.3(a) and (b) we take as initial conditions for $\langle a \rangle$ and $\langle \sigma_k^z \rangle$ a stationary solution located at the low transmission branch, e.g.: $\langle a \rangle = \eta/\kappa(1+C)$ and $\langle \sigma_k^z \rangle = -1$, and then suddenly change η to a value above η_{crit}^+ corresponding to

a solution on the high transmission branch. We repeat this procedure for driving amplitudes that are closer and closer to the critical point η_{crit}^+. A similar test is performed for the lower critical point η_{crit}^- [see Fig. 4.2.3(c) and (d)]. Here, we start from a stationary state located on the high transmission branch ($\langle a \rangle \sim \eta/\kappa$, $\langle \sigma_k^z \rangle = 0$) and abruptly change η to values slightly below η_{crit}^-. In both cases, the transient times increase dramatically as the driving amplitude approaches the critical points $\eta_{\text{crit}}^\pm$, and the evolution of the system becomes much slower than the largest intrinsic time scale $1/\gamma_\parallel$. This behavior is indicative for the phenomenon of critical slowing down in systems exhibiting a saddle-node bifurcation [124, 200, 201].

To further characterize the critical slowing down dynamics, we present several phase trajectories in Fig. 4.2.4(a) and (c). The closer the driving amplitude η is to the critical value at which the upper or lower saddle-node bifurcation occurs, the more and more time the system spends near a narrow slowing down region in phase space [gray areas in Fig. 4.2.4(a) and (c)]. Here, the value of $d\langle a \rangle^2/dt$ drops to very small values indicated by a dip in the phase trajectories. Right at the critical points $\eta_{\text{crit}}^\pm$, the time T the system spends in the slowing down region diverges as presented in Fig. 4.2.4(b) and (d). Such a singular behavior is explained by the vanishing velocity $d\langle a \rangle^2/dt$ at the critical points. Notably, this divergence shows a power law scaling

$$T = T_0 + \beta|\eta - \eta_{\text{crit}}^\pm|^{-\alpha}, \qquad (4.20)$$

where the critical exponent is extracted to be $\alpha = 0.52$ for η_{crit}^+ and $\alpha = 0.53$ for η_{crit}^-, respectively. Both values, therefore, only slightly exceed the well-known square-root scaling law, $\alpha = 0.5$, for the simplest normal form of a nondegenerate saddle-node bifurcation $dx/dt = r + x^2$, where $x \in \mathbb{R}$ and $r \leq 0$ is the bifurcation parameter [201].

Such scaling similarities can be traced back to very generic features of continuous phase transitions at which a system becomes scale invariant and is characterized by an infinite correlation length and time. Specifically, both correlation length and time demonstrate power-law divergence upon changing the external parameter in the vicinity of the phase transition [202]. Moreover, a set of critical exponents can be the same for a certain class of phase transitions, which share the same symmetries and dimensionality. This phenomenon, referred to as "universality" [202], can be understood by divergent correlations at the phase transition giving rise to smearing out of the system's complexity nearby it. Therefore, a very complex system can respond similarly as a very simple one provided that both are sufficiently close to the phase transition—a scenario which is realized in our case as well.

Finally, we demonstrate the phenomenon of critical slowing down for the same physical setup based on a superconducting microwave resonator and a large ensemble of NV centers in diamond [39, 51, 168], which was presented already in the previous section. Figure 4.2.5(a) depicts the quench dynamics of the transmission
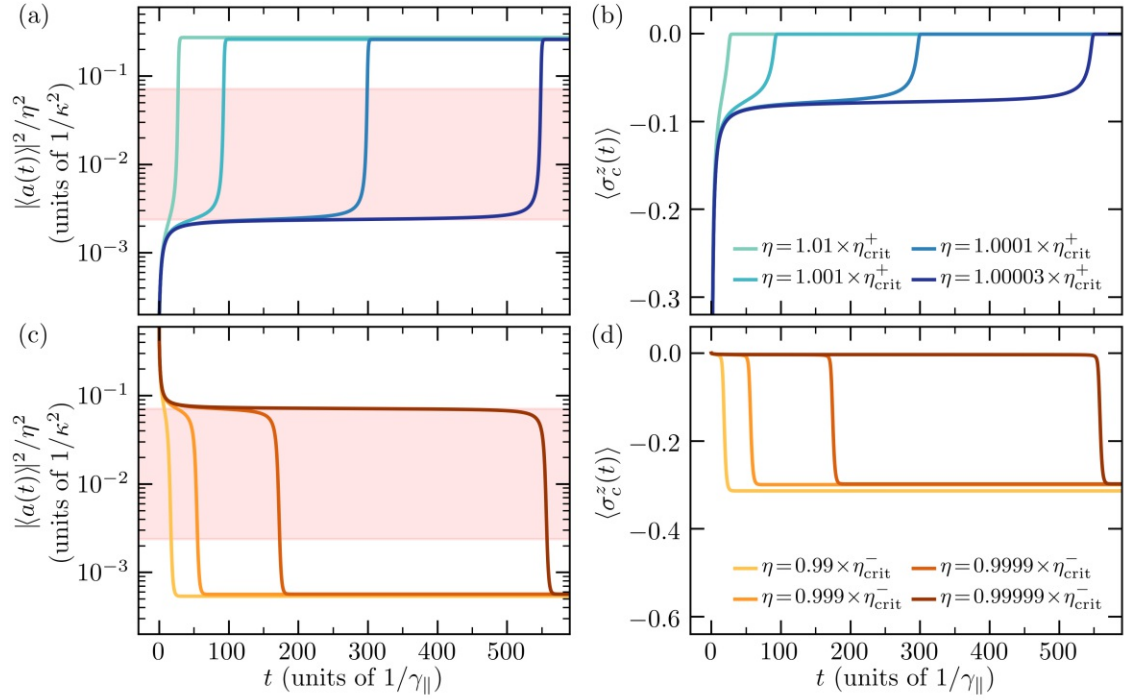
Figure 4.2.3.: Critical slowing down of the transient quench dynamics in the vicinity of the critical points η_{crit}^+ and η_{crit}^-. (a,c) Cavity probability amplitude squared $|\langle a(t)\rangle|^2$ and (b,d) expectation value of the central spin operator $\langle \sigma_c^z(t)\rangle$ ($\omega_k = \omega_c$) as a function of time t (in units of $1/\gamma_\parallel$). (a,b) As initial condition a stationary state on the low transmission branch is chosen, which lies far from the bistable regime. The driving strength is then increased abruptly to values slightly above η_{crit}^+ so that the system approaches the high transmission branch. (c,d) same as (a,b) but with reversed directions such that the system starts out at the high transmission branch and ends up at the low transmission branch after a sudden decrease of η below η_{crit}^-. The closer the driving amplitude is to the critical values η_{crit}^+ and η_{crit}^-, respectively, the longer the transient times become (light to dark curves). The red shaded regions designate a gap in values of $|\langle a_{st}\rangle|^2$, where no stable stationary solution exists [see Fig. 4.2.1(c)].

through the cavity for a spin ensemble with a collective cooperativity of $C \approx 78$ ($\kappa/2\pi = 0.44$ MHz, $\gamma_\perp/2\pi = 33$ kHz). In the experiment, which is performed in the group of Jörg Schmiedmayer, the system is prepared in an initial state lying on the high transmission branch [see Fig. 4.1.4(c)]. This is achieved by setting the cavity input power to $P_{\text{in}} \gg P_{\text{in}}^+$ for several minutes. The input power is then nonadiabatically switched to a smaller value. This measurement is repeated several times, with the system always prepared in the same initial state but switching to a different target driving power. Note that, when the system is driven with powers slightly below P_{in}^-, the time scales needed to settle in a stationary state become as
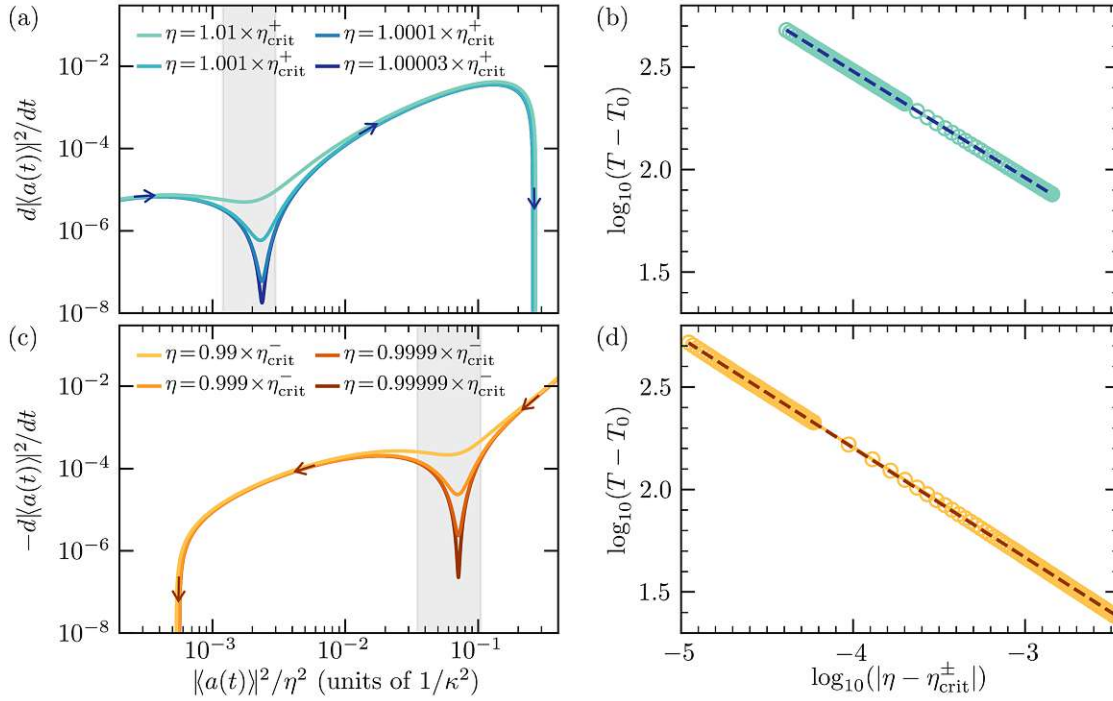
Figure 4.2.4.: Phase portraits and scaling for the quench dynamics presented in Fig. 4.2.3 showing a critical slowing down near the critical points $\eta_{\text{crit}}^{\pm}$. (a) Phase trajectories in the $[d|\langle a(t)\rangle|^2/dt, |\langle a(t)\rangle|^2]$ plane for the dynamics in the vicinity of η_{crit}^{+}. (b) The time duration $T - T_0$ (measured in units of $1/\gamma_{\parallel}$) needed to pass the slowing-down region [gray area in (a)] versus $\log_{10}(|\eta - \eta_{\text{crit}}|)$ is displayed by colored circles. The dashed line represents the algebraic fit $T - T_0 = \beta|\eta - \eta_{\text{crit}}^{+}|^{-\alpha}$, with the exponent $\alpha = 0.52$, $T_0 = -74.7$, and $\beta = 2.54$. (c,d) Corresponding plots for the dynamics near η_{crit}^{-}. Here, the fit parameters are given by $\alpha = 0.53$, $T_0 = -6.25$, and $\beta = 1.16$. Arrows in (a) and (c) indicate the system's evolution in time.

long as 4×10^4 s, which is much longer than ever observed for this effect. In Fig. 4.2.5(c) we present the transient switching time t_{switch} characterizing the time scale the system needs to reach its stationary state. We define this time as the inverse of the smallest rate $d|T|^2/dt$. The measurements suggest a power law divergence of the switching time $t_{\text{switch}} \approx |P_{\text{in}} - P_{\text{crit}}^{-}|^{-2\alpha}$ with $2\alpha = 1.20 \pm 0.04$, which is in reasonable agreement with our theoretical results presented in Fig. 4.2.4(d). Note that in comparison with Eq. (4.20) the additional factor of two in the critical exponent arises from the use of the power $P_{\text{in}} \approx \eta^2/\kappa^2$ instead of the amplitude η.
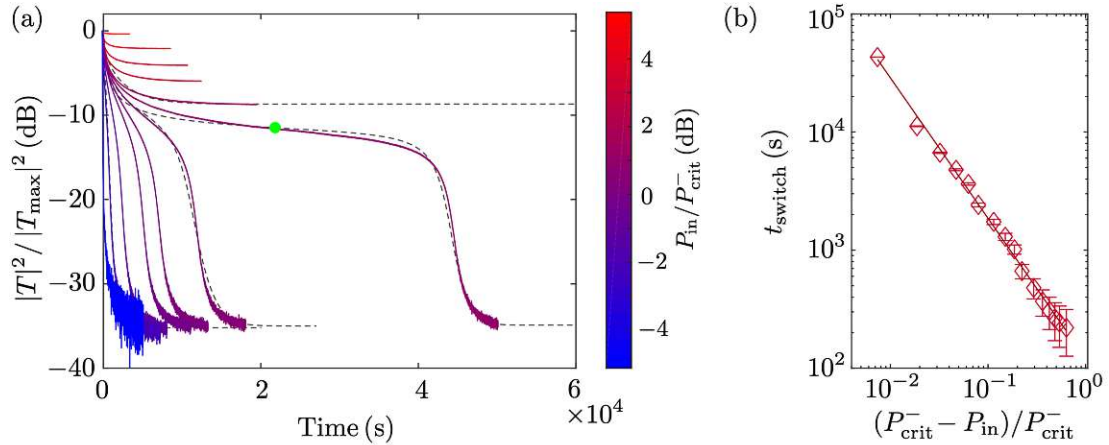
Figure 4.2.5.: Measurement of the quench dynamics of an ensemble of NV centers with high cooperativity $C \approx 78$ coupled to a superconducting microwave resonator [39]. The cavity is strongly driven so that the system's initial state is on the high transmission branch. At $t = 0$ the driving power is suddenly switched to a different target value. (a) Normalized cavity transmission versus time for different target drive powers P_{in}. For powers slightly below the critical point P_{crit}^{-}, the time it takes the system to settle at its stationary state is extremely prolonged and approaches 4×10^4 s. The dashed lines correspond to numerical calculations using Eq. (4.18). (b) Switching time between the high and low transmission branch in the vicinity of the critical driving power P_{crit}^{-}. We define the switching time t_{switch} as the inverse of the smallest gradient for a given curve [green dot in (a)]. Close to P_{crit}^{-}, the switching time diverges. The solid red line is a fit to the algebraic function $t_{\mathrm{switch}} = |P_{\mathrm{in}} - P_{\mathrm{crit}}^{-}|^{-\alpha}$ (with $\alpha = 1.20 \pm 0.4$). Figure adapted from ref. [39].

4.3. Semiclassical-to-quantum boundary[7]

In the previous sections, we have described optical bistability on a semiclassical basis using Maxwell-Bloch equations and completely ignored all quantum fluctuations. This mean-field description becomes exact in the thermodynamic limit $N \to \infty$ [114] and is well justified for the presented ensemble of nitrogen-vacancy centers, which contains about $N \approx 10^{12}$ spins [39]. However, as the number of spins within the ensemble decreases, fluctuations become more significant and must be included in the theoretical model. While in the semiclassical description two stable stationary states—one with low transmission and one with high transmission—can coexist, a quantum mechanical model of bistability predicts only a single transmission value for the same parameters. This difference is caused by quantum fluctuations which destabilize the semiclassical solutions and trigger a switching of the system between

---

[7] The figures and parts of the text in this section are taken from our published work in ref. [83]. All figures and numerical results were produced by myself.

low and high transmission [156]. The switching smears out the two semiclassical expectation values and is characterized by a bimodal quantum mechanical probability distribution [102, 166, 203]. In the limit of large spin ensembles, the switching times of the system diverge and the two stable semiclassical solutions are restored [166, 203]. The natural question that arises is how many spins are required to enter this semiclassical regime.

To answer this question, we use the second- (CE2) and third-order cumulant expansion (CE3) introduced in Section 3.1 to calculate quantum corrections to the semiclassical Maxwell-Bloch equations. In particular, we focus on deviations from the semiclassical solution in the stationary transmission through the cavity under constant driving η. The stationary transmission, which is proportional to the stationary cavity probability amplitude $|\langle a_{st} \rangle|^2$ can be obtained either by directly solving the corresponding steady-state equations as in Section 4.1 or by a temporal evolution of the system for sufficiently long time. For simplicity, we assume homogeneous coupling ($g_k = g$) and radiative decay only ($\gamma_p = 0$).

The semiclassical-to-quantum boundary for homogeneous spin ensembles

We start with the simple case of homogeneous broadening, where all spins are on resonance with the cavity and the driving frequency ($\Delta_k = 0$, $\Delta_c = 0$). Recall that the semiclassical Maxwell-Bloch equations (2.20a)-(2.20c) are invariant to changes in the number of spins N under the transformation

$$g_j \to g_j/\sqrt{N}, \quad \langle a \rangle \to \langle a \rangle \sqrt{N}, \quad \eta \to \eta\sqrt{N}. \tag{4.21}$$

Note that such a re-scaling is impossible for the equations of motion that involve higher-order expectation values. Hence, the stationary states obtained from the CE2 and CE3 will explicitly depend on the number of spins N. Figure 4.3.1 depicts the quantum corrections to the semiclassical steady-state cavity probability amplitude $|\langle a_{st} \rangle|^2$ for a collective cooperativity parameter of $C = 14$ (with the tendency described below being similar for all C). We present typical numerical results from the CE2 and CE3 for ten different driving strengths, chosen to allow us to study the stationary states on both the lower transmission branch within the bistable region and the upper transmission branch above the critical point η_{crit}^+.

The results in Fig. 4.3.1 show that, for small ensembles, the stationary transmission calculated using the CE2 and CE3 deviate significantly from the semiclassical solution. Notably, this deviation occurs not only within the bistable region but also for driving strengths above the critical point η_{crit}^+. As expected, increasing the number of spins restores the semiclassical results as the quantum fluctuations decrease with $1/N$ [102]. However, the actual number of spins needed for the CE to agree well with the semiclassical solution substantially increases for driving strengths close to the critical point η_{crit}^+. While the results obtained from the CE3 for spin
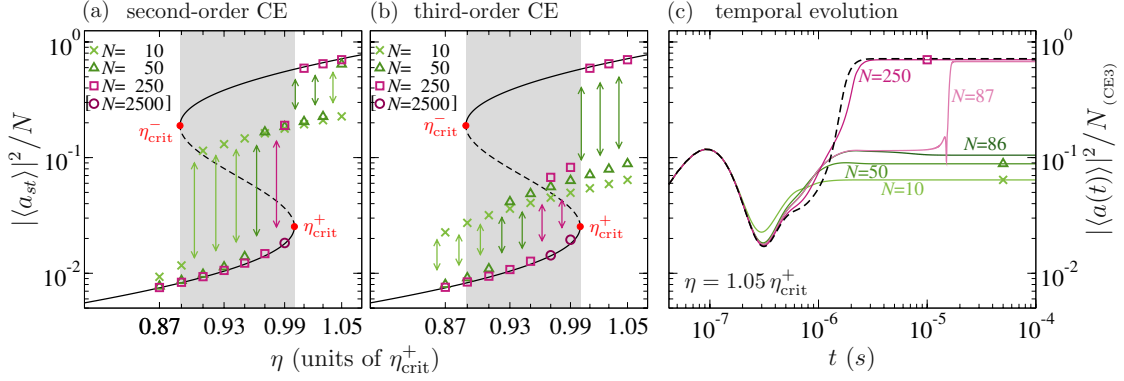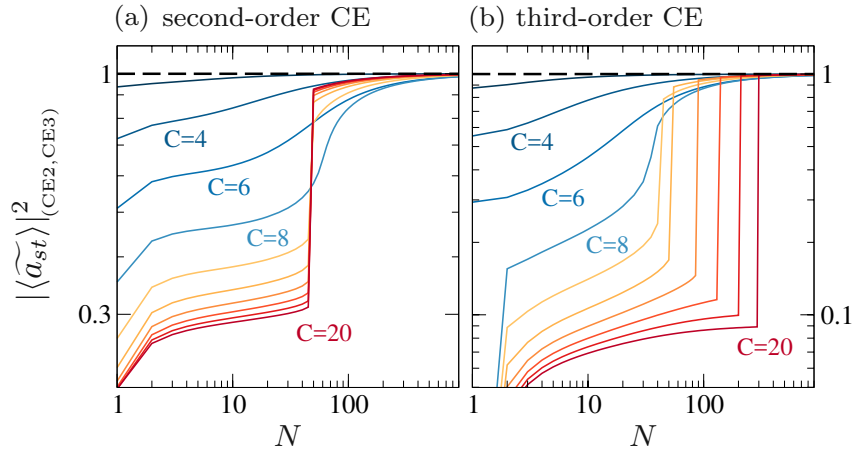
Figure 4.3.1.: Deviations from the semiclassical cavity probability amplitude for a co-operativity parameter $C = 14$ (with $\kappa = 2\gamma_h = 2\pi \times 1$ MHz) and different numbers of spins inside the ensemble. (a,b) Stationary solutions for the cavity probability amplitude $|\langle a_{st} \rangle|^2$ as a function of the driving amplitude η. For comparison, the semiclassical result is shown as black solid line. Amplitude bistability is marked by two critical points $\eta_{crit}^{\pm}$ (red dots) with a bistable region in between (gray area). At well defined driving amplitudes, corrections to the semiclassical solutions are calculated using (a) the second- and (b) third-order cumulant expansion (CE) for different numbers of spins $N = 10, 50, 250$, and 2500. For reasons of clarity, results for the latter are presented only for driving strengths close to the critical point of the lower transmission branch η_{crit}^{+}. The colored arrows indicate the deviations from the corresponding semiclassical transmission curve. (c) Temporal evolution of the cavity probability amplitude $|\langle a(t) \rangle|^2_{(CE3)}$ using the third-order cumulant expansion (CE) and for the driving strength $\eta = 1.05 \cdot \eta_{crit}^{+}$. The initial conditions are chosen such that at $t = 0$ the spin ensemble is unexcited and the cavity is empty. Results are shown for increasing numbers of spins, $N = 10, 50, 86, 87$, and 250. The semiclassical solution is shown as black dashed line. The colored symbols indicate the stationary states shown in (b).

ensembles of moderate size ($N = 250$) agree reasonably well with the semiclassical solution for most driving strengths, this is not the case for driving strengths close to the critical point of the low transmission branch $0.97 \cdot \eta_{crit}^{+}$ and $0.99 \cdot \eta_{crit}^{+}$, respectively. Here much larger numbers of spins ($N = 2500$) are needed for the CE3 to approach the semiclassical solution lying on the low transmission branch. The stationary states shown in Fig. 4.3.1(a) and (b) are extracted from a temporal evolution of the system for sufficiently long time starting initially from an unexcited spin ensemble ($\langle \sigma_k^z \rangle = -1$, $\langle \sigma_k^- \rangle = 0$) and an empty cavity ($\langle a \rangle = 0$), subjected to constant driving. For this initial state the semiclassical dynamics converges towards the lower transmission branch of the bistable region and reaches the upper transmission branch only for $\eta > \eta_{crit}^{+}$ as discussed in Section 4.1.

The transient dynamics of the cavity probability amplitude $|\langle a(t) \rangle|^2_{(CE3)}$ calculated using the CE3 for $C = 14$ and driving strength $\eta = 1.05 \cdot \eta_{crit}^{+}$ is presented in

Figure 4.3.2.: Comparison of the second- and third-order cumulant expansion (CE) with the semiclassical cavity transmission for the driving strength $\eta = 1.05 \cdot \eta_{\mathrm{crit}}^{+}$. The normalized stationary state solutions for the cavity probability amplitude $|\langle \widetilde{a_{st}} \rangle|^2_{(\mathrm{CE2,3})} = |\langle a_{st} \rangle|^2_{(\mathrm{CE2,3})} / |\langle a_{st} \rangle|^2_{(\mathrm{CE1})}$ is shown as a function of the number of spins N using (a) the second- (CE2) and (b) the third-order cumulant expansion (CE3), respectively. Results are shown for cooperativity parameters $C = 2$ (dark blue) to 20 (dark red). $|\langle \widetilde{a_{st}} \rangle|^2_{(\mathrm{CE2,3})} = 1$ (dashed black line) corresponds to the semiclassical result.

Fig. 4.3.1(c). As indicated already in Fig. 4.3.1(b) for $N = 250$ the results obtained from the CE3 agree well with the semiclassical solution, whereas for small spin ensembles ($N = 10$ or 50) the CE3 tends towards a stationary state of much lower transmission than that predicted by the semiclassical equations. Interestingly, our calculations show an abrupt transition from spin ensembles with large deviations from the semiclassical limit to spin ensembles where such deviations are small. Whereas for $N \leq 86$ the CE3 tends towards a stationary state of relatively low transmission, ensembles of $N \geq 87$ spins approach a state of high transmission, following the semiclassical solution.

To compare the validity of the semiclassical approximation for different driving strengths η and cooperativity parameters C, we normalize the stationary state obtained in the framework of the CE2 and CE3 by the corresponding semiclassical result (CE1),

$$|\langle \widetilde{a_{st}} \rangle|^2_{(\mathrm{CE2,3})} \equiv \frac{|\langle a_{st} \rangle|^2_{(\mathrm{CE2,3})}}{|\langle a_{st} \rangle|^2_{(\mathrm{CE1})}}, \tag{4.22}$$

such that a value close to unity indicates being close to the semiclassical regime. In Fig. 4.3.2 we present the normalized cavity probability amplitude $|\langle \widetilde{a_{st}} \rangle|^2_{(\mathrm{CE2,3})}$ for the driving strength $1.05 \cdot \eta_{\mathrm{crit}}^{+}$ and cooperativity parameters ranging from $C = 2$ to 20. Focusing at first on the CE2 solutions, we see that the normalized cavity probability amplitude approaches the semiclassical result $|\langle \widetilde{a_{st}} \rangle|^2_{(\mathrm{CE2})} = 1$ for increasing numbers

of spins. As indicated above, the transition towards the semiclassical solution becomes more abrupt for increasing C and for $C > 8$ even resembles a first-order phase transition at $N \approx 45$.

If we turn now to the CE3 solutions, a similar tendency is observed with the only difference that the transition is shifted to larger values of N for increasing cooperativities C. While these findings suggest that the transition from systems of large fluctuations towards systems of small fluctuations has a discontinuous nature, caution should be taken since in the cross-over region the cumulant expansion has not yet converged, i.e., the CE2 and CE3 give quite different values for $|\langle a_{st}\rangle|^2$. Including higher orders of cumulants or a full quantum mechanical treatment of the problem is therefore required to validate results in this parameter regime.

Furthermore, it turns out that at values of η slightly smaller than η_{crit}^+ (at which the first-order transition obtained in the framework of the semiclassical approach occurs), other time-dependent solutions can simultaneously exist for certain numbers of spins N—a common scenario for systems governed by nonlinear differential equations. Specifically, starting from the simple initial conditions mentioned above (empty cavity with unexcited spin ensemble) can result in periodic long-time solutions or even numerically unstable trajectories with unphysical values of $|\langle \sigma_k^z \rangle| > 1$. To overcome such problems we vary the initial conditions for $\langle \sigma_k^z \rangle$ between -1 and -0.5 to finally find those which lie in the so-called basin of attraction for the stationary state. Originating from these initial conditions, the system finally settles to the stationary state under study as time increases.

We avoid the difficulties in the cross-over region of Fig. 4.3.2 by focusing on the results of the cumulant expansion close to the semiclassical stationary states. Thereby, we establish a criterion for the validity of the semiclassical Maxwell-Bloch equations based on the convergence of the cumulant expansion. For this purpose, we define the relative deviations

$$\Delta_{n-m}^{\mathrm{CE}} \equiv \frac{\left| |\langle a_{st}\rangle|_{(n)}^2 - |\langle a_{st}\rangle|_{(m)}^2 \right|}{|\langle a_{st}\rangle|_{(m)}^2} \, , \tag{4.23}$$

where n and m stand for the different orders of the cumulant expansion, CE1, CE2, and CE3. Recall that the first-order cumulant expansion (CE1) corresponds to the Maxwell-Bloch equations. In Fig. 4.3.3 we presents the relative deviations between the first three orders of the cumulant expansion, $\Delta_{1-2}^{\mathrm{CE}}$, $\Delta_{2-3}^{\mathrm{CE}}$, and $\Delta_{1-3}^{\mathrm{CE}}$, for $C = 14$ and driving strengths $\eta = 1.05 \cdot \eta_{\mathrm{crit}}^+$ and $0.95 \cdot \eta_{\mathrm{crit}}^+$, respectively. The discontinuous nature of the transition region is also found in the relative deviations, leading to a intricate dependence on the number of spins N. However, for large N the relative deviations start to decrease linearly with $1/N$ as expected from a linearized theory of quantum fluctuations in the small noise limit [78]. Note that the size of the relative deviations does not only strongly depend on the cooperativity C and the number of spins N but also on the driving strength η. Our results reveal that,
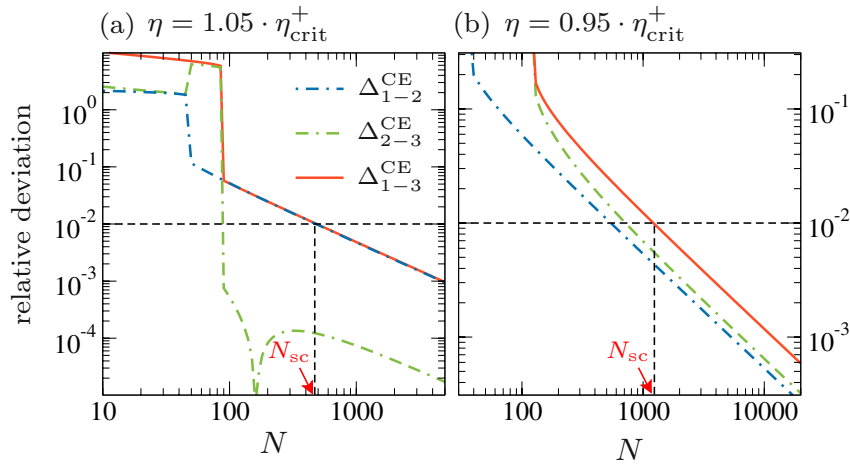
Figure 4.3.3.: Relative deviations in the cavity probability amplitude $|\langle a_{st} \rangle|^2$ calculated using the semiclassical Maxwell-Bloch equations (CE1), the second- (CE2), and the third-order cumulant expansion (CE3). Results are shown for cooperativity $C = 14$ and driving strengths (a) $\eta = 1.05 \cdot \eta_{\text{crit}}^+$ and (b) $\eta = 0.95 \cdot \eta_{\text{crit}}^+$. The relative deviations are defined as $\Delta_{n-m}^{\text{CE}} \equiv \left| |\langle a_{st} \rangle|^2_{(n)} - |\langle a_{st} \rangle|^2_{(m)} \right| / |\langle a_{st} \rangle|^2_{(m)}$, where n and m stand for the CE1, CE2, and CE3, respectively. The horizontal black dashed line indicates the threshold of convergence, which we set to be $\delta\epsilon = 10^{-2}$. Only if all three relative deviations, Δ_{1-2}^{CE} (blue dashed-dotted line), Δ_{2-3}^{CE} (green double-dashed-dotted line), and Δ_{1-3}^{CE} (orange solid line) are smaller than $\delta\epsilon$, the semiclassical solution for the cavity probability amplitude $|\langle a_{st} \rangle|^2$ is reliable. The minimal ensemble size that fulfills this criterion is denoted as N_{sc} (vertical black dashed line).

even for the same C and the same N, the relative deviations Δ_{n-m}^{CE} are significantly larger for driving strengths below the critical point ($\eta = 0.95 \cdot \eta_{\text{crit}}^+$) than for driving strengths above this point ($\eta = 1.05 \cdot \eta_{\text{crit}}^+$). This asymmetry will be explored in more detail below.

Using the relative deviations Δ_{n-m}^{CE}, we are now finally able to fulfill our primary goal: finding a minimum value for the number of spins N that allows a semiclassical description based on the Maxwell-Bloch equations. Therefore, we define a small threshold value $\delta\epsilon = 10^{-2}$, which serves as criterion for the convergence of the cumulant expansion. In the following, we estimate the minimal number of spins, N_{sc}, for which all relative deviations drop below this threshold, i.e.

$$\Delta_{1-2}^{\text{CE}}, \ \Delta_{2-3}^{\text{CE}}, \ \Delta_{1-3}^{\text{CE}} < \delta\epsilon \ , \tag{4.24}$$

and call this the semiclassical-to-quantum boundary. Hence, for spin ensembles with $N > N_{\text{sc}}$ the semiclasscial Maxwell-Bloch equations provide trustful results for the cavity probability amplitude $|\langle a_{st} \rangle|^2$ and all higher correlations like $\langle \sigma_j^z a \rangle_c$, $\langle \sigma_j^- a^\dagger \rangle_c$, etc., give only negligible relative contributions (lower than 1%).

The vanishing of these quantum correlations, characterized by Eq.(4.24), captures a subtle but important point of open quantum systems. While the stationary state

of the master equation (1.7) is unique, the bistability of the semiclassical regime translates into a bimodality of the corresponding quasi-probability function. Triggered by quantum fluctuations, the system switches between the two local maxima of the bimodal quasi-probability function. This gives a unique time averaged expectation value that can be quite different from the semiclassical solution [102, 166]. However, as the quantum fluctuations vanish with increasing system size N, the switching time diverges [166] and the dynamics stabilize along one of the two semiclassical transmission branches. Hence, the convergence criterion established in Eq. (4.24) implies that for $N > N_{\mathrm{sc}}$, the cavity probability amplitude $|\langle a_{st}\rangle|^2$ calculated from a full quantum mechanical evolution of the intitial state can not be distinguished from the solutions of the semiclassical Maxwell-Bloch equations on relevant time scales.
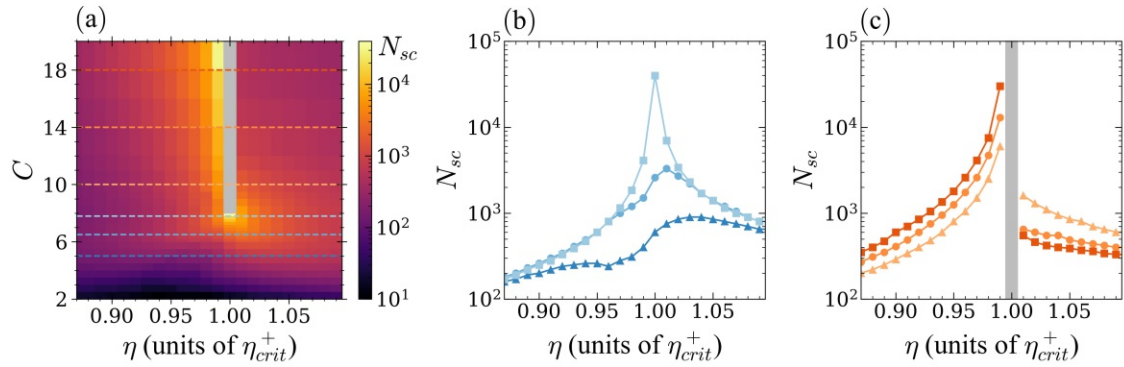
Figure 4.3.4.: Semiclassical-to-quantum boundary: Minimal number of spins N_{sc} for which the cumulant expansion converges towards the semiclassical results, i.e., for which condition (4.24) is fulfilled. (a) N_{sc} as a function of the driving strength η and the cooperativity parameter C. Note that N_{sc} drastically increases in the vicinity of the critical point η^+_{crit} for $C \geq 8$ and no data is available in this region (gray bar). The horizontal dashed lines correspond to cooperativity parameters, which are shown separately in (b) and (c), respectively. (b) N_{sc} as a function of the driving strength η for $C = 5.0$, 6.5, and 7.8 (dark to light blue). (c) N_{sc} as a function of the the driving strength η for $C = 10$, 14, and 18 (light to dark orange).

Figure 4.3.4 depicts this semiclassical-to-quantum boundary value as a function of both the cooperativity parameters C and the driving strength η. In the vicinity of the critical point η^+_{crit}, the value of N_{sc} increases dramatically. Exactly at $\eta = \eta^+_{\mathrm{crit}}$ the time the systems needs to reach its stationary state for $C \geq 8$ diverges as discussed in the previous previous, and data points are therefore omitted for these parameters. Below the bistability threshold, $C < 8$, where there is no bistability and also no critical point (see Eq.(4.10)), we take the driving strength where the slope of the input-output relation $d|\langle a_{st}\rangle|^2/d\eta$ is maximal as our reference point η^+_{crit}. Here the value of the semiclassical-to-quantum boundary N_{sc} has its maximum at driving strengths slightly above the driving strength η^+_{crit}. N_{sc} starts to peak at

$\eta = \eta_{\mathrm{crit}}^{+}$ as C approaches the threshold value of bistability. As can be seen in Fig. 4.3.4(b) for the cooperativity parameter $C = 5$ the value of N_{sc} above η_{crit}^{+} is significantly larger than below that driving strength. This asymmetry with respect to η_{crit}^{+} becomes less pronounced but is still present for increasing cooperativities up to $C \leq 8$. The peak in N_{sc} for $C = 7.8$ at the critical driving is the precursor to the emergence of a first-order phase transition and the effect of bistability, which emerges for cooperativity values above $C = 8$.

It is worth noting that for $C > 8$ the semiclassical-to-quantum boundary as defined in Eq. (4.24) behaves qualitatively different for the lower transmission branch as compared to the upper transmission branch. This asymmetry can be understood from our choice to probe the upper critical point η_{crit}^{+}. Below this point, we have bistability, so even though we are probing the low transmission branch, a high transmission branch is also present for these parameters. As we approach the critical point η_{crit}^{+} from below, the value N_{sc} progressively increases and eventually diverges exactly at η_{crit}^{+}, where a saddle-node bifurcation occurs [curves from the left with respect to the gray bar of Fig. 4.3.4(c)]. In contrast, above the critical point η_{crit}^{+} the is only one stable solution in form of the upper transmission branch. In the system's phase space these solutions are far from the saddle-node bifurcation at η_{crit}^{+}. Therefore, as we approach η_{crit}^{+} from above, the value of N_{sc} exhibits no divergence and is significantly smaller than below η_{crit}^{+}.

Another interesting observation from Fig. 4.3.4(c) is that for the lower transmission branch ($\eta < \eta_{\mathrm{crit}}^{+}$), N_{sc} increases for increasing cooperativity parameters C. In contrast, for the upper transmission branch ($\eta > \eta_{\mathrm{crit}}^{+}$), N_{sc} decreases for increasing C. The cooperativity of the spin ensemble therefore seems to play a dual role: Within the bistable region, a high cooperativity amplifies fluctuations that cause a deviation from the semiclassical solution, whereas, outside the bistable domain, a high cooperativity suppresses them and facilitates a rapid convergence to the single stationary state.

Our findings suggest that close to the critical point at the lower transmission branch even very large ensembles of up to $\sim 10^{4}$ spins can not be accurately described by the semiclassical Maxwell-Bloch equations. Note that for large cooperativities the differences in N_{sc} for driving strengths within and outside the bistable region become very large. Whereas for $C = 18$ and $\eta = 1.01 \cdot \eta_{\mathrm{crit}}^{+}$ the semiclassical result agrees well (1% deviation) with the CE2 and CE3 already for ensembles of $N_{\mathrm{sc}} \approx 500$ spins, the corresponding value grows to $N_{\mathrm{sc}} \approx 3 \cdot 10^{4}$ for $\eta = 0.99 \cdot \eta_{\mathrm{crit}}^{+}$. This can be explained by very large quantum fluctuations near the critical point, which destabilize one of the two semiclassical basins of attraction.
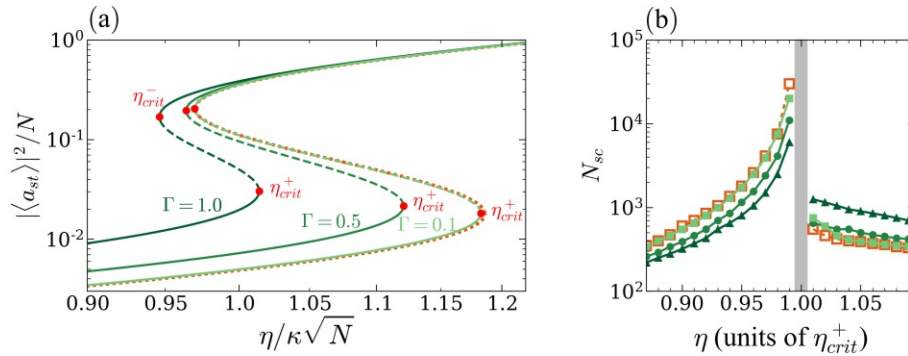
Figure 4.3.5.: Semiclassical-to-quantum boundary including inhomogeneous broadening: (a) Semiclassical stationary states for the cavity probability amplitude $|\langle a_{st} \rangle|^2$ as a function of the driving amplitude η. Results are shown for Gaussian spin distributions with a width (FWHM) of $\Gamma = 0.1$, 0.5, and 1.0 MHz, corresponding to a collective cooperativity of $C \approx 17.9$, 15.8, and 12.7, respectively (light to dark green). Results without inhomogeneous broadening, corresponding to $C = 18$, are presented for comparison purposes (dotted orange line). (b) Semiclassical-to-quantum boundary N_{sc} as a function of the the driving strength η for $\Gamma = 0.1$, 0.5, 1.0 MHz (light to dark green), and no inhomogeneous broadening (orange).

The semiclassical-to-quantum boundary for inhomogeneously broadened spin ensembles

In the following, we examine how inhomogeneous broadening affects the previously defined semiclassical-to-quantum boundary. For this purpose, we assume that the individual spin frequencies Δ_k follow a Gaussian distribution. This scenario becomes computationally much more demanding, since now the coupled equations of motion have to be solved for each spin frequency individually. Following the procedure described in the Appendix C, we split the spin ensemble into $L = 51$ equidistantly spaced frequency clusters to make our problem numerically tractable.

In Fig. 4.3.5(a) we present the semiclassical stationary states of the cavity probability amplitude $|\langle a_{st} \rangle|^2$ for Gaussian spin distributions of three different widths (FWHM), $\Gamma = 0.1$, 0.5, and 1.0 MHz. For comparison we also show the bistability curve of a homogeneous spin ensemble with a collective cooperativity of $C = 18$. Note that an increase of the width Γ leads to a decrease of the collective cooperativity, given by Eq. (4.2). Here, $\Gamma = 0.1$, 0.5, and 1.0 MHz correspond to cooperativity values of $C \approx 17.9$, 15.8, and 12.7, respectively.

The minimal number of spins, N_{sc}, for which the cumulant expansion converges towards the semiclassical results is depicted in Fig. 4.3.5(b). A comparison with Fig. 4.3.4(c) indicates that the change in the semiclassical-to-quantum boundary due to the inhomogeneous broadening can be explained by the change in the collective cooperativity parameter C. Our results demonstrate that also inhomogeneously

broadened spin ensembles containing about 10^4 spins can show non-semiclassical behavior close to the critical point of bistability.

Chapter 5.

Atomic frequency combs and spectral engineering

So far, we have dealt with spin ensembles whose spectral distribution naturally follows a single Gaussian or q-Gaussian function due to the inhomogeneous broadening by different local environments within the host material. In this chapter, we proceed with spin ensembles with artificially designed spectral spin distributions. In particular, we focus on comb-shaped spin ensembles, known as atomic frequency combs [61, 62], which are promising candidates for future quantum memories by offering long storage times [63, 64], on-demand readout [63–66], and high multimode capacity [62, 67, 68].

The distinctive feature of an atomic frequency comb is the comb-shaped frequency distribution of the spin ensemble leading to a periodic absorption and subsequent emission of photons at well-defined times. Notably, this enables the storage of pulses containing both single and entangled photons [204–207]. While it has been shown that such quantum protocols achieve very high efficiencies by coupling the atomic frequency comb to an impedance-matched cavity [65, 206, 208–211], the strong coupling regime is widely unexplored. This chapter aims to fill this gap by providing a rigorous treatment of strongly coupled spin-cavity systems featuring a comb-shaped spectral spin distribution.

We start with macroscopic spin ensembles using the Volterra integral formalism presented in Section 2.1 introducing the concept of multimode strong coupling [212], which lays the foundation for understanding the operating principle of atomic frequency combs in cavities. Here we also show how one major limitation, i.e., the dephasing due to inhomogeneous broadening, can be overcome by spectral hole burning [84]. Then we switch to mesoscopic spin ensembles, which we treat at a fully quantum mechanical level using the variational renormalization group method introduced in Section 3.2. While most previous studies on atomic frequency combs have focused on the information stored in the amplitude and the relative phase of incoming pulses [213], we focus on the quantum mechanical phase space of the cavity, which has not received much attention. Our results reveal that arbitrary multi-photon states in the cavity are almost perfectly absorbed by the spin ensem-

ble and re-emitted as parity-flipped states at periodic time intervals [86]. Finally, we demonstrate how the collective interactions in a mesoscopic atomic frequency comb strongly coupled to a cavity can be used to generate a periodic pulse train of nonclassical light from a short coherent input pulse [85].

5.1. Multimode strong coupling and sustained photon pulse revivals[8]

In the following, we consider a single-mode cavity containing a strongly coupled spin ensemble with a comb-shaped spectral spin distribution. A well-known method to engineer such atomic frequency combs is the spectral hole burning of an inhomogeneously broadened ensemble [214, 215]. Recently, the possibilities of using coherent spectral hole burning by the stimulated Raman adiabatic passage [57] or the piecewise adiabatic passage technique [58] have also been discussed. Furthermore, a proposal of using intrinsic atomic levels to construct a frequency comb exists [216].

Here, we assume an arrangement of several inhomogeneously broadened spin ensembles with mean frequencies $\omega_s^{(\mu)}$ that are equidistantly spaced at intervals $\Delta\omega$, such that $\omega_s^{(\mu)} = \omega_s + \mu\Delta\omega$ for $\mu = \{-(m-1)/2, \ldots, (m+1)/2\}$ with m being the number of subensembles constituting the frequency comb as depicted in Fig. 5.1.1. While our approach is general, we will be referring in the following to one particular experimental realization based on the magnetic coupling of NV-ensembles residing in several diamonds coupled to a superconducting microwave resonator [39]. Note that by an appropriate alignment of the diamonds with respect to an external magnetic field and by exploiting the Zeeman effect, the mean frequencies of the spin ensembles, $\omega_s^{(\mu)}$, can be efficiently tuned in a rather wide spectral interval [35, 36].

We model the individual teeth of the atomic frequency comb by a q-Gaussian spectral spin distribution $\rho_\mu(\omega)$ [see Eq. (4.12)] with $q = 1.39$ and width $\gamma_{inh}/2\pi = 9.4$ MHz satisfying $\int d\omega \rho_\mu(\omega) = 1$. The collective coupling strength of each subensemble is given by $\Omega_\mu = (\sum_{k=1}^{N_\mu} g_k^{(\mu)2})^{1/2}$, where $g_k^{(\mu)}$ is the coupling strength of the k-th spin and N_μ is the number of spins. Note that the coupling strengths Ω_μ are not equal in general, but follow a Gaussian distribution $\Omega_\mu^2/\Omega^2 = \exp[-(\omega_c - \omega_s^{(\mu)})^2/2\sigma_G^2]$, with $\sigma_G/2\pi = 150$ MHz; then, Ω denotes the collective coupling strength of the central spin ensemble, and the total spectral spin distribution acquires the form

---

[8] The concept of multimode strong coupling was first introduced by Dmitry Krimer, et al. [212] for a single two-level system coupled to a multimode cavity and is adopted here for the inverse case of a single-mode cavity coupled to multiple spin modes. The text and figures in this section are partly taken from the joint publication [84]. The numerical calculations were performed by Dmitry Krimer and myself, whereas the theoretical analysis was mainly done by Dmitry Krimer and Stefan Rotter in collaboration with Stefan Putz, who helped to propose a realistic experimental realization.

$\rho(\omega) = \sum_\mu \rho_\mu(\omega)\Omega_\mu^2/\Omega^2$ depicted in Fig. 5.1.1. The spacing of the individual subensembles is given by $\Delta\omega/2\pi = 40$ MHz, which is much larger than the cavity linewidth $\kappa/2\pi = 0.4$ MHz and the spin decay rate $\gamma/2\pi = 0.01$ MHz.
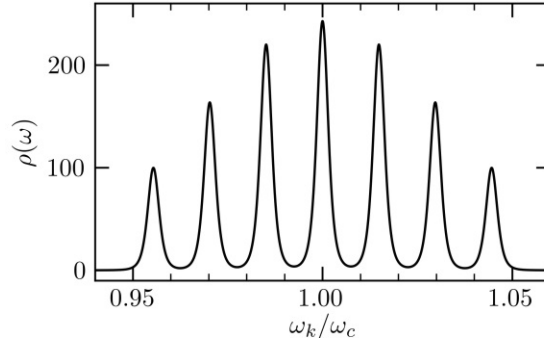
Figure 5.1.1.: Spectral spin distribution, $\rho(\omega) = \sum_\mu \Omega_\mu^2/\Omega^2 \rho_\mu(\omega)$ for $\mu = \{-(m-1)/2, \ldots, (m+1)/2\}$, of an atomic frequency comb consisting of $m = 7$ equally spaced q-Gaussians of equal widths $\gamma_{inh}/2\pi = 9.4$ MHz. The spin distribution has peaks at frequencies $\omega_s^{(\mu)} = \omega_s + \mu\Delta\omega$ with the spacing $\Delta\omega/2\pi = 40$ MHz. The cavity frequency ω_c coincides with the mean frequency of the central q-Gaussian, $\omega_s = \omega_c = 2\pi \times 2.6915$ GHz. The collective coupling strengths of the individual subensembles are distributed as $\Omega_\mu^2/\Omega^2 = \exp[-(\omega_c - \omega_s^{(\mu)})^2/2\sigma_G^2]$, with $\sigma_G/2\pi = 150$ MHz.

In the following, we consider a macroscopic spin ensemble in the weak excitation limit such that we are allowed to use the Volterra equation (2.13). Before examining the temporal evolution of the system in detail, however, we introduce the concept of multimode strong coupling [212], which gives us an insight into the transition from the dynamics of a single spin ensemble as encountered in the previous chapter to that of a more complicated atomic frequency comb.

The multimode strong coupling regime

The notion of multimode strong coupling originates from the situation where a single spin is coupled to a multimode cavity [212]. Here we translate this concept to the inverse case where multiple spins with very different frequencies are coupled to a single cavity mode. Hence, the term multimode—in the following—refers to the multiple spin ensembles with different transition frequencies $\omega_s^{(\mu)}$.

As mentioned in Section 2.1, the Volterra equation is the governing equation not only for the semiclassical case but also for the quantum case, when at $t = 0$ the system is in the state $|1, \downarrow\rangle$ with a single photon in the cavity and all spins in their ground state. Using a Laplace transformation (see Appendix F), we can write down a formal solution to the Volterra equation (2.13) for the above initial state given

by

$$A(t) = \Omega^2 \int_0^\infty e^{-i(\omega - \omega_c - i\gamma)t} \, U(\omega) \, d\omega, \tag{5.1}$$

where

$$U(\omega) = \lim_{\sigma \to 0^+} \left\{ \frac{\rho(\omega)}{(\omega - \omega_c - \Omega^2 \delta(\omega) + i(\kappa - \gamma))^2 + (\pi \Omega^2 \rho(\omega) + \sigma)^2} \right\} \tag{5.2}$$

is the kernel function and $|A(t)|^2 = \langle 1, \downarrow | a^\dagger a(t) | 1, \downarrow \rangle$ is the cavity occupation in the single-excitation regime. Furthermore,

$$\delta(\omega) = \mathcal{P} \int_0^\infty \frac{d\tilde{\omega} \rho(\tilde{\omega})}{\omega - \tilde{\omega}} \tag{5.3}$$

denotes the nonlinear Lamb shift of the cavity frequency ω_c with $\mathcal{P}$ being the Cauchy principal value. The dominant frequency components that enter the dynamics of $A(t)$ are the resonances ω_r of the kernel function $U(\omega)$. A necessary condition for such a resonance is that the first term in the denominator of $U(\omega)$ vanishes [212]

$$(\omega_r - \omega_c)/\Omega^2 = \delta(\omega_r). \tag{5.4}$$

This resonance condition allows us to identify different dynamic regimes depending on the collective coupling strength Ω.

Figure 5.1.2(a-d) depicts the kernel function $U(\omega)$ and the nonlinear Lamb shift $\delta(\omega)$ for two different coupling strengths $\Omega/2\pi = 8\,\text{MHz}$ and $26\,\text{MHz}$, respectively. The resonance condition (5.4) is fulfilled for the intersections of the nonlinear Lamb shift $\delta(\omega)$ with the straight line $(\omega - \omega_c)/\Omega^2$ [dashed line in Fig. 5.1.2(c,d)]. As the slope of $(\omega - \omega_c)/\Omega^2$ changes, so does the number of intersections, which gives rise to very different resonance structures in $U(\omega)$ and, hence, very different dynamical regimes. For $\Omega/2\pi = 8\,\text{MHz}$, we observe two pronounced resonances in the kernel function $U(\omega)$ corresponding to the well-known single-mode strong coupling regime with two polaritonic peaks. When the coupling strength is increased to $\Omega/2\pi = 26\,\text{MHz}$, the slope of $(\omega - \omega_c)/\Omega^2$ decreases, resulting in more intersection points with the nonlinear Lamb shift $\delta(\omega)$. As a consequence, we observe multiple resonances in $U(\omega)$, which leads to a new dynamic regime as detailed below.

In Fig. 5.1.2(e,f) we present the corresponding temporal evolution of the cavity photon number $\langle a^\dagger a(t) \rangle$ for the initial state $|1, \downarrow\rangle$ with a single photon inside the cavity and all spins in their ground state. For the single-mode strong coupling regime ($\Omega/2\pi = 8\,\text{MHz}$) the cavity photon number displays damped Rabi oscillations at a frequency given by the spacing of the two polaritonic peaks $U(\omega)$. Here, effectively only the central spin ensemble couples strongly to the cavity, while the presence of the off-resonant ensembles leads merely to minor distortions of the oscillations. Note that the detuning $\Delta\omega/2\pi = 40\,\text{MHz}$ of these ensembles is much larger than
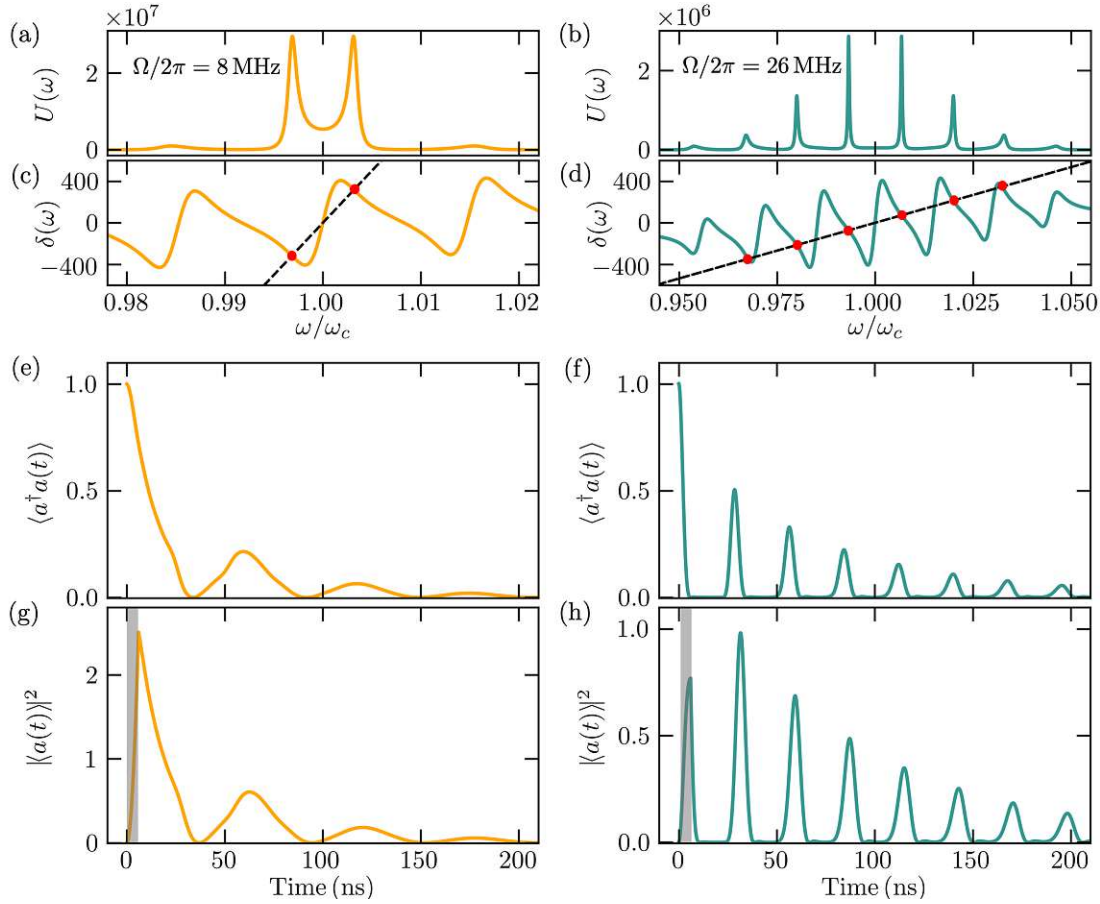
Figure 5.1.2.: Route from single-mode strong coupling to multimode strong coupling for the atomic frequency comb depicted in Fig. 5.1.1 strongly coupled to a single cavity mode. The left columns show results for a collective coupling strengths $\Omega/2\pi = 8\,\text{MHz}$ where effectively only the central spin ensemble couples to the cavity. The right columns show the same calculations for an increased coupling strength $\Omega/2\pi = 26\,\text{MHz}$ realizing multimode strong coupling. (a,b) Kernel function $U(\omega)$ of the formal solution for the cavity amplitude Eq. (5.1) showing (a) two polaritonic peaks in the single-mode strong coupling regime and (b) multiple such peaks in the multimode strong coupling regime. (c,d) Nonlinear Lamb shift $\delta(\omega)$ versus frequency ω. The red dots indicate the resonances of the kernel function $U(\omega)$ given by the intersections between $\delta(\omega)$ and the dashed line $(\omega-\omega_c)/\Omega^2$ [see Eq. (5.2)]. Note that not all intersections lead to a resonance in $U(\omega)$, since the second term of the denominator in Eq.(5.2) can suppress such a contribution. (e,f) Dynamics of the cavity photon number $\langle a^\dagger a(t) \rangle$ when at $t = 0$ the cavity is in the single photon state $|1, \downarrow\rangle$, with all spins unexcited. The dynamics is governed by the frequencies of the Kernel function $U(\omega)$ featuring (e) damped Rabi-oscillations in the single-mode strong coupling regime and (f) pulsed revivals of the initial excitation in the multimode strong coupling regime. (g,h) Semiclassical evolution of the cavity probability amplitude $|\langle a(t) \rangle|^2$ after a short coherent input pulse of rectangular shape and $6\,\text{ns}$ duration showing the same characteristic behavior as (e,f).

the cavity linewidth $\kappa/2\pi = 0.4\,\text{MHz}$ and the coupling strength $\Omega/2\pi = 8\,\text{MHz}$. However, with the increased coupling strength $\Omega/2\pi = 26\,\text{MHz}$ all subensembles start to couple to the cavity as outlined above, with the system entering the multimode strong coupling regime. Instead of Rabi oscillations, here, we observe pulsed revivals of the initial excitation, which can be attributed to a constructive rephasing of the spins at time intervals that are approximately equal to the inverse of the spectral distance $2\pi/\Delta\omega$ between adjacent subensembles.

We find very similar dynamics in the semiclassical case presented in Fig. 5.1.2(g,h) when we directly solve the Volterra equation (2.13) for a short rectangular input pulse on resonance with the cavity $\omega_p = \omega_c$. The duration of the driving pulse is chosen to be $6\,\text{ns}$, which is much smaller than the intrinsic dephasing time in our system such that the inhomogeneous broadening has only negligible influence during the excitation pulse and the dynamics resembles the evolution in the single-excitation regime. As before, the cavity amplitude $|\langle a(t)\rangle|^2$ shows distorted Rabi oscillations for $\Omega/2\pi = 8\,\text{MHz}$ and periodic pulses of excitation for $\Omega/2\pi = 26\,\text{MHz}$. While these results already demonstrate that one can enter a new dynamic regime of pulsed emission from collectively coupled and inhomogeneously broadened spin ensembles for realistic parameter values, the number of pulses that we observe in Fig. 5.1.2 is rather limited. As we show below, one can resolve this limitation in the system by the method of spectral hole burning [55].

Eigenvalue analysis

To arrive at these results, we first need to investigate the eigenvalues and the corresponding eigenstates of the strongly coupled cavity-spin system. For this purpose we start from the discrete set of linear differential equations for the cavity and spin expectation values [Eqs. (2.3a) and (2.3b)] and substitute $\langle a(t)\rangle = A \cdot \exp(-\lambda t)$ as well as $\langle \sigma_k(t)\rangle = B_k \cdot \exp(-\lambda t)$. This allows us to derive the non-Hermitian eigenvalue problem

$$\mathcal{L}\psi_l = \lambda_l \psi_l, \tag{5.5}$$

with

$$\mathcal{L} = \begin{pmatrix} \kappa & -g_1 & -g_2 & ... & -g_N \\ g_1 & \gamma + i(\omega_1 - \omega_c) & 0 & ... & 0 \\ g_2 & 0 & \gamma + i(\omega_2 - \omega_c) & ... & 0 \\ ... & ... & ... & ... & ... \\ g_N & 0 & 0 & ... & \gamma + i(\omega_N - \omega_c) \end{pmatrix}, \tag{5.6}$$

and $\psi_l = (A_l, B_l^k)^T$, which we solve numerically for different values of the mean spin frequency ω_s. Note that $\text{Im}(\lambda_l)$ plays the role of the collective eigenfrequency and $\text{Re}(\lambda_l) > 0$ is the decay rate of ψ_l. When solving this eigenvalue problem, we always keep the same shape for the spectral function $\rho(\omega)$ depicted in Fig. 5.1.1
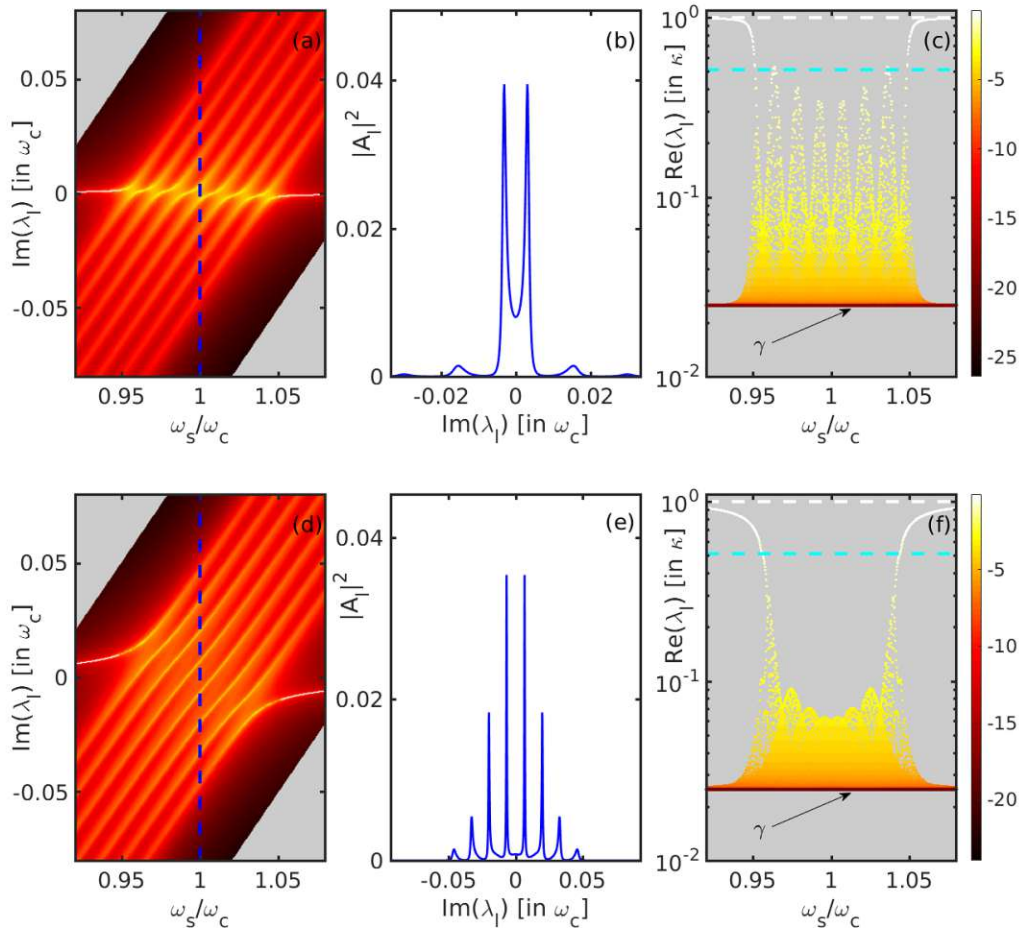
Figure 5.1.3.: (a-c) Single-mode strong coupling regime. Solution of the eigenvalue problem [Eq. (5.5)] for $\Omega/2\pi = 8$ MHz as a function of the mean spin frequency ω_s of the spectral function $\rho(\omega)$ shown in Fig. 5.1.1. (a) Cavity content $|A_l|^2$ of the normalised eigenvector $\psi_l = (A_l, B_l^k)$ versus eigenfrequencies $\mathrm{Im}(\lambda_l)$ and ω_s (logarithmic color scale): two prominent polariton modes are clearly distinguishable from a bath of dark states with low cavity content at fixed values of ω_s. (b) The cavity content $|A_l|^2$ versus $\mathrm{Im}(\lambda_l)$ for the resonant case $\omega_s = \omega_c$ along the vertical cut shown in (a) (dashed blue line). (c) $|A_l|^2$ versus decay rates $\mathrm{Re}(\lambda_l)$ and ω_s with the same coloring as in (a). The cyan dashed line indicates the minimal decay rate of the cavity amplitude reachable by the cavity protection effect given by $\kappa/2$, with $\kappa = 2\pi \times 0.4$ MHz (HWHM of the cavity decay) and $\gamma = 2\pi \times 0.01$ MHz $\ll \kappa$ (HWHM of the spin decay). The white dashed line indicates the decay rate of the bare cavity mode κ. (d-f) Multimode strong coupling regime. Solution to the same eigenvalue problem as above but for an increased coupling strength $\Omega/2\pi = 26$ MHz (same color-coding and notations as above). Eight polariton modes are clearly visible with an almost equidistant spacing, see (e) for the resonant case $\omega_s = \omega_c$. In all calculations $N = 1200$ spins were used.

but shift the whole structure in the frequency domain by detuning the mean spin frequency ω_s of the central ensemble with respect to the cavity frequency ω_c.

The results of these calculations are presented in Fig. 5.1.3 for $\Omega/2\pi = 8\,\mathrm{MHz}$ and $\Omega/2\pi = 26\,\mathrm{MHz}$, where we plot the cavity content $|A_l|^2$ of the normalized eigenvector ψ_l as a function of ω_s and $\mathrm{Im}(\lambda_l)$ (a,d) or $\mathrm{Re}(\lambda_l)$ (c,f), respectively. For $\Omega/2\pi = 8\,\mathrm{MHz}$ each subensemble separately is in the strong coupling regime and we observe an avoided crossing in Fig. 5.1.3(a) whenever the resonance condition $\omega_s^{(\mu)} = \omega_c$ is satisfied. The off-resonant spin ensembles, however, provide only a negligible cavity content [see Fig. 5.1.3(b)]. It can be seen from Fig. 5.1.3(c) that a large fraction of eigenstates, ψ_l , decays with some intermediate decay rate which lies within the interval $\gamma < \mathrm{Re}(\lambda_l) < \kappa$. With a further increase of the coupling strengths to $\Omega/2\pi = 26\,\mathrm{MHz}$ the avoided crossings are replaced by a comb-shaped structure with parallel stripes of large cavity content $|A_l|^2$ [yellow lines in Fig. 5.1.3(d)] indicating the multimode strong coupling between all subensembles and the cavity. It is worth noting that the peaks become substantially sharper as compared to the case of the single-mode strong coupling regime [compare Fig. 5.1.3(e) and (b)], which can be attributed to the so called "cavity protection effect" [37, 38, 53, 54]. This phenomenon can also be observed in Fig. 5.1.3(f) where the decay rates are shifted towards smaller values compared those in Fig. 5.1.3(c).

Sustained photon pulse revivals

In the following, we want to apply these findings to suppress the decay of the observed revivals in the multimode strong coupling regime. For this purpose, we make use of the recent insight [55] that the decoherence induced by the spin broadening can be strongly suppressed by burning two narrow spectral holes in the spin spectral density close to the maxima of the two polaritonic peaks. This effect is based on the creation of long-lived collective dark states [53, 54, 56, 211] in the spin ensemble that have only very little cavity content. Here, we generalize this theoretical concept, which meanwhile has also been successfully implemented experimentally [56], to the multimode strong coupling regime.

The most natural extension of this hole-burning approach to the multimode regime would demand that the positions of the burned spectral holes remain close to the polaritonic peaks of which we observe altogether eight in Fig. 5.1.3(e). As illustrated in Fig.5.1.4, we therefore burn eight narrow spectral holes into the spin distribution $\rho(\omega)$ at frequencies which correspond to the maxima of the cavity content, $|A_l|^2$, shown in Fig. 5.1.3(e). The hole burning can be straightforwardly implemented in an experiment by exposing the cavity to very high intensity pulses that feature frequency components exactly at the position of the desired holes. The spins at these frequencies will then saturate and no longer couple to the cavity such that they are effectively removed from the spin distribution. While the hole burning itself is a nonlinear process which can not be modeled by the Volterra equation,
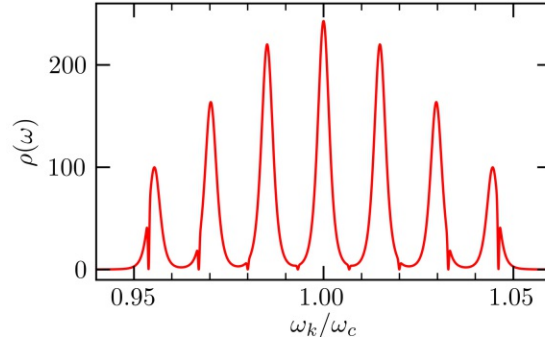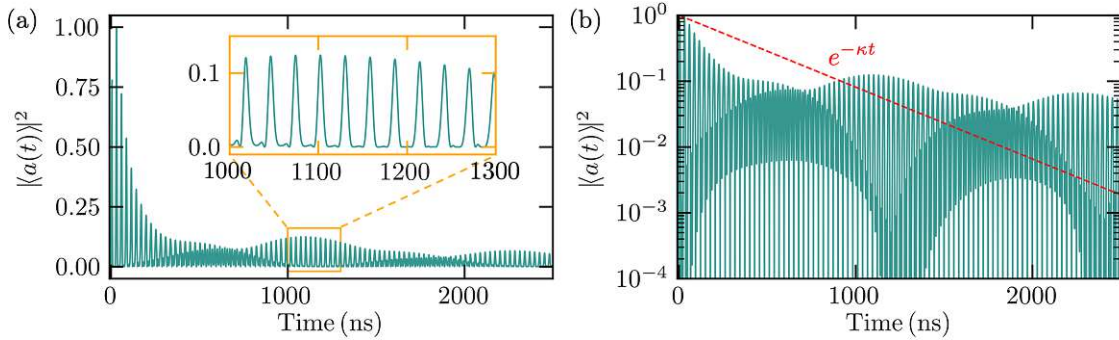
Figure 5.1.4.: Spectral spin distribution from Fig. 5.1.1 with eight spectral holes (red) at the maxima of the cavity content $|A_l|^2$ shown in Fig. 5.1.3(e) for $\Omega/2\pi = 26$ MHz. All holes are of equal width, $\Delta_h/2\pi = 0.47$ MHz, and are modeled by a Gaussian lineshape.

the subsequent dynamics can be well described using the same formalism as above. We therefore assume that the holes are burned at $t = 0$ and numerically integrate the Volterra equation for the spin distribution depicted in Fig.5.1.4 after a short rectangular input pulse.

Figure 5.1.5 shows that the pulsed revivals of the cavity probability amplitude $|\langle a(t) \rangle|^2$ persist over a drastically increased time interval as compared to the corresponding case without hole burning presented in Fig.5.1.2(h). Notably, the suppression of decoherence surpasses also the limit imposed by the cavity protection effect as illustrated in Fig.5.1.5(b). Note that while the decay of the bare cavity

Figure 5.1.5.: Cavity probability amplitude $|\langle a(t) \rangle|^2$ as a function of time t under the action of a short (6 ns) rectangular input pulse for a comb-shaped spin distribution with eight spectral holes as presented in Fig. 5.1.4. All other parameters are the same as for the case without hole burning presented in Fig. 5.1.2(d). (b) Same as (a) but with the ordinate plotted on a logarithmic scale. The decay process with the minimal decay rate reachable by the cavity protection effect, $e^{-\kappa t}$, with $\kappa/2\pi = 0.4$ MHz is depicted by the red dashed line. Note that the rate of $|\langle a(t) \rangle|^2$ for a bare cavity without spin ensemble is given by $e^{-2\kappa t}$ (not shown).

probability is given by $e^{-2\kappa t}$, the cavity protection effect in the limit of $\gamma \ll \kappa$ predicts a decay following $e^{-\kappa t}$ [38]. We find that the photon pulse revivals significantly exceed this barrier such that, e.g., at $t = 3\,\mu$s after the driving pulse, the values of $|\langle a(t) \rangle|^2$ are two orders of magnitude above those achievable through the cavity protection effect. To check if the holes we burned in the ensemble are, indeed, located at the optimal positions, we also performed additional calculations (not shown) in which we varied the hole positions by only a few percent away from the maxima of $|A_l|^2$. This leads to a substantial decrease in the revival amplitudes as compared to those in Fig.5.1.5 confirming our initial choice of positioning the holes right at the frequencies of the polaritonic peaks to obtain long-lived photon pulse revivals.

5.2. Cavity state revivals[9]

As we have shown in the previous section, the strong coupling of a cavity to multiple spin ensembles, which form an atomic frequency comb, leads to pulsed revivals of the initial cavity occupation probability. While the Volterra integral formalism used in this context is also valid in the single-photon regime, it does not provide access to the quantum mechanical phase space of the spin-cavity system. In this section, we use a time-dependent variational renormalization group method (Section 3.2) to shed light on the quantum mechanical wavefunction of the cavity field during the periodic absorption and re-emission process of the atomic frequency comb. This is particularly interesting since the infinite Hilbert space of the cavity can encode quantum information in various forms ranging from simple Fock states [217] to error-correcting Schrödinger cat codes [218–221], binomial codes [222, 223], or Gottesman-Kitaev-Preskill codes [224, 225], which promise fault-tolerant bosonic quantum computing.

Unlike in the previous section, we study here a mesoscopic spin ensemble of $N = 70$ spins without inhomogeneous broadening. The frequency comb is given by $m = 7$ frequency clusters $\omega_\mu = \omega_c + \mu \Delta\omega$ with $\mu = \{-(m-1)/2, ..., (m-1)/2\}$, where each subensemble is filled with $N' = N/m$ spins. As before, the collective coupling strength of the μ-th sub-ensemble is then given by $\Omega_\mu = \sum_k^{N'} g_{\mu,k}^2 = N' g_\mu^2$. While our treatment is very general, we use in our calculations parameters in the microwave regime that are realistic in experiments with nitrogen-vacancy centers in diamond assuming $\omega_c/2\pi = 3$ GHz and $\Delta\omega/2\pi = 40$ MHz. If not stated otherwise we use the parameters $\kappa/2\pi = 0.2$ MHz, $\gamma_h/2\pi = 1$ kHz, and $\gamma_p/2\pi = 33$ kHz.

---

[9] The results presented in this section are based on the publication [86], from which also figures and parts of the text are taken. All calculations were performed by myself under the supervision of Dmitry Krimer and Stefan Rotter. Himadri Dhar helped with the theoretical interpretation of our results and developed the time-dependent variational renormalization group method used in this section.
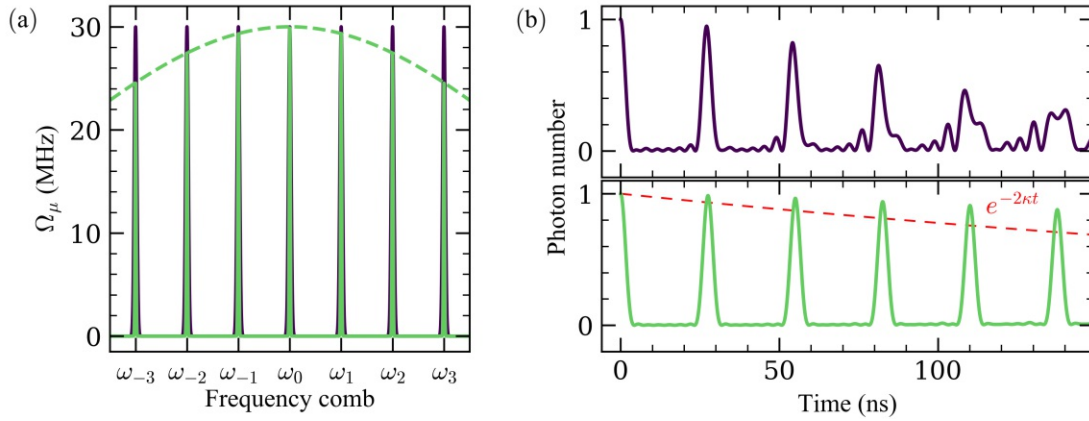
Figure 5.2.1.: (a) Comb-shaped distribution of the collective coupling strengths Ω_μ (without inhomogeneous broadening). Here we compare a uniform comb structure, where each frequency cluster (indicated by a delta-like peak) couples to the cavity with the same coupling strength $\Omega_\mu/2\pi = 30$ MHz (purple), with a spectrally engineered comb structure (light green), where Ω_μ follows a Gaussian envelope (dashed line) $\Omega_\mu = \Omega_0 \exp\left[-(\omega_c - \omega_\mu)^2/2\lambda^2\right]$, with $\Omega_0/2\pi = 30$ MHz and $\lambda/2\pi = 0.19$ GHz. (b) Cavity photon number $\langle a^\dagger a \rangle$ as a function of time for the modified (bottom) and uniform (top) comb structure. The spin ensemble in both cases is initially unexcited and the cavity is prepared in a coherent state $|\alpha\rangle$ of amplitude $\alpha = 1$. The red dashed line corresponds to the bare cavity decay proportional to $\exp(-2\kappa t)$, with $2\kappa = 2\pi \times 0.4$ MHz.

In the following, we assume that the spin ensemble is initially unexcited and the cavity is prepared in some initial state $|\psi_{\rm cav}^{\rm in}\rangle$. Before we examine the quantum evolution of the cavity wave function for specific multi-photon states, we revisit the revival dynamics of the cavity photon number $\langle a^\dagger a(t) \rangle$ with the cavity being initially in the coherent state $|\psi_{\rm cav}^{\rm in}\rangle = |\alpha\rangle$ with amplitude $\alpha = 1$. For the simplest case of a uniform coupling distribution, where each subensemble couples with the same strength $\Omega_\mu/2\pi = 30$ MHz [depicted in Fig. 5.2.1(a)], we observe in Fig. 5.2.1(b) that the cavity excitation is first transferred into the frequency comb and then re-emitted back into the cavity at a well-defined later time $T_{\rm rev}$. As we have encountered in the previous section, this process repeats periodically, leading to a series of revivals in the cavity photon number. We note that for the uniform coupling distribution, however, the photon numbers drop already significantly during the first five revivals depicted in Fig. 5.2.1(b) (top panel). Interestingly, this drastic decrease is not a result of losses in the cavity or the spin ensemble but rather a consequence of the normal-mode splitting in the strong coupling regime, which distorts the comb's equidistant frequency spectrum. As detailed below, this frequency detuning can be compensated through a customized engineering of the spectral coupling distribution Ω_μ. Using a Gaussian distribution of standard deviation $\lambda/2\pi = 0.19$ GHz for the coupling strengths Ω_μ, we obtain a long-lived train of revivals in the cavity photon

number as presented in Fig. 5.2.1(b) (bottom panel). A comparison with the bare cavity decay $\propto \exp(-2\kappa t)$ shows that the excitation transfer to the long-lived spin ensemble protects the initial excitation from the cavity losses.

Revivals of multi-photon cavity states

The important open question we now address is, which quantum states are written into the cavity by the frequency comb during the revivals and how these states are related to the initial cavity wave function. To answer this question comprehensively, we examine the quantum mechanical evolution of the cavity wave function during the periodic absorption and re-emission process for three different initial states $|\psi_{\mathrm{cav}}^{\mathrm{in}}\rangle$: (i) $|\alpha\rangle$ is a coherent state of amplitude $\alpha = \sqrt{2}$, which closely resembles the situation of a short coherent pulse injected into the cavity. (ii) $|\psi_{\mathrm{sup}}\rangle = \frac{1}{\mathcal{N}_{\mathrm{sup}}} \sum_{n=1}^{4} c_n |n\rangle$ is a superposition of the four lowest Fock states $|n\rangle$ with the coefficients c_{1-4} chosen arbitrarily as 5, $-i\sqrt{15}$, $-(\sqrt{10} - i\sqrt{15})$, and $(5 - i\sqrt{10})$ such that no apparent phase relation can be established between neighboring Fock states. (iii) $|\psi\rangle_{\mathrm{cat}} = \frac{1}{\mathcal{N}_{\mathrm{cat}}}(|\beta\rangle + |-\beta\rangle)$ with $\beta = 2$ denotes a Schrödinger cat state as used in many quantum information processing tasks, including quantum computation [226], quantum teleportation [227], and precision measurements [228].
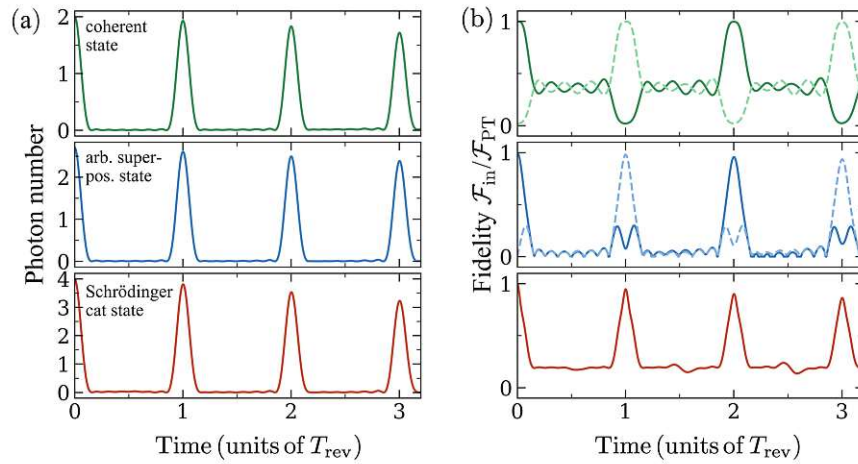
Figure 5.2.2.: (a) Cavity photon number $\langle a^\dagger a \rangle$ as a function of time for three different initial states $|\psi_{\mathrm{cav}}^{\mathrm{in}}\rangle$ of the cavity: (i) $|\alpha\rangle$, (ii) $|\psi_{\mathrm{sup}}\rangle$, and (iii) $|\psi_{\mathrm{cat}}\rangle$ (top to bottom) as specified in the main text. (b) Fidelity of the time evolved cavity state $\rho_{\mathrm{cav}}(t)$ with its initial state from (a) $|\psi_{\mathrm{cav}}^{\mathrm{in}}\rangle$ ($\mathcal{F}_{\mathrm{in}}$, solid line) and with the parity transformed state $\hat{\Pi}|\psi_{\mathrm{cav}}^{\mathrm{in}}\rangle$ ($\mathcal{F}_{\mathrm{PT}}$, dashed line). Here, the coupling distribution Ω_μ for all three cases follows the same Gaussian envelope with $\lambda/2\pi = 0.19$ GHz.
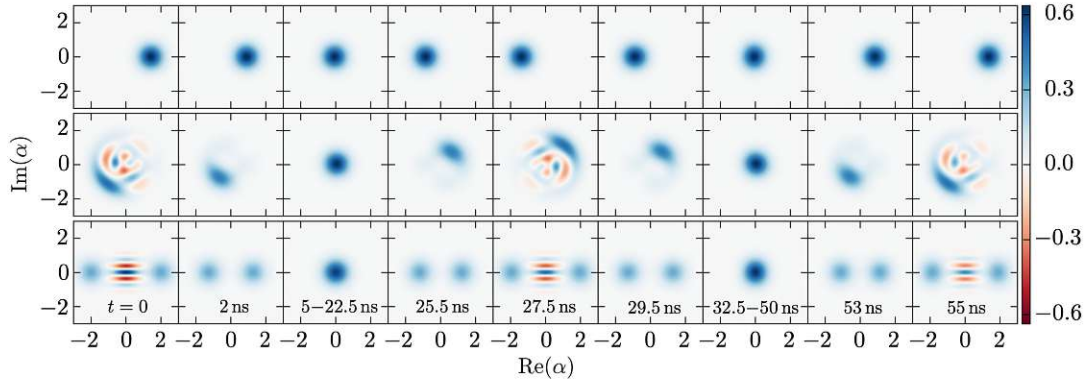
Figure 5.2.3.: Wigner functions corresponding to the dynamics presented in Fig. 5.2.2 (timestamps are given in the bottom row). The cavity state is transferred to the spin ensemble within a few nanoseconds. Then the cavity remains empty until the stored photons are re-emitted at $T_{\mathrm{rev}} = 27.5\,\mathrm{ns}$. Note that after one absorption and re-emission period, the Wigner function is point-reflected through the origin, which amounts to a parity transformation $\hat{\Pi} = \exp(i\pi\hat{a}^\dagger\hat{a})$ of the initial state. Initial states which are not eigenstates of the parity operator $\hat{\Pi}$, such as $|\alpha\rangle$ or $|\psi_{\mathrm{sup}}\rangle$, are therefore restored only after $2\,T_{\mathrm{rev}} = 55\,\mathrm{ns}$.

First of all, we see in Fig. 5.2.2(a) that for all three initial states the cavity photon number $\langle\hat{a}^\dagger\hat{a}\rangle$ shows the characteristic periodic revival structure: The initial cavity photons are absorbed by the spin ensemble within a few nanoseconds, irrespective of the quantum state in which the cavity is initialized. After that, the cavity remains empty until the number of photons is restored at $t = T_{\mathrm{rev}} \approx 27.5$ ns and the process starts all over again. Since we have direct access to the full density matrix of the cavity field, we are now in the position to calculate the fidelity

$$\mathcal{F}_{\mathrm{in}} = \mathcal{F}\{\rho_{\mathrm{cav}}(t), \rho_{\mathrm{in}}\} = \left(\mathrm{Tr}\left[\sqrt{\sqrt{\rho_{\mathrm{cav}}(t)}\rho_{\mathrm{in}}\sqrt{\rho_{\mathrm{cav}}(t)}}\right]\right)^2 \qquad (5.7)$$

of the cavity state $\rho_{\mathrm{cav}}(t)$ with the initial state $\rho_{\mathrm{in}} = |\psi_{\mathrm{cav}}^{\mathrm{in}}\rangle\langle\psi_{\mathrm{cav}}^{\mathrm{in}}|$ during the absorption and revival process. Figure 5.2.2(b) shows that $\mathcal{F}_{\mathrm{in}}$ has a maximum peak of almost one for the Schrödinger cat state (iii) at the first revival but at the same time is minimal for the coherent (i) and the chosen superposition state (ii). As we show below, the reason for this peculiar behavior is that the absorption and re-emission by the frequency comb act as a parity transformation $\hat{\Pi} = \exp(i\pi\hat{a}^\dagger\hat{a})$ on the initial state. We therefore calculate the fidelity $\mathcal{F}_{\mathrm{PT}} = \mathcal{F}\{\rho_{\mathrm{cav}}(t), \rho_{\mathrm{PT}}\}$ of $\rho_{\mathrm{cav}}(t)$ with the parity-transformed initial state $\rho_{\mathrm{PT}} = \hat{\Pi}\rho_{\mathrm{in}}\hat{\Pi}^\dagger$ and present the results in Fig. 5.2.2(b) as well. Our calculations confirm that the state that is restored in the cavity at the first revival is indeed the parity-transformed initial state. Note that the Schrödinger cat state is an eigenstate of the parity operator such that

$\mathcal{F}_{\mathrm{PT}} = \mathcal{F}_{\mathrm{in}}$.

Using the access to the full density matrix of the cavity, we plot in Fig. 5.2.3(b) the Wigner function

$$W(\alpha, \alpha^*, t) = \frac{1}{\pi^2} \int d^2\beta\, e^{\alpha\beta^* - \alpha^*\beta} \operatorname{Tr}\{e^{\beta\hat{a}^\dagger - \beta^*\hat{a}} \rho_{\mathrm{cav}}(t)\} \tag{5.8}$$

of the cavity field during the periodic revivals. As expected, the cavity state is absorbed by the spin ensemble within a few nanoseconds regardless of the initial state. The cavity remains in the vacuum state $|0\rangle$ for times $t = 5\,\mathrm{ns}$ to $22.5\,\mathrm{ns}$ before the multi-photon state is finally re-emitted from the spin ensemble. We see that at the peak of the first revival at $T_{\mathrm{rev}} = 27.5\,\mathrm{ns}$ the Wigner function is point-reflected through the origin as compared to the initial Wigner function, which corresponds to a parity transformation as discussed above. Then the process starts all over again such that the initial cavity state is restored at $2\,T_{\mathrm{rev}}$.

The energy spectrum in the few-excitation limit

As demonstrated in Fig. 5.2.1, a uniform coupling distribution leads to a rapid decrease in the photon number of the revivals, which can be attributed to an imperfect rephasing of the atomic frequency comb. To examine this in more detail, we calculate the eigenenergies of the compound spin-cavity system in the one- and two-excitation subspace. Introducing collective spin operators for each subensemble of the frequency comb $J_\mu^z = \frac{1}{2}\sum_{k=1}^{N'}\sigma_k^z$ and $J_\mu^\pm = \sum_{k=1}^{N'}\sigma_k^\pm$, the Tavis-Hamiltonian can be rewritten as

$$H = \omega_c a^\dagger a + \sum_\mu \omega_\mu J_\mu^z + g_\mu \sum_\mu (J_\mu^+ a + J_\mu^- a^\dagger). \tag{5.9}$$

With the use of a collective spin basis [98]

$$J_\mu^z |J_\mu, m_\mu\rangle = m_\mu |J_\mu, m_\mu\rangle = (-N'/2 + q_\mu)|q_\mu\rangle, \tag{5.10}$$

and

$$\begin{aligned} J_\mu^\pm |J_\mu, m_\mu\rangle &= \sqrt{J_\mu(J_\mu + 1) - m_\mu(m_\mu \pm 1)}\,|J_\mu, m_\mu\rangle \\ &= \sqrt{N'/2 + N'q_\mu - q_\mu^2 \pm (N'/2 - q_\mu)}\,|q_\mu\rangle, \end{aligned} \tag{5.11}$$

we can set up the one- and two-excitation subspace for the coupled spin-cavity system. Note that we have introduced the shorthand notation $|J_\mu, m_\mu\rangle = |q_\mu\rangle$ for the spin states, where q_μ denotes the number of excitations in the μ-th subensemble. We write the $1 + m$ basis states of the one-excitation subspace of the combined spin-cavity system as $|1_c\rangle|0_\mu\rangle$ and $|0_c\rangle|1_\mu\rangle$. Here, $|1_c\rangle|0_\mu\rangle$ denotes a state with a

single excitation in the cavity part and no excitation in the spin ensemble, whereas $|0_c\rangle |1_\mu\rangle$ denotes m states where the single excitation is in the μ-th subensemble (with all other subensembles unexcited) and no excitation in the cavity. The action of the Hamiltonian (5.9) on this one-excitation basis is then given by

$$H |1_c\rangle |0_\mu\rangle = \left(\omega_c - \frac{N'}{2}\omega_\Sigma \right) |1_c\rangle |0_\mu\rangle + \sum_\mu \Omega_\mu |0_c\rangle |1_\mu\rangle , \qquad (5.12)$$

$$H |0_c\rangle |1_\mu\rangle = \left(\omega_\mu - \frac{N'}{2}\omega_\Sigma \right) |0_c\rangle |1_\mu\rangle + \Omega_\mu |1_c\rangle |0_\mu\rangle , \qquad (5.13)$$

with $\omega_\Sigma = \sum_\mu \omega_\mu$.

Using the same notation as above, the basis states of the two-excitation subspace can be written as $|2_c\rangle |0_\mu\rangle$, $|1_c\rangle |1_\mu\rangle$, $|0_c\rangle |1_\mu\rangle |1_\nu\rangle$, $|0_c\rangle |2_\mu\rangle$ (in total $1 + m + m (m - 1)/2 + m$ basis states). The Hamiltonian (5.9) acting on these states gives

$$H |2_c\rangle |0_\mu\rangle = \left(2\omega_c - \frac{N'}{2}\omega_\Sigma \right) |2_c\rangle |0_\mu\rangle + \sqrt{2} \sum_\mu \Omega_\mu |1_c\rangle |1_\mu\rangle , \qquad (5.14)$$

$$H |1_c\rangle |1_\mu\rangle = \left(\omega_c + \omega_\mu - \frac{N'}{2}\omega_\Sigma \right) |1_c\rangle |1_\mu\rangle + \Omega_\mu \sqrt{2} |2_c\rangle |0_\mu\rangle + \sum_{\nu \neq \mu} \Omega_\nu |0_c\rangle |1_\mu\rangle |1_\nu\rangle$$

$$+ \Omega_\mu \sqrt{2 - 2/N'} |0_c\rangle |2_\mu\rangle , \qquad (5.15)$$

$$H |0_c\rangle |1_\mu\rangle |1_\nu\rangle = \left(\omega_\mu + \omega_\nu - \frac{N'}{2}\omega_\Sigma \right) |0_c\rangle |1_\mu\rangle |1_\nu\rangle + \Omega_\mu |1_c\rangle |1_\nu\rangle + \Omega_\nu |1_c\rangle |1_\mu\rangle ,$$

$$(5.16)$$

and

$$H |0_c\rangle |2_\mu\rangle = \left(2\omega_\mu - \frac{N'}{2}\omega_\Sigma \right) |0_c\rangle |2_\mu\rangle + \Omega_\mu \sqrt{2 - 2/N'} |1_c\rangle |1_\mu\rangle . \qquad (5.17)$$

With the above equations one can set up the Tavis-Cummings Hamiltonian in the single- and two-excitation basis and obtain its eigenvalues numerically. The resulting energy spectrum is presented in Fig. 5.2.4 as a function of the coupling strength Ω_μ for the simple case of an equidistant frequency comb with $\Delta\omega/2\pi = 40$ MHz and uniform coupling. The strong coupling leads to a normal-mode splitting, which lifts the degeneracy of the cavity mode and the central (resonant) spins. Consequently, the first rung of the energy ladder in the strong coupling regime consists of $m+1$ levels instead of m in the uncoupled case. The coupling between the cavity and spin ensemble thereby shifts the energy levels of the spin-cavity system such that they are no longer equidistant. This deviation from an equidistant energy spectrum leads to an imperfect rephasing of the spin ensemble and thereby to a deterioration of the observed revivals. In the following we show how a modification of the distribution of collective coupling strengths Ω_μ can compensate the coupling induced energy shifts and restore revivals of high fidelity.
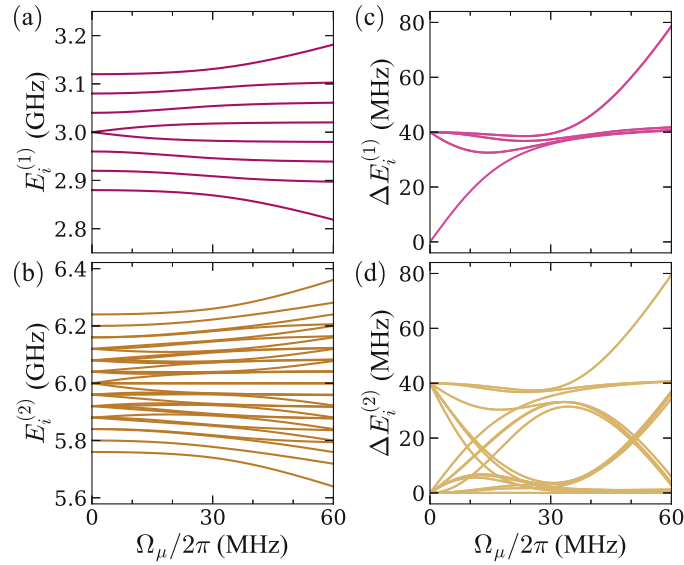
Figure 5.2.4.: (a,b) Energy spectrum of the one- and two-excitation subspace of the Tavis-Cummings Hamiltonian (5.9) as a function of the collective coupling strength Ω_μ. Here we consider the simplest case of an equidistant atomic frequency comb structure with $\Delta\omega/2\pi = 40$ MHz uniformly coupled to a single cavity mode. (c,d) Corresponding spacings $\Delta E_i^{(1/2)}$ of neighboring energy levels. The spin-cavity coupling lifts the equidistant energy spectrum of the atomic frequency comb yielding a non-equidistant spectrum for the compound spin-cavity system.

Spectral engineering

To compensate for the energy distortions in the strong coupling regime, we modify the distribution of coupling strengths as indicated in Fig. 5.2.1 by a Gaussian envelope $\Omega_\mu = \Omega_0 \exp\left[-(\omega_c - \omega_\mu)^2/2\lambda^2\right]$. In principle, we could optimize each coupling strength individually to find the distribution that optimally restores an equidistant energy spectrum. However, the choice of a fixed distribution function has the appealing advantage that we can monitor the fidelity of the revivals and the energy spacings as a function of a single parameter, i.e., the standard deviation λ of the Gaussian envelope.

Subsequently, we tune the standard deviation of the coupling distribution between the values $\lambda/2\pi = 1$ GHz and $\lambda/2\pi = 0.1$ GHz as depicted in Fig. 5.2.5(a) for specific values of λ. We calculate the corresponding dynamics for the simple initial state $|\psi_{\text{cav}}^{\text{in}}\rangle = \frac{1}{\sqrt{2}}(|1\rangle + |2\rangle)$ and evaluate the fidelity $\mathcal{F}_{\text{in/PT}}$ at the first four revivals. Hereafter we will drop the subscripts in $\mathcal{F}_{\text{in/PT}}$ implying that we use the former at even revivals and the latter at odd revivals of the cavity state. To exclude effects stemming from the openness of the system, all loss parameters are set to zero such that deviations from $\mathcal{F} = 1$ can be attributed exclusively to an imperfect rephasing of the frequency comb. Figure 5.2.5(b) shows the fidelity $\mathcal{F}$ at the first

four revivals for the same selection of coupling distributions as presented in (a). For $\lambda/2\pi = 1$ GHz, which corresponds to an almost uniform coupling, the fidelity stays noticeably below one with $\mathcal{F} = 98.1\%$ at the first revival and continues to deteriorate rapidly reaching values ranging from 92.6% to 71.7% for the following three revivals. The fidelity of the revivals drastically increases for decreasing values of λ reaching a maximum for $\lambda/2\pi \approx 0.19$ GHz; here the fidelity with the initial state is 98.6% even for the fourth revival. For λ decreasing even further, the fidelity of the revivals deteriorates again.
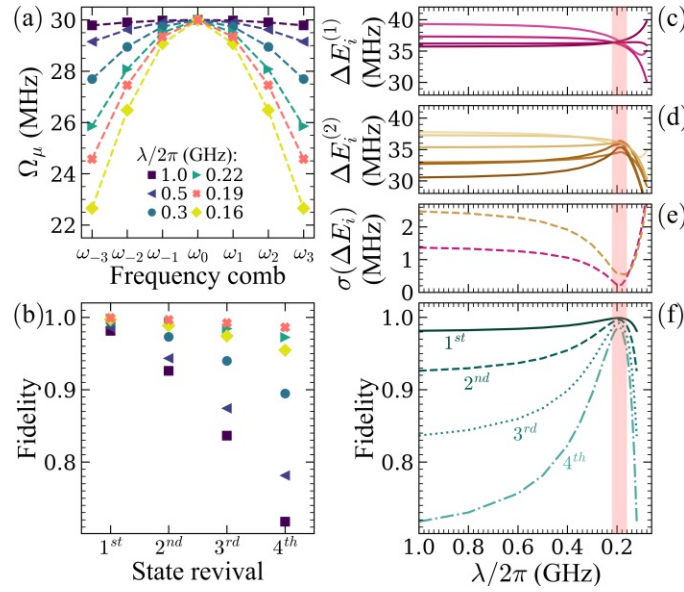
Figure 5.2.5.: (a) Distribution of collective coupling strengths Ω_μ of each frequency cluster of the atomic frequency comb with $\omega_\mu = \omega_c + \mu\Delta\omega$ for $\mu = \{-3, -2, ..., 3\}$ and with $\Delta\omega/2\pi = 40$ MHz. The couplings follow Gaussian distributions with standard deviations $\lambda/2\pi$ ranging from 1 GHz to 0.16 GHz. (b) Fidelity at the first four cavity state revivals for the coupling distributions presented above. At even revivals the fidelity is calculated for the cavity state function and the initial state $|\psi_{\mathrm{cav}}^{\mathrm{in}}\rangle = \frac{1}{\sqrt{2}}(|1\rangle + |2\rangle)$; at odd revivals we calculate the fidelity of the cavity state function and the parity transformed initial state. (c,d) Energy spacings $\Delta E_i^{(1/2)}$ of the one- and two-excitation subspace of the Tavis-Cummings Hamiltonian as a function of the distribution parameter λ. In the vicinity of $\lambda/2\pi = 0.19$ GHz (red shaded areas) the energy levels become almost equidistant resulting in an enhanced performance of the atomic frequency comb. (e) Standard deviation of $\Delta E_i^{(1/2)}$ (purple/yellow) as a function of λ. (f) Fidelity at the first four cavity state revivals as a function of λ showing distinct maxima around $\lambda/2\pi = 0.19$ GHz.

Next, we present in Fig. 5.2.5(c,d) the energy level spacings $\Delta E_i^{(1)}$, $\Delta E_i^{(2)}$ of the one- and two-excitation subspace of the Tavis-Cummings Hamiltonian, Eq. (5.9), as a function of the width λ of the Gaussian coupling distribution. The energy

shifts induced by the normal-mode splitting are larger for the energy levels close to resonance with the cavity than for off-resonant levels. The energy levels of a uniformly coupled spin-cavity system are therefore no longer equidistant, which inhibits a perfect rephasing of the initial cavity state as discussed above. Conversely, the Gaussian modification of the coupling distribution acts as a compensation for the induced energy shifts, as evidenced in Fig. 5.2.5(e). Here, we present the standard deviation $\sigma(\Delta E_i^{(1/2)})$ of the energy spacings $\Delta E_i^{(1/2)}$ showing a minimum at $\lambda = 0.19$ GHz, which is the same parameter value for which the fidelity depicted in Fig. 5.2.5(f) shows a maximum. Our findings thus confirm that in the regime of strong coupling, the spectral engineering of the spin ensemble is a viable tool to efficiently preserve the quantum information in the system.

Note further that the mean energy spacing of the energy levels in the few-excitation subspace is given by $\overline{\Delta E_i^{(1)}} \approx 36.36$ MHz (at $\lambda/2\pi = 0.19$ GHz). This leads to a revival time of $T_{\mathrm{rev}} = 1/\overline{\Delta E_i^{(1)}} = 27.5$ ns, which is in excellent agreement with the value observed our calculations.

5.3. Periodic pulses of nonclassical light[10]

Whereas in the previous section, we showed how a mesoscopic atomic frequency comb preserves an initial multiphoton state over several revivals, we will now examine how such a frequency comb can also be used to generate pulses of nonclassical light. In particular, we show that a short coherent input pulse is converted to periodic single photon pulses with sub-Poissonian statistics.

We again consider an atomic frequency comb, as presented in Fig. 5.2.1(a), where the individual spin frequencies are given by $\omega_\mu = \omega_c + \mu\Delta\omega$ with $\mu = \{-(m-1)/2, ..., (m-1)/2\}$ for $m = 7$ frequency clusters. The collective coupling strength of the μ-th sub-ensemble follows a Gaussian envelope $\Omega_\mu = \Omega_0 \exp\left[-(\omega_c - \omega_\mu)^2/2\lambda^2\right]$ with $\lambda/2\pi = 150$ MHz and $\Omega_0/2\pi = 30$ MHz. The radiative cavity and spin loss terms are taken as $\kappa/2\pi = 0.2$ MHz, and $\gamma_h = \kappa/40$, respectively, while non-radiative dephasing is neglected in the following ($\gamma_p = 0$).

We drive this spin-cavity system resonantly with a short coherent pulse of intensity, $\eta(t) = 40\kappa$, for $0 \le t \le t'$, and $\eta(t) = 0$, otherwise. The pulse duration t' is chosen to be $1/5$ of the characteristic time scale $2\pi/\Delta\omega$. Before the pulse arrives, the initial spin-cavity system is unexcited and the cavity is in the vacuum state. Figure 5.3.1 depicts the resulting dynamics of the cavity photon number $\langle a^\dagger a\rangle$ and the spin expectation value $\langle\sigma_i^+\sigma_i^-\rangle_{\omega_i=\omega_c}$ of the central frequency cluster for ensembles containing from $N = 7$ to $N = 105$ spins. As in the preceding sections, we

---

[10] This section is based on the publication [85], from which also figures and parts of the text are taken. The numerical calculations presented here were performed by Himadri Dhar who also implemented the time dependent variational renormalization group method used in this section. I was involved in the theoretical interpretation and analysis of the results.
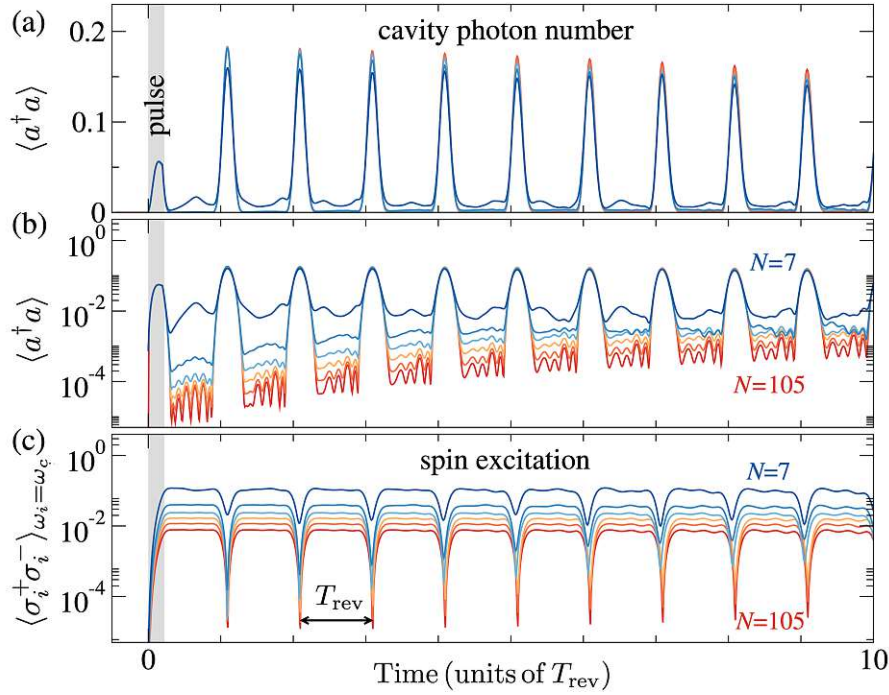
Figure 5.3.1.: Temporal evolution of the mesoscopic spin-cavity system after a short coherent input pulse. The figures show the cavity photon number $\langle a^\dagger a \rangle$ in (a) linear and (b) log scale, and (c) the spin excitation at resonance $\langle \sigma_i^+ \sigma_i^- \rangle_{\omega_i = \omega_c}$, varying with time, and for ensembles containing $N = 7$, 21, 35, 49, 70, and 105 spins, shown with color varying from blue to red. The shaded region at times $0 \leq t \leq t'$ indicates the short rectangular driving pulse and $\Delta\tau$ is the interval between the periodic revivals.

observe a periodic pulse train of light, exhibited by sharp revivals of the average cavity photon number. The peaks correspond to the collective transfer of excitations from the spin ensemble to the cavity, as evident from the sharp decrease in the spin excitation at the revivals. The time interval between subsequent peaks is given by $T_{\text{rev}} \approx 2.2\pi/\Delta\omega = 27.5$ ns. We note that during the transfer of energy from the cavity to the ensemble, larger ensembles, i.e., larger N, not only lead to enhanced coupling, but also produce more stable and sharper photon pulses as excitations are distributed over more spins. In contrast, for few spins, significant photon excitations may also exist between the peaks as observed in Fig. 5.3.1(b).

In the following, we are interested in the photon statistic of the periodic light pulses emerging after the coherent input pulse. For that purpose, we calculate the equal-time second order correlation function at time t, defined as [229]

$$g_2(t, 0) = \frac{\langle a^\dagger(t) a^\dagger(t) a(t) a(t) \rangle}{\langle a^\dagger(t) a(t) \rangle^2}, \tag{5.18}$$

which serves as a signature for nonclassical light with $g_2(t, 0) \geq 1$ for all classical
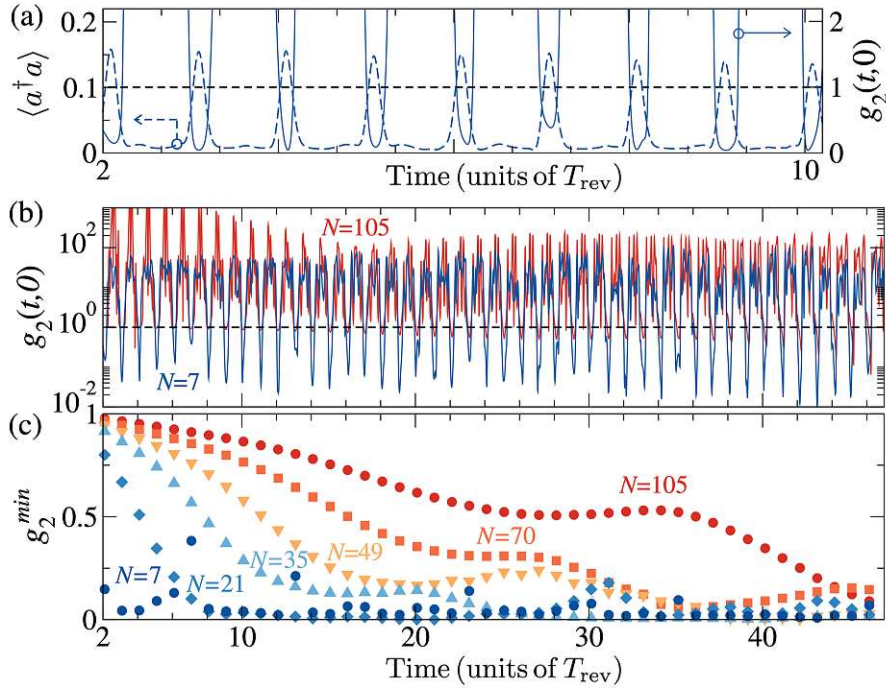
Figure 5.3.2.: Photon statistics of the transient cavity field (all parameters and color codings are the same as in Fig. 5.3.1). (a) Equal-time second-order correlation function $g_2(t,0)$ in comparison with the cavity photon number $\langle a^\dagger a \rangle$, for $N = 7$. (b) Temporal evolution of $g_2(t,0)$ for $N = 7$ and 105. (c) Minimum value of $g_2(t,0)$ during a pulse revival, g_2^{min}, for $N = 7$, 21, 35, 49, 70, and 105. The horizontal black-dashed line in (a) and (b) corresponds to $g_2(t,0) = 1$ for coherent light.

light sources (unity for coherent light) and $g_2(t,0) < 1$ for nonclassical light. While the coherent light pulse injected into the cavity is characterized by $g_2(t,0) = 1$ (not shown), we observe in Fig. 5.3.2(a) that at times when the subsequent photon pulses arrive for $N = 7$ the field is distinctly sub-Poissonian, i.e., $g_2(t,0) < 1$. In contrast to our findings in the previous section, the statistic of the light pulses thus changes significantly from classical to nonclassical during the first few revivals. This behavior can be explained by the finite size of the spin ensemble as detailed below. Note that a similar phenomenon occurs for $N = 105$ spins, however, on a much slower time scale [see Fig. 5.3.2(b)]. Here, the Poissonian statistics, $g_2(t,0) = 1$, of the initial pulse is conserved during several revivals before $g_2(t,0)$ starts to drop significantly below unity reaching the unambiguous single-photon regime, $g_2(t,0) \ll 1$, at later times. Figure 5.3.2(c) demonstrates that the larger the spin ensemble, the slower this conversion to a non-classical light pulse is. For an efficient single-photon source all higher order correlation functions $g_n(t,0) = \langle a^{\dagger n} a^n \rangle / \langle a^\dagger a \rangle^n$ must also satisfy the relation $g_n(t,0) < 1$, which we explicitly checked in Fig. 5.3.3 up to order $n = 4$.
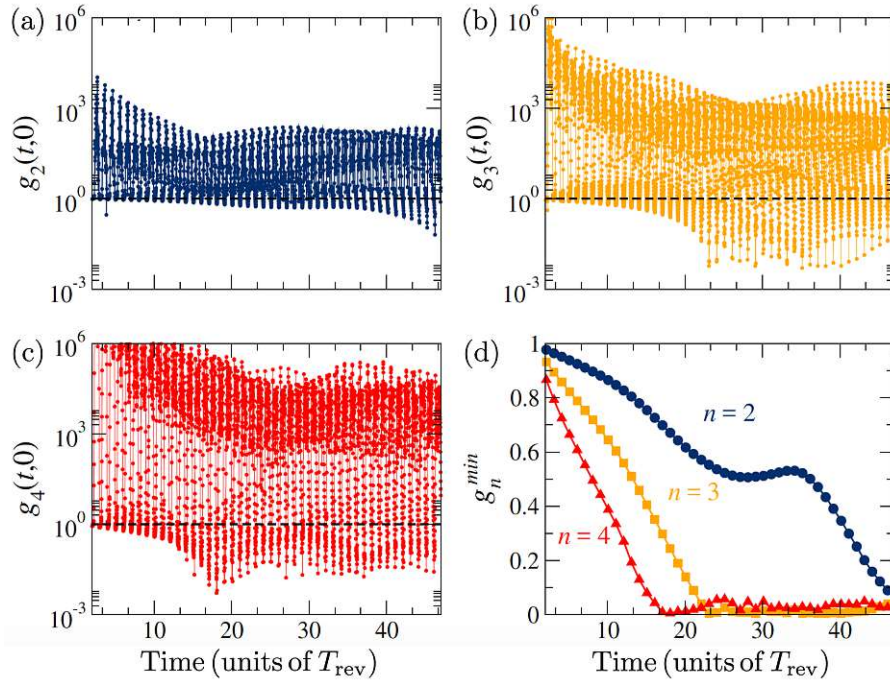
Figure 5.3.3.: Equal-time higher order correlation functions, $g_n(t,0)$ [with $n = 2, 3, 4$], for the nonclassical periodic pulse train presented in Fig. 5.3.1(a,b) for a spin ensemble containing $N = 105$ spins. (d) The minimum of $g_n(t,0)$ during each pulse. As can be seen, the higher order correlation functions all drop considerably below unity.

To understand the process of the conversion from a coherent light pulse to single-photon pulses, we revisit the energy spectrum of the Tavis-Cummings Hamiltonian (5.9) in the one- and two-excitation subspace. As discussed in the previous section, the requirement for the formation of pulsed revivals is an equidistant comb-shaped
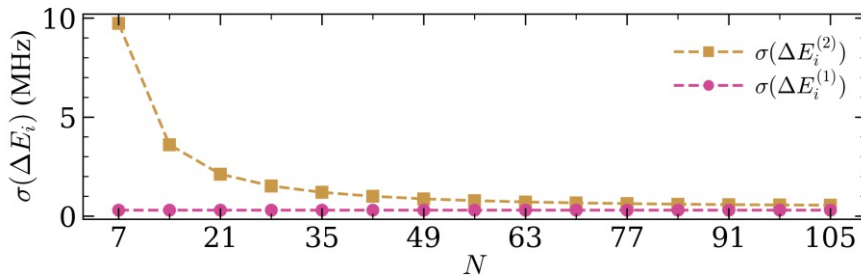
Figure 5.3.4.: Standard deviation of the energy spacings $\Delta E_i^{(1,2)}$ in the one- and two-excitation subspace of the Tavis-Cummings Hamiltonian (5.9) as a function of the number of spins in the atomic frequency comb. Notably, only the one-excitation subspace features an equidistant energy spectrum for all system sizes, whereas the two-excitation subspace deviates strongly from an equidistant spectrum for small spin ensembles.

energy spectrum. In Fig. 5.3.4, we, therefore, present the standard deviation of the energy spacings $\Delta E_i^{(1)}$ and $\Delta E_i^{(2)}$ in the two subspaces. We observe that only the one-excitation subspace features an equidistant energy spectrum for all system sizes. The two-excitation subspace shows equidistant energy levels for large ensembles but deviates strongly from such a spectrum for smaller spin ensembles. Consequently, only the single-photon components show revivals at multiples of the time T_{rev} for small spin ensembles, while higher multiphoton contributions are filtered from the periodic pulses.

Chapter 6.

Spin echoes in the strong coupling regime

The interaction between electromagnetic fields and ensembles of spins is also the basis for magnetic resonance, which in the form of nuclear magnetic resonance (NMR) and electron spin resonance (ESR) is an invaluable diagnostic tool in a variety of scientific fields such as in medicine [70], biophysics [230], and chemistry [231]. As we already encountered, inhomogeneous broadening leads to the dephasing of an initial excitation in a spin ensemble. To extract information from such a sample, a vast repertoire of sophisticated pulse sequences exists [73]. The majority of these sequences is based on the Hahn echo [76], which is illustrated in Fig. 6.0.1. The Hahn echo sequence consists of a $\pi/2$ excitation pulse followed by a refocusing π pulse after some time interval τ. The latter leads to a rephasing of the spin ensemble, creating a detectable spin echo after another time interval τ. In
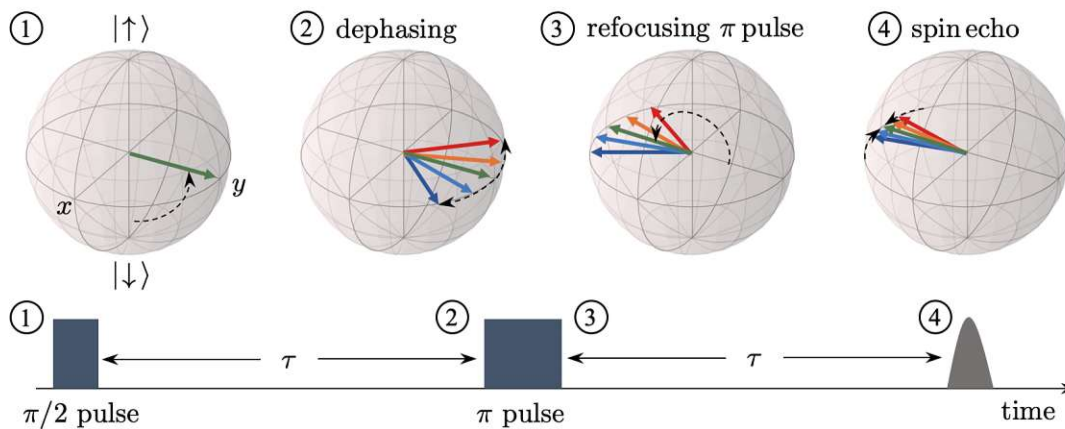
Figure 6.0.1.: Visualization of the Hahn echo sequence. First, a $\pi/2$ pulse is applied to excite the spins to the equator of the Bloch sphere ①. After some time τ during which the spins dephase ②, a refocusing π pulse is applied—reversing the relative phase of the individual spins ③. Consequently, the spins rephase, producing a spin echo ④ after another time interval τ.

this chapter, we present a novel phenomenon in ESR, which occurs when the Hahn echo is transferred to the context of a strongly coupled spin-cavity system [41, 232]. Here, the strong coupling combined with an imperfect refocusing pulse results in a self-sustained train of periodic echoes. We provide a theoretical explanation of this effect using a simple geometric model based on spins rotating on the Bloch sphere, backed up by numerical calculations using the Maxwell-Bloch equations.

6.1. Self-sustained spin echoes in pulsed electron spin resonance[11]

Electron spin resonance (ESR), which started with the early experiments by Zavoisky [234] in the 1940s, has become an indispensable spectroscopy technique used, e.g., for the analysis of the structure and dynamics of molecules [235, 236], material science [237], or quantum sensing and information processing [238–240]. Developments in the latter area have benefited greatly from the progress in the fabrication of superconducting microwave cavities, for which recently the strong coupling regime has been demonstrated [33–35, 37, 40, 42]. Here, the coherent exchange of information between the microwave cavity and the spin ensemble exceeds the individual decay rates of the two subsystems, which is a requirement for an efficient transfer of quantum information [34, 43, 241, 242]. Apart from its importance for quantum technology, a strong coupling rate also enhances the sensitivity in ESR applications [74, 75] going beyond classical ESR models [72, 73].

In the following, we transfer the conventional Hahn echo to the strong coupling regime using a superconducting microwave cavity strongly coupled to a paramagnetic spin ensemble. Specifically, we compare continuous and pulsed ESR measurements of a strongly coupled spin ensemble based on isolated phosphorus donors in a ^{28}Si host matrix with a weakly coupled ensemble of P_2 dimers also present in the sample.

The experimental scheme is sketched in Fig. 6.1.1(a-c). The cavity is a planar superconducting lumped element resonator patterned into a 150 nm thin Nb film on an intrinsic ^{nat}Si substrate and located next to a microwave feedline, which allows us to probe the microwave transmission through the device. The sample is a 20 μm thin slab of [100] oriented ^{28}Si:P mounted onto the cavity [see Fig. 6.1.1 (c)] and kept at a temperature of $T = 50$ mK. A static magnetic field B_0 is applied in-plane of the superconducting resonator. For details of the experimental setup see

---

[11] This section is based on the joint publication [41] from which also parts of the text and figures are taken. The experiment was performed by Stefan Weichselbaumer and Christoph W. Zollitsch at the Walther-Meißner-Institute of the the Bavarian Academy of Sciences under the supervision of Martin S. Brandt, Rudolf Gross, and Hans Hübl. The theoretical modeling and interpretation was performed by myself under the supervision of Stefan Rotter. A detailed description of the experimental setup is given in the PhD thesis of Stefan Weichselbaumer [233].
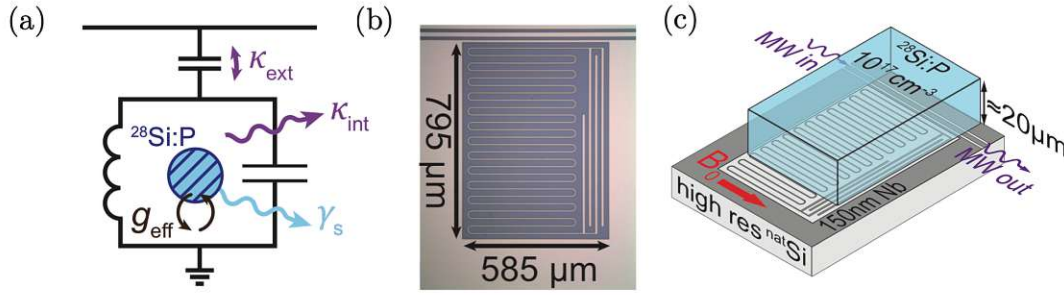
Figure 6.1.1.: (a) Circuit diagram of the ESR setup consisting of phosphorus donors in silicon coupled collectively with strength g_{eff} to a lumped element resonator. The intrinsic and external losses of the resonator are denoted by κ_{in} and κ_{ext}, respectively, and γ_s denotes the spin losses. (b) Microscope image of the lumped element resonator next to a microwave feedline. (c) Schematic of the 20 μm thin ^{28}Si:P sample mounted on top the resonator. In purple the input and output of the microwave feedline is indicated and the red arrow shows the in-plane magnetic field B_0. Figure adapted from ref. [41].

refs. [41, 233].

Continuous-wave ESR spectroscopy

First, the sample containing phosphorus donors as well as P_2 dimers was characterized by continuous-wave ESR spectroscopy. Figure 6.1.2 (a) depicts the normalized microwave transmission $|S_{21}|^2$ as a function of the applied magnetic field B_0 and the frequency of the input field ω_p. At $B_0 = 168.5$ mT, a bare cavity frequency of $\omega_c/2\pi = 4.8116$ GHz was observed. The half-width-at-half-maximum (HWHM) line width was determined using a robust circle-fitting algorithm [243], giving $\kappa_c/2\pi = 534.85$ kHz, which corresponds to a total quality factor of $Q = \omega_c/2\kappa_c = 4498$. The coupling rate of the cavity to the feedline is $\kappa_{\text{ext}}/2\pi = 304.15$ kHz. Similarly, the spin relaxation rate is extracted using a Lorentzian fit along the field axis far detuned from the cavity yielding $\gamma_s/2\pi = 279.03$ kHz. Two distinct avoided crossings were observed at $B_0 = 170.1$ mT and $B_0 = 174.3$ mT, corresponding to the two hyperfine-split lines of phosphorus donors in silicon. The avoided crossings indicate that the ensemble of phosphorus spins couples strongly to the cavity. The effective collective coupling strength $g_{\text{eff}}/2\pi = 1.54$ MHz extracted at the vacuum Rabi splitting at $B_0 = 170.19$ mT, hence, exceeds the intrinsic loss rates κ_c and γ_s.

To obtain further information about the spin species present in the sample, the transmission linewidth κ_T outside the avoided crossings is analyzed as a function of the magnetic field. Figure 6.1.2(b) shows the linewidth κ_T extracted from the data in Fig. 6.1.2(a). Note that far from the avoided crossings the linewidth is given by the bare cavity linewidth $\kappa_T \sim \kappa_c$. At $B_0 = 171.5$ mT we find a broad resonance structure, which is assigned to dangling bond defects at the (100)Si/SiO$_2$ interface,
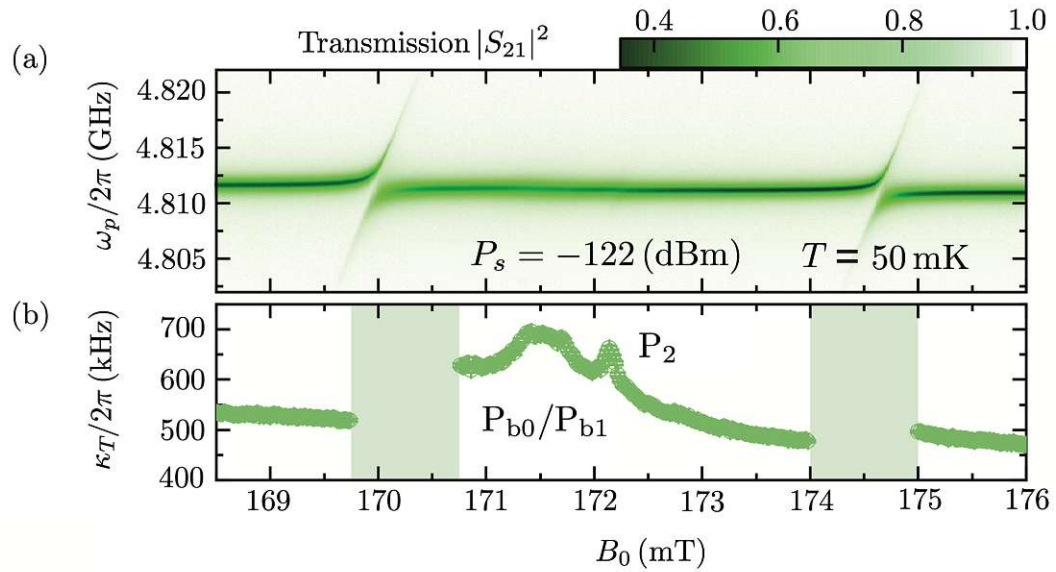
Figure 6.1.2.: (a) Measured normalized transmission $|S_{21}|^2$ as a function of the probe frequency ω_p and the applied magnetic field B_0. Two avoided crossings are visible, indicating strong coupling between the hyperfine-split transitions of the phosphorus donors and the cavity. (b) Linewidth $\kappa_T/2\pi$ (HWHM) extracted from the transmission spectrum in (a) as a function of the magnetic field B_0. Two additional spectroscopic features are observed, which are attributed to dangling bond defects P_{b0}/P_{b1} and P_2 dimers, respectively. Figure adapted from ref. [41].

also known as P_{b0}/P_{b1} defects [244, 245]. Furthermore, a sharp signature emerges at $B_0 = 172.2\,\mathrm{mT}$ corresponding to statistically formed exchange-coupled donor pairs, called P_2 dimers, with a concentration $[P_2] \ll [P]$ [246–249]. The analysis of this P_2 dimer peak yields a spin relaxation rate $\gamma_{s,P_2}/2\pi = 1.74\,\mathrm{MHz}$ and an effective coupling rate $g_{\mathrm{eff},P_2}/2\pi = 0.35\,\mathrm{MHz}$ [41]. This sets the P_2 dimers in the weak coupling regime and enables a direct comparison of the dynamics in the weak and strong coupling regime under the same experimental conditions.

Pulsed ESR spectroscopy

In a next step, a Hahn echo sequence is applied using two Gaussian-shaped pulses with a width of $1\,\mu\mathrm{s}$ and $2\,\mu\mathrm{s}$ and a pulse spacing of $\tau = 80\,\mu\mathrm{s}$. Figure 6.1.3 (a) shows the Hahn echoes detected over time for a sweep of the magnetic field B_0. Note that the origin of the time axis is set to the maximum of the first echo signal. The experimental results demonstrate that the first conventional Hahn echo (at $t = 0$) is present for both, the weakly and the strongly coupled spin ensembles. However, a fundamental difference between weak and strong coupling arises on longer time scales. Particular attention deserve subpanels ① and ③, corresponding to the
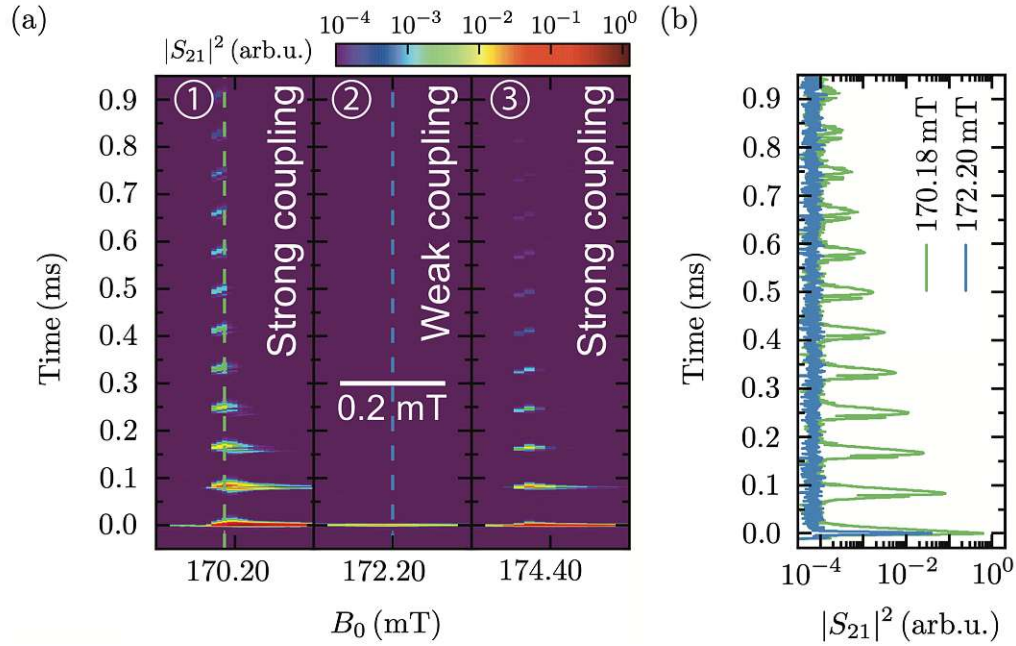
Figure 6.1.3.: (a) Detected microwave intensity $|S_{21}|^2$ as a function of time and applied magnetic field B_0 after a conventional Hahn-pulse sequence (not shown). The strongly coupled hyperfine transitions (① and ③) display several echo signals, while only a single (conventional) Hahn echo is visible for the weakly coupled P_2 dimers (②). (b) Microwave intensity $|S_{21}|^2$ as a function of time for fixed magnetic field [dashed lines in (a)] for the strongly coupled hyperfine transitions (green) and the weakly coupled P_2 dimers (blue). Figure adapted from ref. [41].

strong coupling case. Here, the first Hahn echo is followed by a periodic sequence of echo signatures, which are timed with a delay equal to the pulse delay τ. In contrast, only the first conventional Hahn echo is present for the weakly coupled P_2 dimers shown in subpanel ②.

This marked difference is even more apparent in Fig. 6.1.3 (b), where we show time traces recorded at the fixed magnetic fields of $B_0 = 172.20$ mT and 170.18 mT [dashed lines in Fig. 6.1.3 (a)] corresponding to the weak and strong coupling regime. While only the first conventional Hahn echo appears for the P_2 dimers ($T_{2,P_2} = 4.67(13)$ ms; see supplementary material of ref. [41]), 12 echoes separated by τ are observed for the strongly coupled hyperfine transitions ($T_{2,P} = 2.37(8)$ ms; see supplementary material of ref. [41]).

The relevant mechanism leading to this unique dynamical evolution can be best understood when revisiting the conventional Hahn echo sequence shown in Fig. 6.1.4. For simplicity, we assume here that all spins end up in the xy-plane after the first $\pi/2$-pulse (see panels 1-3), although the spatial variation of the excitation field B_1 and the frequency distribution of the spin ensemble inevitably lead to rota-

tion errors. Realistically, the net dipole moment generated in the xy-plane during this first pulse leads to strong collective coupling with the resonator and, hence, rapid deexcitation of the spin system (not depicted). However, dephasing quickly reduces this dipole moment and thereby effectively suppresses this spin decay channel. After an evolution time τ, the second pulse is injected to start the refocusing
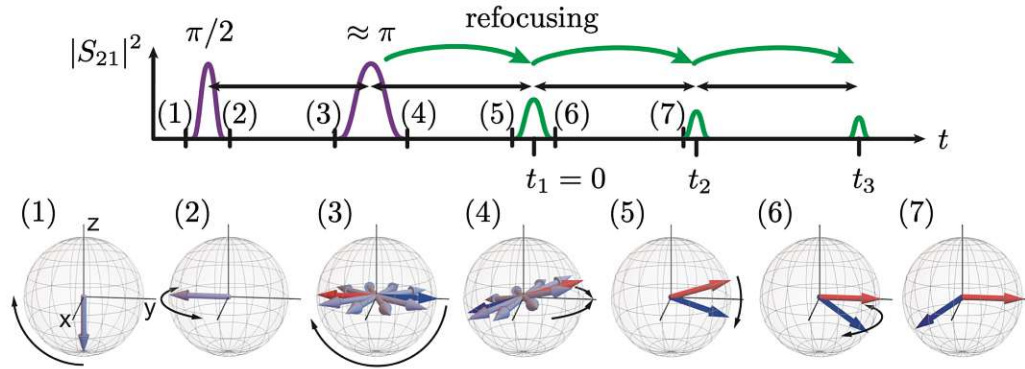
Figure 6.1.4.: Schematic of the Hahn echo sequence and the associated states in the Bloch sphere (exterior black arrows indicate the ensuing spin dynamics). A $\pi/2$ pulse is applied between (1) and (2) and an imperfect π pulse between (3) and (4), leading to the first (conventional) Hahn echo between (5) and (6). For the subsequent dynamics we highlight only spins lying in opposite S_y directions when the refocusing π pulse arrives at (3) (blue and red arrows), since these spins are crucial for the additional echoes at later times. The strong coupling leads to a spin rotation during the first echo (5)-(6), which results in an asymmetry in the S_y projection of the highlighted spins. In (7), this causes a net dipole moment and a second (unconventional) echo. Figure adapted from ref. [41].

process. A perfect π pulse would lead to the complete refocusing of all spins after another period τ, creating the first (conventional) Hahn echo without any subsequent echoes. With the rotation angle realistically deviating from π, however, the refocusing is imperfect, such that the spins end up at different latitudes on the Bloch sphere, depending on their detuning $\delta\omega$ from the average Larmor frequency (see panels 3-5). This mechanism can also be understood as a frequency encoding of spin packets depending on their orientation on the Bloch sphere at the arrival time of this imperfect π-pulse. Specifically, we identify spin packets that point in opposite directions on the S_y-axis when the imperfect π-pulse arrives using red and blue arrows in the panels in Fig. 6.1.4. These will be particularly relevant for the generation of the subsequent pulses. Their frequency detunings are determined by those multiples of π-rotations that the spins already undertook at the arrival of the refocusing pulse: $\delta\omega = 2n\pi/\tau$ (red spins) and $\delta\omega = (2n+1)\pi/\tau$ (blue spins) with $n \in \mathbb{Z}$. In this way, spins with significantly different individual detuning values $\delta\omega$ are now encoded in the same packet. At a time τ after the imperfect π-pulse, when spins (partially) refocus, they emit the first (conventional) Hahn echo through the

coupling to the resonator. Notably, the net dipole moment in the xy-plane created in this refocusing process, together with the strong coupling to the microwave field also leads to a significant spin decay. Importantly, this decay is realized on the Bloch sphere as a spin rotation during this first Hahn echo that affects the projection of the dipole moment on the xy-plane differently for the blue and red spin packets (see panels 5 & 6). This rotation becomes significant at a time τ after the first Hahn echo, where these spin packets again point in opposite S_y-directions (red and blue arrows in panel 7): with the xy projection of these two spin vectors now having different lengths, they give rise to another net dipole moment that produces the (unconventional) second Hahn echo. Here, the process starts all over again, producing the third echo and so on.

Note that without the spin rotation during the first Hahn echo, the red and blue spins would maintain the same xy projection, such that there is no net dipole and therefore no subsequent echo at $t = t_2$ (panel 7). In this way, one understands not only how one echo causes the next but also why strong coupling is important. In addition, the imperfect rotation angle is a necessary condition to observe multiple echoes, as no frequency encoding of spin packets would occur otherwise (panel 5) [see also Fig. 6.1.6].

To underpin this heuristic explanation, we calculate the dynamics of the spin-cavity system by numerically solving the Maxwell-Bloch equations (2.20a)-(2.20c) for two rectangular driving pulses with a width of 1μs and 2μs, a pulse delay of $\tau = 80\mu$s, and a pulse amplitude of $\eta/\kappa_c = 1.08 \times 10^5$. We set $\omega_c = \omega_p$, while the mean frequency of the spin ensemble is slightly detuned from the resonator frequency by $(\omega_s - \omega_c)/2\pi = 0.14\,\mathrm{MHz}$ to match the experimental conditions in the strong-coupling regime (at $B_0 = 170.18$ mT). We account for the dephasing of the spin ensemble by introducing the phenomenological Lorentzian spin spectral density, $\rho(\omega) = \{\pi\gamma_s[1 + (\omega - \omega_s)^2/\gamma_s^2]\}^{-1}$, with width γ_s and mean frequency ω_s, characterizing the frequency distribution of the spin ensemble. For simplicity, we assume that all spins couple with the mean coupling strength $g_k = g_0 = g_{\mathrm{eff}}/\sqrt{N}$.

The calculated average resonator photon number $|\langle a(t)\rangle|^2/N$ following an ordinary Hahn-echo sequence is presented in Fig. 6.1.5 (a). Most importantly, we find that these numerical results nicely reproduce the multiple echo signatures found experimentally [see Fig. 6.1.3 (b)], using only minimalistic assumptions. Additionally, these simulations provide the average spin expectation values $S_{\mathrm{av}}^{x,y,z} := \sum_k \langle \sigma_k^{x,y,z}\rangle/N$, which are not directly accessible in the experiment. From these quantities we can directly evaluate the macroscopic dipole moment $\sum_k \langle \sigma_k^-\rangle = N(S_{\mathrm{av}}^x + iS_{\mathrm{av}}^y)$, which couples the spin dynamics to the resonator field via Eq. (2.20a). Figure 6.1.5 (b,c) shows that the arrival of the first conventional Hahn echo, at $t = 0$, is accompanied by peaks in the average dipole moments S_{av}^x and S_{av}^y, which leads to a resonator-enhanced decay of the spin excitation S_{av}^z [see also gray inset of Fig. 6.1.5(d)]. Confirming our heuristic model from above, the same coincidence between peaks in the dipole moments $(S_{\mathrm{av}}^x, S_{\mathrm{av}}^y)$, the steps in the decay of S_{av}^z, and
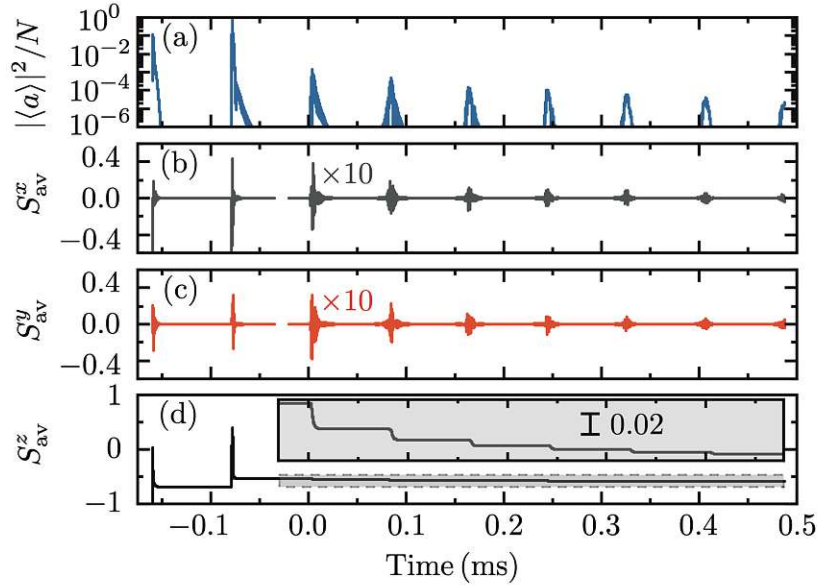
Figure 6.1.5.: Temporal evolution of (a) the average resonator photon number $|\langle a \rangle|^2/N$, (b,c) the average spin expectation values $S_{av}^{x,y} = \sum_k \langle \sigma_k^{x,y} \rangle/N$, and (d) $S_{av}^z = \sum_k \langle \sigma_k^z \rangle/N$ calculated from the semiclassical Maxwell-Bloch equations (2.20a)-(2.20c) for two rectangular input pulses with widths of 1 and $2\,\mu$s, respectively. The delay of the refocusing pulse is given by $\tau = 80\,\mu$s and the initial time is set to -2τ such that the first echo arrives at $t \approx 0$. The inset in (d) shows a zoom of the gray shaded area. Figure adapted from ref. [41].

the emission of a photon pulse into the resonator is observed for all subsequent (unconventional) Hahn echoes. This reduced model thus already reproduces all salient features of the experiment.

Pulse imperfections and coupling strength

To further identify the role of pulse imperfections and strong coupling in the formation of the multiple echoes, we present here additional calculations, where the action of the two microwave pulses of the Hahn echo sequence is included in the initial conditions of our theoretical model. The purpose of this procedure is to unravel the complicated strong-coupling dynamics during the $\pi/2$ and π pulses from the subsequent dynamics. Specifically, we solve the Maxwell-Bloch equations for the initial conditions $\langle a \rangle = 0$, $\langle \sigma_k^x \rangle = -\cos(\Delta_k \tau)\cos(\alpha)$, $\langle \sigma_k^y \rangle = -\sin(\Delta_k \tau)$, and $\langle \sigma_k^z \rangle = \cos(\Delta_k \tau)\sin(\alpha)$ at $t = 0$, where $\Delta_k = \omega_k - \omega_p$ is the detuning between the spin frequency and the reference rotating frame, $\tau = 20\,\mu$s is imposed inter-pulse delay, and α is the rotation angle of the emulated refocusing pulse. These particular initial conditions correspond to the following situation: First, all spins are

collectively brought into the xy-plane by a perfect $\pi/2$ rotation along the y-axis. Then, after a free evolution time τ, the spins are rotated by an angle α along the y-axis. Note that this procedure allows us to study the impact of the spin-resonator coupling and rotation errors independently of the imperfections imposed by the microwave pulses.
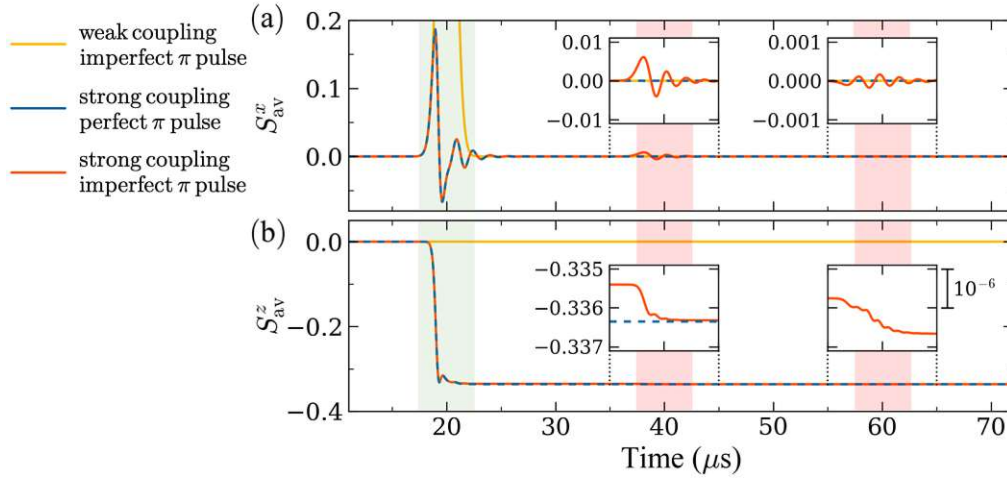
Figure 6.1.6.: Average spin expectation values $S_{\text{av}}^{x,z} = \sum_k \langle \sigma_k^{x,z} \rangle / N$ versus time for a spin ensemble starting from an initial condition that imitates a Hahn echo sequence of a perfect $\pi/2$-rotation followed by an α-rotation right before $t = 0$. Comparison of $S_{\text{av}}^{x,z}$ for (i) a strongly coupled spin ensemble, $g_{\text{eff}}/2\pi = 1.56\,\text{MHz}$, after a perfect rotation $\alpha = \pi$ (blue dashed line) and (ii) an imperfect rotation $\alpha = 0.95 \times \pi$ (red line) as well as (iii) a weakly coupled spin ensemble, $g_{\text{eff}}/2\pi = 1.56\,\text{kHz}$, after an imperfect rotation $\alpha = 0.95 \times \pi$ (yellow line). Notably, the conventional Hahn echo at $t = 20\,\mu\text{s}$ (green shaded area) is present in all three cases, while additional echoes at $t = 40\,\mu\text{s}$ and $t = 60\,\mu\text{s}$ (red shaded area) are visible only for the combination of imperfect rotations and strong coupling (insets).

Figure 6.1.6 depicts the average spin expectation values $S_{\text{av}}^{x,z} = \sum_k \langle \sigma_k^{x,z} \rangle / N$ for three different configurations: (i) a strongly coupled spin ensemble ($g_{\text{eff}}/2\pi = 1.56\,\text{MHz}$) and a perfect ($\alpha = \pi$) refocusing pulse, (ii) a strongly coupled spin ensemble ($g_{\text{eff}}/2\pi = 1.56\,\text{MHz}$) and an imperfect ($\alpha = 0.95 \times \pi$) refocusing pulse, and (iii) a weakly coupled spin ensemble ($g_{\text{eff}}/2\pi = 1.56\,\text{kHz}$) and an imperfect ($\alpha = 0.95 \times \pi$) refocusing pulse. We first note that the conventional Hahn echo at $t = 20\,\mu\text{s}$ is observed in all three cases in S_{av}^x, independent of both coupling strength and rotation error. However, multi-echo signatures are visible only for imperfect refocusing pulses and strong coupling. While at strong coupling the results for the perfect and the imperfect rotation angle almost overlap during the conventional Hahn echo, the additional echoes at $t = 40\,\mu\text{s}$ and $t = 60\,\mu\text{s}$ arise only for $\alpha = 0.95 \times \pi$. This can be intuitively understood from Fig. 6.1.4 (panel 5) as the imperfection of the spin rotation introduces the frequency encoding enabling the

unconventional echoes at later times. As also anticipated from Fig. 6.1.4 (panel 6), the spin rotation due to the strong spin cavity coupling is another necessary condition to observe significant multi-echo signatures. Although for $g_{\mathrm{eff}}/2\pi = 1.56\,\mathrm{kHz}$ the spins build up a large dipole moment S^x_{av} during the conventional Hahn echo, the coupling is too weak to cause a noticeable rotation of the spins on the Bloch sphere and therefore no echoes are visible at later times. Thus, our results confirm that the cavity-enhanced rotation of the spins in combination with the imperfect refocusing pulse are the crucial building blocks for the formation of multiple echoes.

Summary and outlook

Hybrid quantum systems, which consist of ensembles of spins coupled to a cavity, play a pivotal role in many experiments on the foundations of quantum optics and technological applications for future quantum information processing. In this thesis, we have provided a broad repertoire of theoretical methods to study and understand spin ensembles in cavities in very different domains.

For macroscopic ensembles, we have used the semiclassical Maxwell-Bloch equations as well as a Volterra integral equation approach. While the latter method is valid only in the linear regime of few excitations, the Maxwell-Bloch equations describe also the transition into the nonlinear regime, which produces a variety of interesting effects. Here, we focused on two fundamental nonlinear phenomena— optical bistability and critical slowing down. On the one hand, we demonstrated that the onset of bistability depends not only on the width but also on the exact shape of the spectral spin distribution. On the other hand, we found a universal power-law scaling for the critical slowing down of the cavity field amplitude. Here, the system's complexity is smeared out, such that inhomogeneously broadened ensembles behave similarly as very simple systems without inhomogeneous broadening. Both phenomena, the optical bistability and the critical slowing down, were realized in an experiment with nitrogen vacancy centers in diamond.

Furthermore, we used a cumulant expansion method to calculate quantum corrections to the semiclassical Maxwell-Bloch equations setting up a semiclassial-to-quantum boundary. Interestingly, we demonstrated that even very large ensembles of about 10^4 spins can show deviations from a semiclassical description in the vicinity of the bistable regime. We expect that the criterion we have established for the semiclassical-to-quantum limit will be useful to check the validity of Maxwell-Bloch equations in a variety of different setups and contexts.

Inhomogeneous broadening is often a dominant source of decoherence in ensemble-based quantum devices. In this thesis, we have demonstrated that one can overcome this limitation for atomic frequency combs by burning narrow spectral holes at judiciously chosen positions of the spin distribution. This procedure leads to a dramatic prolongation of the observed revival dynamics.

In addition, we have introduced a variational renormalization group method that allows studying mesoscopic spin ensembles of up to one hundred spins coupled to a cavity on a fully quantum mechanical basis. We used this novel technique to provide a rigorous treatment of atomic frequency combs in the strong-coupling regime of cavity QED. In particular, we demonstrated that arbitrary multiphoton states are absorbed by the comb-shaped spin ensemble and re-emitted with high fidelity at well-defined later times. The absorption and re-emission process thereby acts as a parity transformation on the initial cavity state. Using the same method, we have shown that a mesoscopic atomic frequency comb can generate periodic pulses of nonclassical light from a short coherent input pulse. An experimental realization of this concept using superconducting qubits is currently being implemented by Elena Redchenko in the group of Johannes Fink at IST Austria.

Finally, we reported on a novel phenomenon in electron spin resonance, where the strong coupling between an inhomogeneously broadened spin ensemble and a cavity leads to self-sustained echoes after a conventional Hahn echo sequence. We have provided a theoretical interpretation of this effect based on the Maxwell-Bloch equations and a simple geometric model of spins rotating on the Bloch sphere. While our results show a good qualitative agreement with the experiments, additional calculations and a detailed comparison with further measurements are necessary to provide a quantitative description of the measured echo signature. Open topics that could be the scope of future studies are quantum signatures in the periodic echo train as well as the modeling of the decay of the subsequent echoes over time.

We hope that with the results presented in this thesis we have demonstrated that spin ensembles in cavity QED provide an exciting stage for new physics. In particular, we aim to illustrate with our work that inhomogeneous broadening is not just a detrimental effect that blurs ideal homogeneous setups. Instead, the additional frequencies in a spin ensemble allow new dynamical regimes and additional control over the light-matter interaction in hybrid quantum devices.

Appendix

A. Transformation to the rotating frame

In the following, we transform the Tavis-Cummings Hamiltonian (1.1) into the frame rotating with ω_p to remove the explicit time dependence of the external driving field. For this purpose, we perform the unitary transformation

$$\tilde{H} = U\,H\,U^\dagger + i\,\frac{\partial U}{\partial t}U^\dagger, \tag{A.1}$$

where

$$U = e^{i\omega_p t\left(a^\dagger a + \sum_k \frac{1}{2}\sigma_k^z\right)}, \tag{A.2}$$

yielding

$$\begin{aligned}
\tilde{H} &= U\,H\,U^\dagger - \omega_p a^\dagger a - \sum_{k=1}^{N}\frac{1}{2}\omega_p\sigma_k^z \\
&= (\omega_c - \omega_p)\,a^\dagger a + \frac{1}{2}\sum_{k=1}^{N}(\omega_k - \omega_p)\sigma_k^z \\
&\quad + \sum_{k=1}^{N}g_k[\tilde{\sigma}_k^-\tilde{a}^\dagger + \tilde{\sigma}_k^+\tilde{a}] + i[\eta(t)\tilde{a}^\dagger e^{-i\omega_p t} - \eta^*(t)\tilde{a}e^{i\omega_p t}].
\end{aligned} \tag{A.3}$$

Here, $\tilde{\sigma}_k^- \equiv e^{i\omega_p t\frac{1}{2}\sigma_k^z}\,\sigma_k^-\,e^{-i\omega_p t\frac{1}{2}\sigma_k^z}$, $\tilde{\sigma}_k^+ \equiv e^{i\omega_p t\frac{1}{2}\sigma_k^z}\,\sigma_k^+\,e^{-i\omega_p t\frac{1}{2}\sigma_k^z}$, $\tilde{a} \equiv e^{i\omega_p t a^\dagger a}\,a\,e^{-i\omega_p t a^\dagger a}$, and $\tilde{a}^\dagger \equiv e^{i\omega_p t a^\dagger a}\,a^\dagger\,e^{-i\omega_p t a^\dagger a}$, respectively, which can be evaluated with the following useful combinatorial lemma [250, page 64]

$$e^A B e^{-A} = B + [A, B] + \frac{1}{2!}[A,[A,B]] + \frac{1}{3!}[A,[A,[A,B]]] + \dots. \tag{A.4}$$

Equation (A.4), together with the commutation relations (1.2) and (1.3), gives

$$\begin{aligned}
e^{i\omega_p t\frac{1}{2}\sigma_k^z}\,\sigma_k^-\,e^{-i\omega_p t\frac{1}{2}\sigma_k^z} &= \sigma_k^- + \frac{i\omega_p t}{2}[\sigma_k^z,\sigma_k^-] + \frac{1}{2!}\left(\frac{i\omega_p t}{2}\right)^2[\sigma_k^z,[\sigma_k^z,\sigma_k^-]] + \dots \\
&= \sigma_k^-\sum_{n=0}^{\infty}\frac{1}{n!}(-i\omega_p t)^n = \sigma_k^- e^{-i\omega_p t},
\end{aligned} \tag{A.5}$$

$$e^{i\omega_p t \frac{1}{2}\sigma_k^z} \sigma_k^+ \, e^{-i\omega_p t \frac{1}{2}\sigma_k^z} = \sigma_k^+ + \frac{i\omega_p t}{2}[\sigma_k^z, \sigma_k^+] + \frac{1}{2!}\left(\frac{i\omega_p t}{2}\right)^2 [\sigma_k^z, [\sigma_k^z, \sigma_k^+]] + \ldots$$

$$= \sigma_k^+ \sum_{n=0}^{\infty} \frac{1}{n!}(i\omega_p t)^n = \sigma_k^+ e^{i\omega_p t}, \tag{A.6}$$

$$e^{i\omega_p t a^\dagger a} \, a \, e^{-i\omega_p t a^\dagger a} = a + i\omega_p t[a^\dagger a, a] + \frac{1}{2!}(i\omega_p t)^2 [a^\dagger a, [a^\dagger a, a]] + \ldots$$

$$= a \sum_{n=0}^{\infty} \frac{1}{n!}(-i\omega_p t)^n = ae^{-i\omega_p t}, \tag{A.7}$$

and

$$e^{i\omega_p t a^\dagger a} \, a^\dagger \, e^{-i\omega_p t a^\dagger a} = a^\dagger + i\omega_p t[a^\dagger a, a^\dagger] + \frac{1}{2!}(i\omega_p t)^2 [a^\dagger a, [a^\dagger a, a^\dagger]] + \ldots$$

$$= a^\dagger \sum_{n=0}^{\infty} \frac{1}{n!}(i\omega_p t)^n = a^\dagger e^{i\omega_p t}. \tag{A.8}$$

Using Eqs.(A.5)-(A.8), the Tavis-Cummings Hamiltonian in the rotating frame finally reads

$$\tilde{H} = \Delta_c \, a^\dagger a + \frac{1}{2}\sum_{k=1}^{N} \Delta_k \sigma_k^z + \sum_{k=1}^{N} g_k[\sigma_k^- a^\dagger + \sigma_k^+ a] + i\eta(t)[a^\dagger - a]. \tag{A.9}$$

B. Equations of motion for expectation values[12]

Following the procedure outlined in Section 1.2, it is straightforward to derive the hierarchic set of equations of motion for expectation values. For completeness, we show the equations of motion up to the third order explicitly.

First-order expectation values:

$$\frac{d}{dt}\langle a \rangle = -(\kappa + i\,\Delta_c)\,\langle a \rangle - i\sum_{k=1}^{N} g_k \,\langle \sigma_k^- \rangle + \eta \tag{B.1}$$

$$\frac{d}{dt}\langle \sigma_k^- \rangle = -(\gamma_h + 2\gamma_p + i\,\Delta_k)\,\langle \sigma_k^- \rangle + i\,g_k \,\langle \sigma_k^z a \rangle \tag{B.2}$$

$$\frac{d}{dt}\langle \sigma_k^z \rangle = -2\gamma_h(\langle \sigma_k^z \rangle + 1) + 2i\,g_k(\,\langle \sigma_k^- a^\dagger \rangle - \langle \sigma_k^- a^\dagger \rangle^*) \tag{B.3}$$

---

[12] The complete set of equations of motion for expectation values up to third order have already been presented in my diploma thesis [130] and are shown here for the sake of completeness.

Second-order expectation values:

$$\frac{d}{dt}\left\langle\sigma_k^z a\right\rangle = -\left(\kappa + 2\gamma_h + i\,\Delta_c\right)\left\langle\sigma_k^z a\right\rangle - 2\gamma_h\left\langle a\right\rangle + \eta\left\langle\sigma_k^z\right\rangle - i\sum_{\substack{j=1\\j\neq k}}^{N} g_j\left\langle\sigma_k^z\sigma_j^-\right\rangle + ig_k\left\langle\sigma_k^-\right\rangle$$
$$+ 2i\,g_k\left(\left\langle\sigma_k^- a^\dagger a\right\rangle - \left\langle\sigma_k^- a^\dagger a^\dagger\right\rangle^*\right) \tag{B.4}$$

$$\frac{d}{dt}\left\langle\sigma_k^z\sigma_j^-\right\rangle \underset{j\neq k}{=} -\left(3\gamma_h + 2\gamma_p + i\,\Delta_j\right)\left\langle\sigma_k^z\sigma_j^-\right\rangle - 2\gamma_h\left\langle\sigma_j^-\right\rangle + i\,g_j\left\langle\sigma_k^z\sigma_j^z a\right\rangle$$
$$+ 2i\,g_k\left(\left\langle\sigma_k^-\sigma_j^- a^\dagger\right\rangle - \left\langle\sigma_k^+\sigma_j^- a\right\rangle\right) \tag{B.5}$$

$$\frac{d}{dt}\left\langle\sigma_k^- a^\dagger\right\rangle = -\left(\kappa + \gamma_h + 2\gamma_p + i\left(\Delta_k - \Delta_c\right)\right)\left\langle\sigma_k^- a^\dagger\right\rangle + \eta\left\langle\sigma_k^-\right\rangle + i\sum_{\substack{j=1\\j\neq k}}^{N} g_j\left\langle\sigma_j^+\sigma_k^-\right\rangle$$
$$+ i\,\frac{g_k}{2}\left(\left\langle\sigma_k^z\right\rangle + 1\right) + i\,g_k\left\langle\sigma_k^z a^\dagger a\right\rangle \tag{B.6}$$

$$\frac{d}{dt}\left\langle\sigma_k^+\sigma_j^-\right\rangle \underset{j\neq k}{=} -\left(2\gamma_h + 4\gamma_p + i\left(\Delta_j - \Delta_k\right)\right)\left\langle\sigma_k^+\sigma_j^-\right\rangle - i\,g_k\left\langle\sigma_k^z\sigma_j^- a^\dagger\right\rangle + i\,g_j\left\langle\sigma_j^z\sigma_k^- a^\dagger\right\rangle^* \tag{B.7}$$

$$\frac{d}{dt}\left\langle\sigma_k^- a\right\rangle = -\left(\kappa + \gamma_h + 2\gamma_p + i\left(\Delta_k + \Delta_c\right)\right)\left\langle\sigma_k^- a\right\rangle + \eta\left\langle\sigma_k^-\right\rangle - i\sum_{\substack{j=1\\j\neq k}}^{N} g_j\left\langle\sigma_k^-\sigma_j^-\right\rangle + i\,g_k\left\langle\sigma_k^z aa\right\rangle \tag{B.8}$$

$$\frac{d}{dt}\left\langle a^\dagger a^\dagger\right\rangle = -2\left(\kappa - i\,\Delta_c\right)\left\langle a^\dagger a^\dagger\right\rangle + 2i\sum_{k=1}^{N} g_k\left\langle\sigma_k^- a\right\rangle^* + 2\eta\left\langle a\right\rangle^* \tag{B.9}$$

$$\frac{d}{dt}\left\langle a^\dagger a\right\rangle = -2\kappa\left\langle a^\dagger a\right\rangle - i\sum_{k=1}^{N} g_k\left(\left\langle\sigma_k^- a^\dagger\right\rangle - \left\langle\sigma_k^- a^\dagger\right\rangle^*\right) + \eta\left(\left\langle a\right\rangle + \left\langle a\right\rangle^*\right) \tag{B.10}$$

$$\frac{d}{dt}\left\langle\sigma_k^z\sigma_j^z\right\rangle \underset{j\neq k}{=} -2\gamma_h\left(\left\langle\sigma_k^z\right\rangle + \left\langle\sigma_k^z\sigma_j^z\right\rangle + \left\langle\sigma_j^z\right\rangle + \left\langle\sigma_j^z\sigma_k^z\right\rangle\right) + 2i\,g_k\left(\left\langle\sigma_j^z\sigma_k^- a^\dagger\right\rangle - \left\langle\sigma_j^z\sigma_k^- a^\dagger\right\rangle^*\right)$$
$$+ 2i\,g_j\left(\left\langle\sigma_k^z\sigma_j^- a^\dagger\right\rangle - \left\langle\sigma_k^z\sigma_j^- a^\dagger\right\rangle^*\right) \tag{B.11}$$

$$\frac{d}{dt}\left\langle\sigma_k^-\sigma_j^-\right\rangle \underset{j\neq k}{=} -\left(2\gamma_h + 4\gamma_p + i\left(\Delta_j + \Delta_k\right)\right)\left\langle\sigma_k^-\sigma_j^-\right\rangle + i\,g_k\left\langle\sigma_k^z\sigma_j^- a\right\rangle + i\,g_j\left\langle\sigma_j^z\sigma_k^- a\right\rangle \tag{B.12}$$

Third-order expectation values:

$$\frac{d}{dt}\left\langle\sigma_k^z a^\dagger a\right\rangle = -2\left(\kappa + \gamma_h\right)\left\langle\sigma_k^z a^\dagger a\right\rangle - 2\gamma_h\left\langle a^\dagger a\right\rangle + \eta\left(\left\langle\sigma_k^z a\right\rangle + \left\langle\sigma_k^z a\right\rangle^*\right)$$
$$- i\sum_{\substack{j=1\\j\neq k}}^{N} g_j\left(\left\langle\sigma_k^z\sigma_j^- a^\dagger\right\rangle - \left\langle\sigma_k^z\sigma_j^- a^\dagger\right\rangle^*\right) + i\,g_k\left(\left\langle\sigma_k^- a^\dagger\right\rangle - \left\langle\sigma_k^- a^\dagger\right\rangle^*\right)$$
$$+ 2i\,g_k\left(\left\langle\sigma_k^- a^\dagger a^\dagger a\right\rangle - \left\langle\sigma_k^- a^\dagger a^\dagger a\right\rangle^*\right) \tag{B.13}$$

$$\frac{d}{dt}\left\langle \sigma_k^- a^\dagger a \right\rangle = -\left(2(\kappa + \gamma_p) + \gamma_h + i\Delta_k\right)\left\langle \sigma_k^- a^\dagger a \right\rangle + \eta(\left\langle \sigma_k^- a^\dagger \right\rangle + \left\langle \sigma_k^- a \right\rangle) + i\,g_k\left\langle \sigma_k^z a^\dagger a a \right\rangle$$

$$+ i\sum_{\substack{j=1\\j\neq k}}^{N} g_j(\left\langle \sigma_j^+ \sigma_k^- a \right\rangle - \left\langle \sigma_k^- \sigma_j^- a^\dagger \right\rangle) + i\,\frac{g_k}{2}(\left\langle \sigma_k^z a \right\rangle + \left\langle a \right\rangle) \tag{B.14}$$

$$\frac{d}{dt}\left\langle \sigma_k^- a^\dagger a^\dagger \right\rangle = -\left(2(\kappa + \gamma_p) + \gamma_h + i(\Delta_k - 2\Delta_c)\right)\left\langle \sigma_k^- a^\dagger a^\dagger \right\rangle + 2\eta\left\langle \sigma_k^- a^\dagger \right\rangle + 2i\sum_{\substack{j=1\\j\neq k}}^{N} g_j\left\langle \sigma_j^+ \sigma_k^- a^\dagger \right\rangle$$

$$+ i\,g_k(\left\langle \sigma_k^z a \right\rangle^* + \left\langle a \right\rangle^*) + i\,g_k\left\langle \sigma_k^z a^\dagger a^\dagger a \right\rangle \tag{B.15}$$

$$\frac{d}{dt}\left\langle \sigma_k^z a a \right\rangle = -2(\kappa + \gamma_h + i\Delta_c)\left\langle \sigma_k^z a a \right\rangle - 2\gamma_h\left\langle a^\dagger a^\dagger \right\rangle^* + 2\eta\left\langle \sigma_k^z a \right\rangle + 2i\,g_k\left\langle \sigma_k^- a \right\rangle - 2i\sum_{\substack{j=1\\j\neq k}}^{N} g_j\left\langle \sigma_k^z \sigma_j^- a \right\rangle$$

$$+ 2i\,g_k(\left\langle \sigma_k^- a^\dagger a a \right\rangle - \left\langle \sigma_k^+ a a a \right\rangle) \tag{B.16}$$

$$\frac{d}{dt}\left\langle \sigma_k^- a a \right\rangle = -\left(2(\kappa + \gamma_p) + \gamma_h + i(\Delta_k + 2\Delta_c)\right)\left\langle \sigma_k^- a a \right\rangle + 2\eta\left\langle \sigma_k^- a \right\rangle - 2i\sum_{\substack{j=1\\j\neq k}}^{N} g_j\left\langle \sigma_k^- \sigma_j^- a \right\rangle$$

$$+ i\,g_k\left\langle \sigma_k^z a a a \right\rangle \tag{B.17}$$

$$\frac{d}{dt}\left\langle a^\dagger a a \right\rangle = -(3\kappa + i\,\Delta_c)\left\langle a^\dagger a a \right\rangle - 2i\sum_{k=1}^{N} g_k\left\langle \sigma_k^- a^\dagger a \right\rangle + i\sum_{k=1}^{N} g_k\left\langle \sigma_k^- a^\dagger a^\dagger \right\rangle^* + 2\eta\left\langle a^\dagger a \right\rangle + \eta\left\langle a^\dagger a^\dagger \right\rangle^*$$

$$\tag{B.18}$$

$$\frac{d}{dt}\left\langle a a a \right\rangle = -3(\kappa + i\,\Delta_c)\left\langle a a a \right\rangle - 3i\sum_{k=1}^{N} g_k\left\langle \sigma_k^- a a \right\rangle + 3\eta\left\langle a^\dagger a^\dagger \right\rangle^* \tag{B.19}$$

$$\frac{d}{dt}\left\langle \sigma_k^z \sigma_j^z a \right\rangle \underset{j\neq k}{=} -(\kappa + i\Delta_c)\left\langle \sigma_k^z \sigma_j^z a \right\rangle - 2\gamma_h(\left\langle \sigma_k^z a \right\rangle + \left\langle \sigma_k^z \sigma_j^z a \right\rangle + \left\langle \sigma_j^z a \right\rangle + \left\langle \sigma_j^z \sigma_k^z a \right\rangle) + 2i(g_k\left\langle \sigma_j^z \sigma_k^- a^\dagger a \right\rangle$$

$$+ g_j\left\langle \sigma_k^z \sigma_j^- a^\dagger a \right\rangle - g_k\left\langle \sigma_j^z \sigma_k^+ a a \right\rangle - g_j\left\langle \sigma_k^z \sigma_j^+ a a \right\rangle) - i\sum_{\substack{m=1\\m\neq k,j}}^{N} g_m\left\langle \sigma_k^z \sigma_j^z \sigma_m^- \right\rangle$$

$$+ i\,g_k\left\langle \sigma_j^z \sigma_k^- \right\rangle + i\,g_j\left\langle \sigma_k^z \sigma_j^- \right\rangle \tag{B.20}$$

$$\frac{d}{dt}\left\langle \sigma_k^- \sigma_j^- a^\dagger \right\rangle \underset{j\neq k}{=} -\left(\kappa + 2\gamma_h + 4\gamma_p + i(\Delta_k + \Delta_j - \Delta_c)\right)\left\langle \sigma_k^- \sigma_j^- a^\dagger \right\rangle + \eta\left\langle \sigma_k^- \sigma_j^- \right\rangle$$

$$+ i\sum_{\substack{m=1\\m\neq k,j}}^{N} g_m\left\langle \sigma_m^+ \sigma_k^- \sigma_j^- \right\rangle + i\frac{g_k}{2}(\left\langle \sigma_j^- \right\rangle + \left\langle \sigma_k^z \sigma_j^- \right\rangle) + i\frac{g_j}{2}(\left\langle \sigma_k^- \right\rangle + \left\langle \sigma_j^z \sigma_k^- \right\rangle)$$

$$+ i\,g_k\left\langle \sigma_k^z \sigma_j^- a^\dagger a \right\rangle + i\,g_j\left\langle \sigma_j^z \sigma_k^- a^\dagger a \right\rangle \tag{B.21}$$

$$\frac{d}{dt}\left\langle \sigma_k^+ \sigma_j^- a \right\rangle \underset{j\neq k}{=} -\left(\kappa + 2\gamma_h + 4\gamma_p + i(\Delta_j - \Delta_k + \Delta_c)\right)\left\langle \sigma_k^+ \sigma_j^- a \right\rangle + \eta\left\langle \sigma_k^+ \sigma_j^- \right\rangle$$

$$- i\sum_{\substack{m=1\\m\neq k,j}}^{N} g_m\left\langle \sigma_k^+ \sigma_j^- \sigma_m^- \right\rangle - i\frac{g_k}{2}(\left\langle \sigma_j^- \right\rangle + \left\langle \sigma_k^z \sigma_j^- \right\rangle) - i\,g_k\left\langle \sigma_k^z \sigma_j^- a^\dagger a \right\rangle + i\,g_j\left\langle \sigma_k^+ \sigma_j^z a a \right\rangle$$

$$\tag{B.22}$$

$$\frac{d}{dt}\langle\sigma_k^z\sigma_j^-a^\dagger\rangle \underset{j\neq k}{=} -(\kappa+3\gamma_h+2\gamma_p+i(\Delta_j-\Delta_c))\langle\sigma_k^z\sigma_j^-a^\dagger\rangle - 2\gamma_h\langle\sigma_j^-a^\dagger\rangle + \eta\langle\sigma_k^z\sigma_j^-\rangle$$

$$+ i\sum_{\substack{m=1\\m\neq k,j}}^N g_m\langle\sigma_m^+\sigma_k^z\sigma_j^-\rangle - i\,g_k\langle\sigma_k^+\sigma_j^-\rangle + i\,\frac{g_j}{2}(\langle\sigma_k^z\rangle + \langle\sigma_k^z\sigma_k^z\rangle) + i\,g_j\langle\sigma_k^z\sigma_j^za^\dagger a\rangle$$

$$+ 2i\,g_k(\langle\sigma_k^-\sigma_j^-a^\dagger a^\dagger\rangle - \langle\sigma_k^+\sigma_j^-a^\dagger a\rangle) \tag{B.23}$$

$$\frac{d}{dt}\langle\sigma_k^z\sigma_j^-a\rangle \underset{j\neq k}{=} -(\kappa+3\gamma_h+2\gamma_p+i(\Delta_j+\Delta_c))\langle\sigma_k^z\sigma_j^-a\rangle - 2\gamma_h\langle\sigma_j^-a\rangle + \eta\langle\sigma_k^z\sigma_j^-\rangle$$

$$- i\sum_{\substack{m=1\\m\neq k,j}}^N g_m\langle\sigma_k^z\sigma_j^-\sigma_m^-\rangle + i\,g_k\langle\sigma_k^-\sigma_j^-\rangle + i\,g_j\langle\sigma_k^z\sigma_j^zaa\rangle$$

$$+ 2i\,g_k(\langle\sigma_k^-\sigma_j^-a^\dagger a\rangle - \langle\sigma_k^+\sigma_j^-aa\rangle) \tag{B.24}$$

$$\frac{d}{dt}\langle\sigma_k^-\sigma_j^-a\rangle \underset{j\neq k}{=} -(\kappa+2\gamma_h+4\gamma_p+i(\Delta_k+\Delta_j+\Delta_c))\langle\sigma_k^-\sigma_j^-a\rangle + \eta\langle\sigma_k^-\sigma_j^-\rangle$$

$$- i\sum_{\substack{m=1\\m\neq k,j}}^N g_m\langle\sigma_k^-\sigma_j^-\sigma_m^-\rangle + i\,g_k\langle\sigma_k^z\sigma_j^-aa\rangle + i\,g_j\langle\sigma_j^z\sigma_k^-aa\rangle \tag{B.25}$$

C. Inhomogeneous broadening

The assumption of a homogeneous spin ensemble has the advantage of allowing simple analytical solutions, which often enable valuable insights into the phenomenon at hand, but the disadvantage of being utterly unrealistic for most experimental realizations. In this appendix, we demonstrate how the inhomogeneous broadening can be implemented in the Maxwell-Bloch equations of Section 2.2 and the cumulant expansion method of Section 3.1.

In Section 2.1, we introduced the continuous spectral spin distribution $\rho(\omega) \equiv \sum_{k=1}^N g_k^2\delta(\omega-\omega_k)/\Omega^2$, where Ω is the collective coupling strength of the spin ensemble. This spectral spin distribution, which is determined from transmission measurements in the weak excitation regime [36], is a combined distribution of both, the coupling strengths g_k and the spin frequencies ω_k. While in the linear regime, the knowledge of this combined spin spectral density is sufficient to precisely describe the dynamics of the spin-cavity system [38], the situation becomes more complicated in the nonlinear regime. Here, the individual distributions of coupling strengths and spins become relevant, and, in case these are unknown, additional assumptions have to be made.

First, we divide the spin ensemble into L equally sized frequency intervals $\delta\omega$ with $L \ll N$ to make the problem numerically tractable. We assume that the frequency clusters, which we label with the greek index μ, consist of M_μ spins

with similar transition frequencies ω_μ and coupling strengths g_μ. This dramatically reduces the number of equations that need to be solved in the Maxwell-Bloch equations [Section 2.2] and the cumulant expansion method [Section 3.1]. Notably, the number of clusters has to be chosen such that the spectral spin distribution can be properly represented, and the reciprocal frequency spacing of adjacent clusters $1/|\omega_\mu - \omega_{\mu+1}|$ is larger than the covered time of the system's evolution. The latter condition ensures that there are no artifacts in the simulation due to the frequency discretization. In this thesis, for practical purposes, we consider two simplified scenarios: (i) inhomogeneous coupling g_μ and (ii) inhomogeneous cluster sizes M_μ.

Inhomogeneous coupling. We assume that g_μ effectively respresents the coupling strength of a "large" spin residing in the μ-th spin cluster with frequency $\omega_\mu + \delta\omega$ rather than an individual coupling strength. The coupling strengths g_μ are then determined from the spectral spin density $\rho(\omega)$ by the inverse transformation, $g_\mu = \Omega[\rho(\omega_\mu)/\sum_{\nu=1}^{L} \rho(\omega_\nu)]^{1/2}$.

Inhomogeneous cluster size. Instead of an inhomogeneous coupling distribution, we assume here, that each frequency cluster is occupied by a different number of spins M_μ. Here, the distribution of spins follows the spectral spin density $M_\mu = \rho(\omega_\mu)/\sum_{\nu=1}^{L} \rho(\omega_\nu)$, while we assume that the individual spins all couple with the same coupling strength $g_k = g_0 = \Omega/\sqrt{N}$.

D. Calculation of the stationary states

In order to solve for the stationary states of a macroscopic spin ensemble, we start from the semiclassical Maxwell-Bloch equations (2.20a)-(2.20c) and set all time derivatives to zero. Equation (2.20b) then results in

$$\langle\sigma_{k,st}^-\rangle = i\,g_k \frac{\langle\sigma_{k,st}^z\rangle\,\langle a_{st}\rangle}{\gamma_\perp + i\,\Delta_k}, \tag{D.1}$$

which inserted into Eq. (2.20c) gives

$$\langle\sigma_{k,st}^z\rangle = -\frac{1}{1 + |\langle a_{st}\rangle|^2 \frac{4g_k^2}{\gamma_\perp\gamma_\parallel(1+\Delta_k^2/\gamma_\perp^2)}} = -\frac{1}{1 + |\langle a_{st}\rangle|^2/n_k}. \tag{D.2}$$

Substituting the equations (D.1) and (D.2) into Eq.(2.20a) yields

$$\eta = \langle a_{st}\rangle \left(\kappa + i\Delta_c + \sum_k \frac{g_k^2}{1 + |\langle a_{st}\rangle|^2/n_k} \frac{\gamma_\perp - i\Delta_k}{\gamma_\perp^2 + \Delta_k^2} \right). \tag{D.3}$$

Since we only deal with resonant driving, we can set $\Delta_c = 0$. Furthermore, we focus on spin distributions which are symmetric with respect to their central frequency ω_s and resonant with the cavity frequency $\omega_s = \omega_c$. As a result, the imaginary part in Eq. (D.3) vanishes after summation, and we arrive at

$$\eta = \langle a_{st} \rangle \left(\kappa + \sum_k \frac{g_k^2}{1 + |\langle a_{st} \rangle|^2 / n_k} \frac{\gamma_\perp}{\gamma_\perp^2 + \Delta_k^2} \right). \tag{D.4}$$

Finally, dividing Eq. (D.4) by κ and using the definition of the cooperativity parameter $C_k \equiv g_k^2 (\gamma_\perp \kappa (1 + \Delta_k^2/\gamma_\perp^2))^{-1}$ [Eq. (4.2)] gives the steady-state equation (4.1) for the cavity amplitude

$$\frac{\eta}{\kappa} = \langle a_{st} \rangle \left(1 + \sum_k \frac{C_k}{1 + |\langle a_{st} \rangle|^2 / n_k} \right). \tag{D.5}$$

E. Adiabatic elimination

Adiabatic elimination is a universal concept of fundamental importance in the study of complex and nonlinear dynamical systems [251]. It allows one to reduce the number of equations that govern the system's evolution by identifying fast variables with large relaxation rates and slow variables, which display small relaxation rates. The temporal evolution is thereby divided into two distinct stages: a first fast time scale, in which the fast variables relax to a state determined by the instant values of the slow variables, and a second stage governed solely by the evolution of the slow variables, which are adiabatically followed by the fast variables.

We observe such a separation of time scales in Section 4.2, where we study the time evolution of an inhomogeneously broadened solid-state spin ensemble strongly coupled to a microwave cavity. Here, the longitudinal relaxation rate of the spins, $\gamma_\parallel$, is much smaller than all other relaxation rates within the system $\gamma_\parallel \ll \kappa, \gamma_\perp$. In Section 4.2, we use this property to eliminate the fast variables $\langle a \rangle$ and $\langle \sigma_k^- \rangle$ obtaining a single equations for $\langle \sigma_k^z \rangle$, which determines the evolution of the whole spin-cavity system at large time scales.

Introducing the dimensionless time $\tau = \gamma_\parallel t$, the Maxwell-Bloch equations can be rewritten as

$$\frac{\gamma_\parallel}{\kappa} \frac{d}{d\tau} \langle a \rangle = -(1 + i\frac{\Delta_c}{\kappa}) \langle a \rangle - \frac{i}{\kappa} \sum_{k=1}^{N} g_k \langle \sigma_k^- \rangle + \frac{\eta}{\kappa} \tag{E.1}$$

$$\frac{\gamma_\parallel}{\gamma_\perp} \frac{d}{d\tau} \langle \sigma_k^- \rangle = -(1 + i\frac{\Delta_k}{\gamma_\perp}) \langle \sigma_k^- \rangle + i \frac{g_k}{\gamma_\perp} \langle \sigma_k^z \rangle \langle a \rangle \tag{E.2}$$

$$\frac{d}{d\tau} \langle \sigma_k^z \rangle = -(\langle \sigma_k^z \rangle + 1) - 4 \frac{g_k}{\gamma_\parallel} \text{Im}(\langle \sigma_k^- \rangle \langle a^\dagger \rangle). \tag{E.3}$$

From $\gamma_\parallel/\kappa \ll 1$ and $\gamma_\parallel/\gamma_\perp \ll 1$, we infer that the time derivatives $d\langle a \rangle/d\tau$ and $d\langle \sigma_k^- \rangle/d\tau$ give only vanishing contributions at large times compared to the right-hand side of Eqs. (E.1)-(E.2). Setting these time derivatives to zero, we obtain an algebraic set of equations determining a functional dependence of the fast variables $\langle a \rangle$ and $\langle \sigma_k^- \rangle$ on the slow variables $\langle \sigma_k^z \rangle$ given by

$$\langle \sigma_k^- \rangle = ig_k \frac{\langle a \rangle \langle \sigma_k^z \rangle}{\gamma_\perp(1 + i\Delta_k/\gamma_\perp)} \tag{E.4}$$

and

$$\langle a \rangle = \frac{\eta}{\kappa(1 - \sum_{k=1}^N C_k \langle \sigma_k^z \rangle)}. \tag{E.5}$$

Similarly to Appendix D, here we have assumed a symmetric spin distribution ($\sum_{k=1}^N \Delta_k = 0$), resonant driving ($\Delta_c = 0$), and used the definition of the cooperativity parameter $C_k \equiv g_k^2(\gamma_\perp \kappa(1 + \Delta_k^2/\gamma_\perp^2))^{-1}$ [Eq. (4.2)].

Inserting Eqs. (E.4) and (E.5) into the dynamic equation for the variables $\langle \sigma_k^z \rangle$, Eq. (E.3) yields

$$\frac{d}{d\tau}\langle \sigma_k^z \rangle = -(1 + \langle \sigma_k^z \rangle) - \frac{\eta^2}{\kappa^2} \frac{4g_k^2}{\gamma_\parallel \gamma_\perp(1 + \Delta_k^2/\gamma_\perp^2)} \frac{\langle \sigma_k^z \rangle}{(1 - \sum_{l=1}^N C_l \langle \sigma_l^z \rangle)^2}$$

$$= -(1 + \langle \sigma_k^z \rangle) - \frac{\eta^2}{\kappa^2} \frac{\langle \sigma_k^z \rangle}{n_k(1 - \sum_l C_l \langle \sigma_l^z \rangle)^2}, \tag{E.6}$$

with $n_k \equiv \frac{\gamma_\perp \gamma_\parallel}{4g_k^2}(1 + \Delta_k^2/\gamma_\perp^2)$ being the photon saturation number [Eq. (4.3)]. As a result of the adiabatic elimination, the single Eq. (E.6) for the slow variables $\langle \sigma_k^z \rangle$ fully determines the evolution of the spin-cavity system on long time scales.

F. Laplace transformation

In this Appendix, we present a formal solution to the Volterra equation (2.13) using the standard Laplace transform method [252] closely following refs. [38, 212] and the Supplementary Note 3 of ref. [84]. Here we assume initial conditions with a single photon inside the cavity ($A(0) = 1$) and all spins in their ground state ($B_k(0) = 0$). Furthermore, we assume that the cavity is on resonance ($\Delta_c = 0$) and that there is no external driving ($\eta = 0$).

Starting from Eq. (2.7), we perform the transformation $\tilde{A}(t) \equiv e^{\gamma_\perp t}A(t)$ giving the following integro-differential equation

$$\frac{d}{dt}\tilde{A}(t) = -\xi\tilde{A}(t) - \Omega^2 \int_0^\infty d\omega \rho(\omega) \int_0^t d\tau e^{-i(\omega-\omega_c)(t-\tau)}\tilde{A}(\tau), \tag{F.1}$$

where we introduced the shorthand notation $\xi \equiv \kappa - \gamma_\perp$. The Laplace transformation of $\tilde{A}(t)$ is given by

$$\mathcal{A}(s) \equiv \int_0^\infty e^{-st} \tilde{A}(t), \tag{F.2}$$

with $s \equiv \sigma + i\bar{\omega}$ being a complex variable. Multiplying Eq. (F.1) by e^{-st} and integrating both sides with respect to time gives

$$\int_0^\infty dt e^{-st} \frac{d}{dt} \tilde{A}(t) = -\xi \int_0^\infty dt e^{-st} \tilde{A}(t) - \Omega^2 \int_0^\infty d\omega \rho(\omega) \int_0^\infty dt e^{-st} \int_0^t d\tau e^{-i(\omega-\omega_c)(t-\tau)} \tilde{A}(\tau), \tag{F.3}$$

which can be simplified to

$$-\tilde{A}(0) + s\mathcal{A}(s) = -\xi \mathcal{A}(s) - \Omega^2 \int_0^\infty d\omega \rho(\omega) \int_0^\infty dt e^{-st} \int_0^t d\tau e^{-i(\omega-\omega_c)(t-\tau)} \tilde{A}(\tau). \tag{F.4}$$

The time integral in the second term of the right side of Eq. (F.4) can be solved through integration by parts,

$$\int_0^\infty dt e^{-st} \int_0^t d\tau e^{-i\alpha(t-\tau)} \tilde{A}(\tau) = \int_0^\infty dt e^{-(s+i\alpha)t} \int_0^t d\tau e^{i\alpha\tau} \tilde{A}(\tau)$$

$$= -\frac{1}{s+i\alpha} \left[\underbrace{e^{-(s+i\alpha)t} \int_0^t d\tau e^{-i\alpha\tau} \tilde{A}(\tau) \Big|_0^\infty}_{=0} - \int_0^\infty dt e^{-(s+i\alpha)t} e^{-i\alpha t} \tilde{A}(t) \right]$$

$$= \frac{1}{s+i\alpha} \int_0^\infty dt\, e^{-st} \tilde{A}(t) = \frac{\mathcal{A}(s)}{s+i\alpha}, \tag{F.5}$$

where the boundary term vanishes for $\mathrm{Re}(s) > 0$. Using Eq. (F.5) and the initial condition $\tilde{A}(0) = 1$, we arrive at an algebraic equation for the Laplace transform giving

$$\mathcal{A}(s) = \frac{1}{s + \xi + \Omega^2 \int_0^\infty d\omega \rho(\omega) \frac{1}{s+i(\omega-\omega_c)}}. \tag{F.6}$$
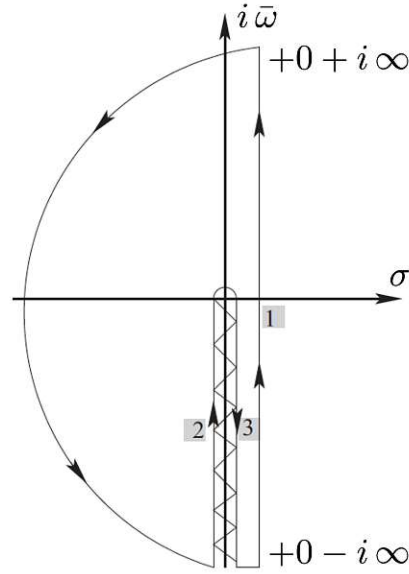
By performing the inverse Laplace transformation

$$\tilde{A}(t) = \frac{1}{2\pi i} \int_{\sigma-i\infty}^{\sigma+i\infty} ds\, e^{st} \mathcal{A}(s), \tag{F.7}$$

we obtain a formal solution for the amplitude $A(t)$ given by

$$A(t) = \frac{1}{2\pi i} e^{(-\gamma_\perp + i\omega_c)t} \int_{\sigma-i\infty}^{\sigma+i\infty} d\tilde{s} \frac{e^{\tilde{s}t}}{\tilde{s} + i\omega_c + \xi + \Omega^2 \int_0^\infty d\omega \rho(\omega) \frac{1}{\tilde{s}+i\omega}}, \tag{F.8}$$

where we have substituted $\tilde{s} \equiv s - i\omega_c$. Furthermore, $\sigma > 0$ is chosen such that the real parts of all singularities of $\mathcal{A}(s)$ are smaller than σ. It can be shown that

Figure F.1.: Contour completion in the complex plane $s = \sigma + i\,\bar{\omega}$ for the calculation of the inverse Laplace transform [Eq. (F.8)]. Those paths which give nonzero contribution are designated by numbers. The zig-zag line corresponds to the branch cut along the negative part of the imaginary axis. Figure adapted from Supplementary Note 3 of ref. [84].

the integrand in Eq. (F.8) exhibits a jump along the negative part of the imaginary axis [212], which is a branch cut. By equating the denominator of the integrand in Eq. (F.8) to zero, one can derive equations for the simple poles, $\tilde{s}_j = \sigma_j + i\,\bar{\omega}_j$.

To evaluate the integral Eq. (F.8), we apply Cauchy's theorem to the closed contour depicted in Fig. F.1. Taking into account that only a few paths contribute, we finally end up with the following expression for the cavity amplitude

$$A(t) = \Omega^2 \int_0^\infty e^{-i(\omega - \omega_c - i\gamma_\perp)t}\, U(\omega)\, d\omega, \tag{F.9}$$

where

$$U(\omega) = \lim_{\sigma \to 0^+} \left\{ \frac{\rho(\omega)}{\left(\omega - \omega_c - \Omega^2 \delta(\omega) + i(\kappa - \gamma_\perp)\right)^2 + \left(\pi\Omega^2\rho(\omega) + \sigma\right)^2} \right\} \tag{F.10}$$

is the kernel function and

$$\delta(\omega) = \mathcal{P} \int_0^\infty \frac{d\tilde{\omega}\rho(\tilde{\omega})}{\omega - \tilde{\omega}} \tag{F.11}$$

denotes the nonlinear Lamb shift of the cavity frequency ω_c.

Bibliography

[1] E. M. Purcell. "Spontaneous Emission Probabilities at Radio Frequencies". *Physical Review* 69, p. 681 (1946).

[2] K. H. Drexhage. "IV Interaction of Light with Monomolecular Dye Layers". In: *Progress in Optics*. Vol. 12. Elsevier, 1974, pp. 163–232.

[3] P. Goy, J. M. Raimond, M. Gross, and S. Haroche. "Observation of Cavity-Enhanced Single-Atom Spontaneous Emission". *Physical Review Letters* 50, pp. 1903–1906 (1983).

[4] R. G. Hulet, E. S. Hilfer, and D. Kleppner. "Inhibited Spontaneous Emission by a Rydberg Atom". *Physical Review Letters* 55, pp. 2137–2140 (1985).

[5] G. Gabrielse and H. Dehmelt. "Observation of inhibited spontaneous emission". *Physical Review Letters* 55, pp. 67–70 (1985).

[6] E. Jaynes and F. Cummings. "Comparison of quantum and semiclassical radiation theories with application to the beam maser". *Proceedings of the IEEE* 51, pp. 89–109 (1963).

[7] B. W. Shore and P. L. Knight. "The Jaynes-Cummings Model". *Journal of Modern Optics* 40, pp. 1195–1238 (1993).

[8] B. Odom, D. Hanneke, B. D'Urso, and G. Gabrielse. "New Measurement of the Electron Magnetic Moment Using a One-Electron Quantum Cyclotron". *Physical Review Letters* 97, p. 030801 (2006).

[9] P. Bertet, S. Osnaghi, A. Rauschenbeutel, G. Nogues, A. Auffeves, M. Brune, J. M. Raimond, and S. Haroche. "A complementarity experiment with an interferometer at the quantum–classical boundary". *Nature* 411, pp. 166–170 (2001).

[10] S. Gleyzes, S. Kuhr, C. Guerlin, J. Bernu, S. Deléglise, U. Busk Hoff, M. Brune, J.-M. Raimond, and S. Haroche. "Quantum jumps of light recording the birth and death of a photon in a cavity". *Nature* 446, pp. 297–300 (2007).

[11] C. Guerlin, J. Bernu, S. Deléglise, C. Sayrin, S. Gleyzes, S. Kuhr, M. Brune, J.-M. Raimond, and S. Haroche. "Progressive field-state collapse and quantum non-demolition photon counting". *Nature* 448, pp. 889–893 (2007).

[12] S. Deléglise, I. Dotsenko, C. Sayrin, J. Bernu, M. Brune, J.-M. Raimond, and S. Haroche. "Reconstruction of non-classical cavity field states with snapshots of their decoherence". *Nature* 455, pp. 510–514 (2008).

[13] P. Michler, A. Kiraz, C. Becher, W. V. Schoenfeld, P. M. Petroff, L. Zhang, E. Hu, and A. Imamoglu. "A Quantum Dot Single-Photon Turnstile Device". *Science* 290, pp. 2282–2285 (2000).

[14] P. Ginzburg. "Cavity quantum electrodynamics in application to plasmonics and metamaterials". *Reviews in Physics* 1, pp. 120–139 (2016).

[15] S. Haroche, M. Brune, and J. M. Raimond. "From cavity to circuit quantum electrodynamics". *Nature Physics* 16, pp. 243–246 (2020).

[16] J. M. Raimond, M. Brune, and S. Haroche. "Manipulating quantum entanglement with atoms and photons in a cavity". *Reviews of Modern Physics* 73, pp. 565–582 (2001).

[17] A. Blais, R.-S. Huang, A. Wallraff, S. M. Girvin, and R. J. Schoelkopf. "Cavity quantum electrodynamics for superconducting electrical circuits: An architecture for quantum computation". *Physical Review A* 69, p. 062320 (2004).

[18] J.-M. Raimond and G. Rempe. "Cavity Quantum Electrodynamics: Quantum Information Processing with Atoms and Photons". In: *Quantum Information*. Ed. by D. Bruß and G. Leuchs. 1st ed. Wiley, Apr. 18, 2016, pp. 669–689.

[19] G. Kurizki, P. Bertet, Y. Kubo, K. Mølmer, D. Petrosyan, P. Rabl, and J. Schmiedmayer. "Quantum technologies with hybrid systems". *Proceedings of the National Academy of Sciences* 112, pp. 3866–3873 (2015).

[20] Z.-L. Xiang, S. Ashhab, J. Q. You, and F. Nori. "Hybrid quantum circuits: Superconducting circuits interacting with other quantum systems". *Reviews of Modern Physics* 85, pp. 623–653 (2013).

[21] T. E. Northup and R. Blatt. "Quantum information transfer using photons". *Nature Photonics* 8, pp. 356–363 (2014).

[22] J. J. Morton and P. Bertet. "Storing quantum information in spins and high-sensitivity ESR". *Journal of Magnetic Resonance* 287, pp. 128–139 (2018).

[23] H. Mabuchi. "Cavity Quantum Electrodynamics: Coherence in Context". *Science* 298, pp. 1372–1377 (2002).

[24] S. Haroche. "Controlling Photons in a Box and Exploring the Quantum to Classical Boundary (Nobel Lecture)". *Angewandte Chemie International Edition* 52, pp. 10158–10178 (2013).

[25] M. Brune, F. Schmidt-Kaler, A. Maali, J. Dreyer, E. Hagley, J. M. Raimond, and S. Haroche. "Quantum Rabi Oscillation: A Direct Test of Field Quantization in a Cavity". *Physical Review Letters* 76, pp. 1800–1803 (1996).

[26] H. J. Kimble. "Strong Interactions of Single Atoms and Photons in CavityQED". *Physica Scripta* T76, p. 127 (1998).

[27] R. J. Thompson, G. Rempe, and H. J. Kimble. "Observation of normal-mode splitting for an atom in an optical cavity". *Physical Review Letters* 68, pp. 1132–1135 (1992).

[28] R. Chikkaraddy, B. de Nijs, F. Benz, S. J. Barrow, O. A. Scherman, E. Rosta, A. Demetriadou, P. Fox, O. Hess, and J. J. Baumberg. "Single-molecule strong coupling at room temperature in plasmonic nanocavities". *Nature* 535, pp. 127–130 (2016).

[29] K. Santhosh, O. Bitton, L. Chuntonov, and G. Haran. "Vacuum Rabi splitting in a plasmonic cavity at the single quantum emitter limit". *Nature Communications* 7, ncomms11823 (2016).

[30] A. Wallraff, D. I. Schuster, A. Blais, L. Frunzio, R. S. Huang, J. Majer, S. Kumar, S. M. Girvin, and R. J. Schoelkopf. "Strong coupling of a single photon to a superconducting qubit using circuit quantum electrodynamics". *Nature* 431, pp. 162–167 (2004).

[31] J. M. Fink, M. Göppl, M. Baur, R. Bianchetti, P. J. Leek, A. Blais, and A. Wallraff. "Climbing the Jaynes–Cummings ladder and observing its nonlinearity in a cavity QED system". *Nature* 454, pp. 315–318 (2008).

[32] D. Najer, I. Söllner, P. Sekatski, V. Dolique, M. C. Löbl, D. Riedel, R. Schott, S. Starosielec, S. R. Valentin, A. D. Wieck, N. Sangouard, A. Ludwig, and R. J. Warburton. "A gated quantum dot strongly coupled to an optical microcavity". *Nature* 575, pp. 622–627 (2019).

[33] D. I. Schuster, A. P. Sears, E. Ginossar, L. DiCarlo, L. Frunzio, J. J. L. Morton, H. Wu, G. A. D. Briggs, B. B. Buckley, D. D. Awschalom, and R. J. Schoelkopf. "High-Cooperativity Coupling of Electron-Spin Ensembles to Superconducting Cavities". *Physical Review Letters* 105, p. 140501 (2010).

[34] Y. Kubo, F. R. Ong, P. Bertet, D. Vion, V. Jacques, D. Zheng, A. Dréau, J.-F. Roch, A. Auffeves, F. Jelezko, J. Wrachtrup, M. F. Barthe, P. Bergonzo, and D. Esteve. "Strong Coupling of a Spin Ensemble to a Superconducting Resonator". *Physical Review Letters* 105, p. 140502 (2010).

[35] R. Amsüss, C. Koller, T. Nöbauer, S. Putz, S. Rotter, K. Sandner, S. Schneider, M. Schramböck, G. Steinhauser, H. Ritsch, J. Schmiedmayer, and J. Majer. "Cavity QED with Magnetically Coupled Collective Spin States". *Physical Review Letters* 107, p. 060502 (2011).

[36] K. Sandner, H. Ritsch, R. Amsüss, C. Koller, T. Nöbauer, S. Putz, J. Schmiedmayer, and J. Majer. "Strong magnetic coupling of an inhomogeneous nitrogen-vacancy ensemble to a cavity". *Physical Review A* 85, p. 053806 (2012).

[37] S. Putz, D. O. Krimer, R. Amsüss, A. Valookaran, T. Nöbauer, J. Schmied-mayer, S. Rotter, and J. Majer. "Protecting a spin ensemble against deco-herence in the strong-coupling regime of cavity QED". *Nature Physics* 10, pp. 720–724 (2014).

[38] D. O. Krimer, S. Putz, J. Majer, and S. Rotter. "Non-Markovian dynamics of a single-mode cavity strongly coupled to an inhomogeneously broadened spin ensemble". *Physical Review A* 90, p. 043852 (2014).

[39] A. Angerer, S. Putz, D. O. Krimer, T. Astner, M. Zens, R. Glattauer, K. Streltsov, W. J. Munro, K. Nemoto, S. Rotter, J. Schmiedmayer, and J. Majer. "Ultralong relaxation times in bistable hybrid quantum systems". *Science Advances* 3, e1701626 (2017).

[40] C. W. Zollitsch, K. Mueller, D. P. Franke, S. T. B. Goennenwein, M. S. Brandt, R. Gross, and H. Huebl. "High cooperativity coupling between a phosphorus donor spin ensemble and a superconducting microwave res-onator". *Applied Physics Letters* 107, p. 142105 (2015).

[41] S. Weichselbaumer, M. Zens, C. W. Zollitsch, M. S. Brandt, S. Rotter, R. Gross, and H. Huebl. "Echo Trains in Pulsed Electron Spin Resonance of a Strongly Coupled Spin Ensemble". *Physical Review Letters* 125, p. 137701 (2020).

[42] S. Probst, H. Rotzinger, S. Wünsch, P. Jung, M. Jerger, M. Siegel, A. V. Ustinov, and P. A. Bushev. "Anisotropic Rare-Earth Spin Ensemble Strongly Coupled to a Superconducting Resonator". *Physical Review Letters* 110, p. 157001 (2013).

[43] P. Bushev, A. K. Feofanov, H. Rotzinger, I. Protopopov, J. H. Cole, C. M. Wilson, G. Fischer, A. Lukashenko, and A. V. Ustinov. "Ultralow-power spectroscopy of a rare-earth spin ensemble using a superconducting res-onator". *Physical Review B* 84, p. 060501 (2011).

[44] P. Goldner, A. Ferrier, and O. Guillot-Noël. "Rare Earth-Doped Crystals for Quantum Information Processing". In: *Handbook on the Physics and Chem-istry of Rare Earths*. Vol. 46. Elsevier, 2015, pp. 1–78.

[45] J. Verdú, H. Zoubi, C. Koller, J. Majer, H. Ritsch, and J. Schmiedmayer. "Strong Magnetic Coupling of an Ultracold Gas to a Superconducting Waveg-uide Cavity". *Physical Review Letters* 103, p. 043603 (2009).

[46] A. Imamoğlu. "Cavity QED Based on Collective Magnetic Dipole Coupling: Spin Ensembles as Hybrid Two-Level Systems". *Physical Review Letters* 102, p. 083602 (2009).

[47] R. H. Dicke. "Coherence in Spontaneous Radiation Processes". *Physical Re-view* 93, pp. 99–110 (1954).

[48] P. Rabl, D. DeMille, J. M. Doyle, M. D. Lukin, R. J. Schoelkopf, and P. Zoller. "Hybrid Quantum Processors: Molecular Ensembles as Quantum Memory for Solid State Circuits". *Physical Review Letters* 97, p. 033003 (2006).

[49] B. Julsgaard and K. Mølmer. "Fundamental limitations in spin-ensemble quantum memories for cavity fields". *Physical Review A* 88, p. 062324 (2013).

[50] W.-l. Song, W.-l. Yang, Z.-q. Yin, C.-y. Chen, and M. Feng. "Controllable quantum dynamics of inhomogeneous nitrogen-vacancy center ensembles coupled to superconducting resonators". *Scientific Reports* 6, p. 33271 (2016).

[51] S. Putz. *Circuit Cavity QED with Macroscopic Solid-State Spin Ensembles*. Springer Theses. Cham: Springer International Publishing, 2017.

[52] R. Houdré, R. P. Stanley, and M. Ilegems. "Vacuum-field Rabi splitting in the presence of inhomogeneous broadening: Resolution of a homogeneous linewidth in an inhomogeneously broadened system". *Physical Review A* 53, pp. 2711–2715 (1996).

[53] Z. Kurucz, J. H. Wesenberg, and K. Mølmer. "Spectroscopic properties of inhomogeneously broadened spin ensembles in a cavity". *Physical Review A* 83, p. 053852 (2011).

[54] I. Diniz, S. Portolan, R. Ferreira, J. M. Gérard, P. Bertet, and A. Auffèves. "Strongly coupling a cavity to inhomogeneous ensembles of emitters: Potential for long-lived solid-state quantum memories". *Physical Review A* 84, p. 063810 (2011).

[55] D. O. Krimer, B. Hartl, and S. Rotter. "Hybrid Quantum Systems with Collectively Coupled Spin States: Suppression of Decoherence through Spectral Hole Burning". *Physical Review Letters* 115, p. 033601 (2015).

[56] S. Putz, A. Angerer, D. O. Krimer, R. Glattauer, W. J. Munro, S. Rotter, J. Schmiedmayer, and J. Majer. "Spectral hole burning and its application in microwave photonics". *Nature Photonics* 11, pp. 36–39 (2017).

[57] K. Debnath, A. H. Kiilerich, A. Benseny, and K. Mølmer. "Coherent spectral hole burning and qubit isolation by stimulated Raman adiabatic passage". *Physical Review A* 100, p. 023813 (2019).

[58] J. L. Rubio, D. Viscor, J. Mompart, and V. Ahufinger. "Atomic-frequency-comb quantum memory via piecewise adiabatic passage". *Physical Review A* 98, p. 043834 (2018).

[59] J. H. Wesenberg, K. Mølmer, L. Rippe, and S. Kröll. "Scalable designs for quantum computing with rare-earth-ion-doped crystals". *Physical Review A* 75, p. 012304 (2007).

[60] N. Ohlsson, R. Krishna Mohan, and S. Kröll. "Quantum computer hardware based on rare-earth-ion-doped inorganic crystals". *Optics Communications* 201, pp. 71–77 (2002).

[61] M. Afzelius, C. Simon, H. de Riedmatten, and N. Gisin. "Multimode quantum memory based on atomic frequency combs". *Physical Review A* 79, p. 052329 (2009).

[62] H. de Riedmatten, M. Afzelius, M. U. Staudt, C. Simon, and N. Gisin. "A solid-state light–matter interface at the single-photon level". *Nature* 456, pp. 773–777 (2008).

[63] C. Laplane, P. Jobez, J. Etesse, N. Timoney, N. Gisin, and M. Afzelius. "Multiplexed on-demand storage of polarization qubits in a crystal". *New Journal of Physics* 18, p. 013006 (2015).

[64] A. Holzäpfel, J. Etesse, K. T. Kaczmarek, A. Tiranov, N. Gisin, and M. Afzelius. "Optical storage for 0.53 s in a solid-state atomic frequency comb memory using dynamical decoupling". *New Journal of Physics* 22, p. 063009 (2020).

[65] P. Jobez, I. Usmani, N. Timoney, C. Laplane, N. Gisin, and M. Afzelius. "Cavity-enhanced storage in an optical spin-wave memory". *New Journal of Physics* 16, p. 083005 (2014).

[66] K. I. Gerasimov, S. A. Moiseev, V. I. Morosov, and R. B. Zaripov. "Room-temperature storage of electromagnetic pulses on a high-finesse natural spin-frequency comb". *Physical Review A* 90, p. 042306 (2014).

[67] N. Sinclair, E. Saglamyurek, H. Mallahzadeh, J. A. Slater, M. George, R. Ricken, M. P. Hedges, D. Oblak, C. Simon, W. Sohler, and W. Tittel. "Spectral Multiplexing for Scalable Quantum Photonics using an Atomic Frequency Comb Quantum Memory and Feed-Forward Control". *Physical Review Letters* 113, p. 053603 (2014).

[68] P. Jobez, N. Timoney, C. Laplane, J. Etesse, A. Ferrier, P. Goldner, N. Gisin, and M. Afzelius. "Towards highly multimode optical quantum memory for quantum repeaters". *Physical Review A* 93, p. 032327 (2016).

[69] C. Grezes, B. Julsgaard, Y. Kubo, M. Stern, T. Umeda, J. Isoya, H. Sumiya, H. Abe, S. Onoda, T. Ohshima, V. Jacques, J. Esteve, D. Vion, D. Esteve, K. Mølmer, and P. Bertet. "Multimode Storage and Retrieval of Microwave Fields in a Spin Ensemble". *Physical Review X* 4, p. 021049 (2014).

[70] E. M. Bradbury. "Nuclear Magnetic Resonance Techniques in Medicine". *Annals of Internal Medicine* 98, p. 514 (1983).

[71] R. W. Darbeau. "Nuclear Magnetic Resonance (NMR) Spectroscopy: A Review and a Look at Its Use as a Probative Tool in Deamination Chemistry". *Applied Spectroscopy Reviews* 41, pp. 401–425 (2006).

[72] M. H. Levitt. *Spin dynamics: basics of nuclear magnetic resonance.* 2nd ed. ISBN: 978-0-470-51117-6. Chichester, England ; Hoboken, NJ: John Wiley & Sons, 2008. 714 pp.

[73] A. Schweiger and G. Jeschke. *Principles of pulse electron paramagnetic resonance.* Oxford, UK ; New York: Oxford University Press, 2001. 578 pp.

[74] A. Bienfait, J. J. Pla, Y. Kubo, M. Stern, X. Zhou, C. C. Lo, C. D. Weis, T. Schenkel, M. L. W. Thewalt, D. Vion, D. Esteve, B. Julsgaard, K. Mølmer, J. J. L. Morton, and P. Bertet. "Reaching the quantum limit of sensitivity in electron spin resonance". *Nature Nanotechnology* 11, pp. 253–257 (2016).

[75] C. Eichler, A. J. Sigillito, S. A. Lyon, and J. R. Petta. "Electron Spin Resonance at the Level of 1 0 4 Spins Using Low Impedance Superconducting Resonators". *Physical Review Letters* 118, p. 037701 (2017).

[76] E. L. Hahn. "Spin Echoes". *Physical Review* 80, pp. 580–594 (1950).

[77] K. Mølmer and Y. Castin. "Monte Carlo wavefunctions in quantum optics". *Quantum and Semiclassical Optics: Journal of the European Optical Society Part B* 8, pp. 49–72 (1996).

[78] H. Carmichael. *Statistical Methods in Quantum Optics 2: Non-Classical Fields.* Berlin: Springer-Verlag, 2008. 540 pp.

[79] J. Huber, P. Kirton, and P. Rabl. "Phase-space methods for simulating the dissipative many-body dynamics of collective spin systems". *SciPost Physics* 10, p. 045 (2021).

[80] W.-M. Zhang, P.-Y. Lo, H.-N. Xiong, M. W.-Y. Tu, and F. Nori. "General Non-Markovian Dynamics of Open Quantum Systems". *Physical Review Letters* 109, p. 170402 (2012).

[81] W.-M. Zhang. "Exact master equation and general non-Markovian dynamics in open quantum systems". *The European Physical Journal Special Topics* 227, pp. 1849–1867 (2019).

[82] D. O. Krimer, M. Zens, and S. Rotter. "Critical phenomena and nonlinear dynamics in a spin ensemble strongly coupled to a cavity. I. Semiclassical approach". *Physical Review A* 100, p. 013855 (2019).

[83] M. Zens, D. O. Krimer, and S. Rotter. "Critical phenomena and nonlinear dynamics in a spin ensemble strongly coupled to a cavity. II. Semiclassical-to-quantum boundary". *Physical Review A* 100, p. 013856 (2019).

[84] D. O. Krimer, M. Zens, S. Putz, and S. Rotter. "Sustained photon pulse revivals from inhomogeneously broadened spin ensembles". *Laser & Photonics Reviews* 10, pp. 1023–1030 (2016).

[85] H. S. Dhar, M. Zens, D. O. Krimer, and S. Rotter. "Variational Renormalization Group for Dissipative Spin-Cavity Systems: Periodic Pulses of Nonclassical Photons from Mesoscopic Spin Ensembles". *Physical Review Letters* 121, p. 133601 (2018).

[86] M. Zens, D. O. Krimer, H. S. Dhar, and S. Rotter. "Periodic cavity state revivals from atomic frequency combs". *arXiv:2107.05919 [quant-ph]*, (2021).

[87] M. O. Scully and M. S. Zubairy. *Quantum optics.* Cambridge New York Melbourne Madrid Cape Town Singapore SãoPaulo Delhi Dubai Tokyo Mexiko City: Cambridge University Press, 1997. 630 pp.

[88] C. Gerry and P. Knight. *Introductory Quantum Optics.* ISBN: 978-0-521-52735-4. Cambridge University Press, 2004.

[89] D. F. Walls and G. J. Milburn. *Quantum Optics.* 2nd. ISBN: 978-3-642-06676-4. Berlin Heidelberg: Springer, 2010. 425 pp.

[90] G. Grynberg, A. Aspect, C. Fabre, and C. Cohen-Tannoudji. *Introduction to Quantum Optics: From the Semi-classical Approach to Quantized Light.* Cambridge University Press, 2010.

[91] U. Hohenester. *Nano and Quantum Optics: An Introduction to Basic Principles and Theory.* Graduate Texts in Physics. Cham: Springer International Publishing, 2020.

[92] M. Tavis and F. W. Cummings. "Exact Solution for an N -Molecule—Radiation-Field Hamiltonian". *Physical Review* 170, pp. 379–384 (1968).

[93] J. Dukelsky, S. Pittel, and G. Sierra. "*Colloquium* : Exactly solvable Richardson-Gaudin models for many-body quantum systems". *Reviews of Modern Physics* 76, pp. 643–662 (2004).

[94] O. Babelon and D. Talalaev. "On the Bethe ansatz for the Jaynes–Cummings–Gaudin model". *Journal of Statistical Mechanics: Theory and Experiment* 2007, P06013–P06013 (2007).

[95] O. Tsyplyatyev, J. von Delft, and D. Loss. "Simplified derivation of the Bethe-ansatz equations for the Dicke model". *Physical Review B* 82, p. 092203 (2010).

[96] W. Pogosov, D. Shapiro, L. Bork, and A. Onishchenko. "Exact solution for the inhomogeneous Dicke model in the canonical ensemble: Thermodynamical limit and finite-size corrections". *Nuclear Physics B* 919, pp. 218–237 (2017).

[97] H.-P. Breuer and F. Petruccione. *The theory of open quantum systems*. Repr. ISBN: 978-0-19-921390-0. Oxford: Clarendon Press, 2010. 613 pp.

[98] H. Carmichael. *Statistical Methods in Quantum Optics 1: Master Equations and Fokker-Planck Equations*. Berlin: Springer-Verlag, 1999.

[99] G. S. Agarwal. *Quantum Optics*. ISBN: 978-1-139-03517-0. Cambridge: Cambridge University Press, 2012.

[100] V. V. Temnov and U. Woggon. "Superradiance and Subradiance in an Inhomogeneously Broadened Ensemble of Two-Level Systems Coupled to a Low-Q Cavity". *Physical Review Letters* 95, p. 243602 (2005).

[101] A. Auffèves, D. Gerace, S. Portolan, A. Drezet, and M. França Santos. "Few emitters in a cavity: from cooperative emission to individualization". *New Journal of Physics* 13, p. 093020 (2011).

[102] A. Dombi, A. Vukics, and P. Domokos. "Optical bistability in strong-coupling cavity QED with a few atoms". *Journal of Physics B: Atomic, Molecular and Optical Physics* 46, p. 224010 (2013).

[103] H. Carmichael, R. Brecha, and P. Rice. "Quantum interference and collapse of the wavefunction in cavity QED". *Optics Communications* 82, pp. 73–79 (1991).

[104] M. Radulaski, K. A. Fischer, and J. Vučković. "Nonclassical Light Generation From III–V and Group-IV Solid-State Cavity Quantum Systems". In: *Advances In Atomic, Molecular, and Optical Physics*. Vol. 66. Elsevier, 2017, pp. 111–179.

[105] R. Sáez-Blázquez, J. Feist, A. I. Fernández-Domínguez, and F. J. García-Vidal. "Enhancing photon correlations through plasmonic strong coupling". *Optica* 4, p. 1363 (2017).

[106] M. A. Armen and H. Mabuchi. "Low-lying bifurcations in cavity quantum electrodynamics". *Physical Review A* 73, p. 063801 (2006).

[107] M. Gegg and M. Richter. "Efficient and exact numerical approach for many multi-level systems in open system CQED". *New Journal of Physics* 18, p. 043037 (2016).

[108] P. Kirton and J. Keeling. "Suppressing and Restoring the Dicke Superradiance Transition by Dephasing and Decay". *Physical Review Letters* 118, p. 123602 (2017).

[109] K. Henschel, J. Majer, J. Schmiedmayer, and H. Ritsch. "Cavity QED with an ultracold ensemble on a chip: Prospects for strong magnetic coupling at finite temperatures". *Physical Review A* 82, p. 033810 (2010).

[110]   H. A. M. Leymann, A. Foerster, and J. Wiersig. "Expectation value based equation-of-motion approach for open quantum systems: A general formalism". *Physical Review B* 89, p. 085308 (2014).

[111]   S. Krämer and H. Ritsch. "Generalized mean-field approach to simulate the dynamics of large open spin ensembles with long range interactions". *The European Physical Journal D* 69, p. 282 (2015).

[112]   M. Sánchez-Barquilla, R. E. F. Silva, and J. Feist. "Cumulant expansion for the treatment of light–matter interactions in arbitrary material structures". *The Journal of Chemical Physics* 152, p. 034108 (2020).

[113]   M. Kira and S. W. Koch. *Semiconductor Quantum Optics*. ISBN: 978-1-139-01692-6. Cambridge: Cambridge University Press, 2011.

[114]   T. Mori. "Exactness of the mean-field dynamics in optical cavity systems". *Journal of Statistical Mechanics: Theory and Experiment* 2013, P06005 (2013).

[115]   H. Primakoff and T. Holstein. "Many-Body Interactions in Atomic and Nuclear Systems". *Physical Review* 55, pp. 1218–1234 (1939).

[116]   R. Bonifacio and G. Preparata. "Coherent Spontaneous Emission". *Physical Review A* 2, pp. 336–347 (1970).

[117]   H. Haken. *Laser theory*. corr. pr. ISBN: 978-0-387-12188-8. Berlin: Springer, 1984. 320 pp.

[118]   A. A. Svidzinsky, X. Zhang, and M. O. Scully. "Quantum versus semiclassical description of light interaction with atomic ensembles: Revision of the Maxwell-Bloch equations and single-photon superradiance". *Physical Review A* 92, p. 013801 (2015).

[119]   B. C. Rose, A. M. Tyryshkin, H. Riemann, N. V. Abrosimov, P. Becker, H.-J. Pohl, M. L. W. Thewalt, K. M. Itoh, and S. A. Lyon. "Coherent Rabi Dynamics of a Superradiant Spin Ensemble in a Microwave Cavity". *Physical Review X* 7, p. 031002 (2017).

[120]   H. M. Gibbs, S. L. McCall, and T. N. C. Venkatesan. "Differential Gain and Bistability Using a Sodium-Filled Fabry-Perot Interferometer". *Physical Review Letters* 36, pp. 1135–1138 (1976).

[121]   R. Bonifacio and L. A. Lugiato. "Optical bistability and cooperative effects in resonance fluorescence". *Physical Review A* 18, pp. 1129–1144 (1978).

[122]   R. Bonifacio and L. A. Lugiato. "Mean field model for absorptive and dispersive bistability with inhomogeneous broadening". *Lettere al Nuovo Cimento* 21, pp. 517–521 (1978).

[123]   L. A. Lugiato. "II Theory of Optical Bistability". In: *Progress in Optics*. Vol. 21. Elsevier, 1984, pp. 69–216.

[124] R. Bonifacio and P. Meystre. "Critical slowing down in optical bistability". *Optics Communications* 29, pp. 131–134 (1979).

[125] W. H. Press, ed. *Numerical recipes: the art of scientific computing.* 3rd ed. ISBN: 978-0-521-70685-8. Cambridge, UK ; New York: Cambridge University Press, 2007. 1235 pp.

[126] R. Sáez-Blázquez, J. Feist, F. J. García-Vidal, and A. I. Fernández-Domínguez. "Photon statistics in collective strong coupling: Nanocavities and microcavities". *Physical Review A* 98, p. 013839 (2018).

[127] R. Trivedi, M. Radulaski, K. A. Fischer, S. Fan, and J. Vučković. "Photon Blockade in Weakly Driven Cavity Quantum Electrodynamics Systems with Many Emitters". *Physical Review Letters* 122, p. 243602 (2019).

[128] F. Jahnke, C. Gies, M. Aßmann, M. Bayer, H. A. M. Leymann, A. Foerster, J. Wiersig, C. Schneider, M. Kamp, and S. Höfling. "Giant photon bunching, superradiant pulse emission and excitation trapping in quantum-dot nanolasers". *Nature Communications* 7, p. 11540 (2016).

[129] A. A. Zhukov, D. S. Shapiro, W. V. Pogosov, and Y. E. Lozovik. "Dynamics of a mesoscopic qubit ensemble coupled to a cavity: Role of collective dark states". *Physical Review A* 96, p. 033804 (2017).

[130] M. Zens. "Cumulant expansion approach to nonlinear dynamics of inhomogeneous ensembles in cavity QED". Diplomarbeit. Vienna: TU Wien, 2016.

[131] R. Kubo. "Generalized Cumulant Expansion Method". *Journal of the Physical Society of Japan* 17, pp. 1100–1120 (1962).

[132] A. Foerster, H. Leymann, and J. Wiersig. "Computer-aided cluster expansion: An efficient algebraic approach for open quantum many-particle systems". *Computer Physics Communications* 212, pp. 210–219 (2017).

[133] J. Feist. *https://github.com/jfeist/QuantumAlgebra.jl.* Version v0.2.0. Nov. 2, 2019.

[134] D. Plankensteiner, C. Hotter, and H. Ritsch. "QuantumCumulants.jl: A Julia framework for generalized mean-field equations in open quantum systems". *arXiv:2105.01657 [quant-ph]*, (2021).

[135] F. Verstraete, V. Murg, and J. Cirac. "Matrix product states, projected entangled pair states, and variational renormalization group methods for quantum spin systems". *Advances in Physics* 57, pp. 143–224 (2008).

[136] U. Schollwöck. "The density-matrix renormalization group in the age of matrix product states". *Annals of Physics* 326, pp. 96–192 (2011).

[137] R. Orús. "A practical introduction to tensor networks: Matrix product states and projected entangled pair states". *Annals of Physics* 349, pp. 117–158 (2014).

[138]   F. Verstraete, J. J. García-Ripoll, and J. I. Cirac. "Matrix Product Density Operators: Simulation of Finite-Temperature and Dissipative Systems". *Physical Review Letters* 93, p. 207204 (2004).

[139]   M. Zwolak and G. Vidal. "Mixed-State Dynamics in One-Dimensional Quantum Lattice Systems: A Time-Dependent Superoperator Renormalization Algorithm". *Physical Review Letters* 93, p. 207205 (2004).

[140]   D. Stanek, C. Raas, and G. S. Uhrig. "Dynamics and decoherence in the central spin model in the low-field limit". *Physical Review B* 88, p. 155305 (2013).

[141]   G. Vidal. "Efficient Classical Simulation of Slightly Entangled Quantum Computations". *Physical Review Letters* 91, p. 147902 (2003).

[142]   G. Vidal. "Efficient Simulation of One-Dimensional Quantum Many-Body Systems". *Physical Review Letters* 93, p. 040502 (2004).

[143]   A. J. Daley, C. Kollath, U. Schollwöck, and G. Vidal. "Time-dependent density-matrix renormalization-group using adaptive effective Hilbert spaces". *Journal of Statistical Mechanics: Theory and Experiment* 2004, P04005 (2004).

[144]   S. R. White and A. E. Feiguin. "Real-Time Evolution Using the Density Matrix Renormalization Group". *Physical Review Letters* 93, p. 076401 (2004).

[145]   J. Prior, A. W. Chin, S. F. Huelga, and M. B. Plenio. "Efficient Simulation of Strong System-Environment Interactions". *Physical Review Letters* 105, p. 050404 (2010).

[146]   F. A. Y. N. Schröder and A. W. Chin. "Simulating open quantum dynamics with time-dependent variational matrix product states: Towards microscopic correlation of environment dynamics and reduced system evolution". *Physical Review B* 93, p. 075105 (2016).

[147]   J. del Pino, F. A. Y. N. Schröder, A. W. Chin, J. Feist, and F. J. Garcia-Vidal. "Tensor Network Simulation of Non-Markovian Dynamics in Organic Polaritons". *Physical Review Letters* 121, p. 227401 (2018).

[148]   D. Manzano. "A short introduction to the Lindblad master equation". *AIP Advances* 10, p. 025106 (2020).

[149]   M. Suzuki. "Fractal decomposition of exponential operators with applications to many-body theories and Monte Carlo simulations". *Physics Letters A* 146, pp. 319–323 (1990).

[150]   A. Datta and G. Vidal. "Role of entanglement and correlations in mixed-state quantum computation". *Physical Review A* 75, p. 042310 (2007).

[151]   M. Vogelsberger, F. Marinacci, P. Torrey, and E. Puchwein. "Cosmological simulations of galaxy formation". *Nature Reviews Physics* 2, pp. 42–66 (2020).

[152] R. A. Granger. *Fluid mechanics*. Dover. Dover classics of science and mathematics. New York: Dover Publications, 1995. 896 pp.

[153] S. Grossberg. "Nonlinear neural networks: Principles, mechanisms, and architectures". *Neural Networks* 1, pp. 17–61 (1988).

[154] D. Chen. "Modeling the Spread of Infectious Diseases: A Review". In: *Analyzing and Modeling Spatial and Temporal Dynamics of Infectious Diseases*. Hoboken, New Jersey: Wiley, 2014.

[155] A. Szöke, V. Daneu, J. Goldhar, and N. A. Kurnit. "Bistable Optical Element and its Application". *Applied Physics Letters* 15, pp. 376–379 (1969).

[156] R. Bonifacio, M. Gronchi, and L. A. Lugiato. "Photon statistics of a bistable absorber". *Physical Review A* 18, p. 2266 (1978).

[157] C. M. Bowden and C. C. Sung. "First- and second-order phase transitions in the Dicke model: Relation to optical bistability". *Physical Review A* 19, pp. 2392–2401 (1979).

[158] F. Ou. "Critical phenomena and phase transitions in optical bistability". *Physical Review A* 41, pp. 3021–3025 (1990).

[159] H. J. Carmichael. "Breakdown of Photon Blockade: A Dissipative Quantum Phase Transition in Zero Dimensions". *Physical Review X* 5, p. 031028 (2015).

[160] G. Rempe, R. J. Thompson, R. J. Brecha, W. D. Lee, and H. J. Kimble. "Optical bistability and photon statistics in cavity quantum electrodynamics". *Physical Review Letters* 67, pp. 1727–1730 (1991).

[161] H. Chang, H. Wu, C. Xie, and H. Wang. "Controlled Shift of Optical Bistability Hysteresis Curve and Storage of Optical Signals in a Four-Level Atomic System". *Physical Review Letters* 93, p. 213901 (2004).

[162] J. A. Sauer, K. M. Fortier, M. S. Chang, C. D. Hamley, and M. S. Chapman. "Cavity QED with optically transported atoms". *Physical Review A* 69, p. 051804 (2004).

[163] V. R. Almeida and M. Lipson. "Optical bistability on a silicon chip". *Optics Letters* 29, p. 2387 (2004).

[164] T. K. Fryett, C. M. Dodson, and A. Majumdar. "Cavity enhanced nonlinear optics for few photon optical bistability". *Optics Express* 23, p. 16246 (2015).

[165] L. Zhang, L. Zhan, M. Qin, Z. Zou, Z. Wang, and J. Liu. "Large-region tunable optical bistability in saturable absorber-based single-frequency Brillouin fiber lasers". *Journal of the Optical Society of America B* 32, p. 1113 (2015).

[166] J. M. Fink, A. Dombi, A. Vukics, A. Wallraff, and P. Domokos. "Observation of the Photon-Blockade Breakdown Phase Transition". *Physical Review X* 7, p. 011012 (2017).

[167] L. A. Lugiato, F. Prati, and M. Brambilla. *Nonlinear optical systems*. ISBN: 978-1-107-06267-2. Cambridge, United Kingdom: Cambridge University Press, 2015. 454 pp.

[168] A. Angerer. "Non-linear Dynamics in Cavity QED: Beyond Two Coupled Springs". PhD thesis. Vienna: TU Wien, 2019.

[169] M. Soljačić, M. Ibanescu, S. G. Johnson, Y. Fink, and J. D. Joannopoulos. "Optimal bistable switching in nonlinear photonic crystals". *Phys. Rev. E* 66, Publisher: American Physical Society, p. 055601 (2002).

[170] M. Ono, M. Hata, M. Tsunekawa, K. Nozaki, H. Sumikura, H. Chiba, and M. Notomi. "Ultrafast and energy-efficient all-optical switching with graphene-loaded deep-subwavelength plasmonic waveguides". *Nature Photonics* 14, pp. 37–43 (2020).

[171] C. W. Gardiner and M. J. Collett. "Input and output in damped quantum systems: Quantum stochastic differential equations and the master equation". *Physical Review A* 31, pp. 3761–3774 (1985).

[172] D. Walls and G. J. Milburn. "Input–Output Formulation of Optical Cavities". In: *Quantum Optics*. Ed. by D. Walls and G. J. Milburn. Berlin, Heidelberg: Springer Berlin Heidelberg, 2008, pp. 127–141.

[173] G. Agrawal and H. Carmichael. "Inhomogeneous Broadening and the Mean-field Approximation for Optical Bistability in a Fabry-Perot Interferometer". *Optica Acta: International Journal of Optics* 27, pp. 651–660 (1980).

[174] E. Abraham and S. Hassan. "Effects of inhomogeneous broadening on optical bistability in a fabry-perot cavity". *Optics Communications* 35, pp. 291–297 (1980).

[175] F. Jelezko and J. Wrachtrup. "Single defect centres in diamond: A review". *physica status solidi (a)* 203, pp. 3207–3225 (2006).

[176] M. W. Doherty, N. B. Manson, P. Delaney, F. Jelezko, J. Wrachtrup, and L. C. Hollenberg. "The nitrogen-vacancy colour centre in diamond". *Physics Reports* 528, pp. 1–45 (2013).

[177] M. V. G. Dutt, L. Childress, L. Jiang, E. Togan, J. Maze, F. Jelezko, A. S. Zibrov, P. R. Hemmer, and M. D. Lukin. "Quantum Register Based on Individual Electronic and Nuclear Spin Qubits in Diamond". *Science* 316, pp. 1312–1316 (2007).

[178] C. Santori, P. E. Barclay, K.-M. C. Fu, R. G. Beausoleil, S. Spillane, and M. Fisch. "Nanophotonics for quantum optics using nitrogen-vacancy centers in diamond". *Nanotechnology* 21, p. 274008 (2010).

[179] C. E. Bradley, J. Randall, M. H. Abobeih, R. C. Berrevoets, M. J. Degen, M. A. Bakker, M. Markham, D. J. Twitchen, and T. H. Taminiau. "A Ten-Qubit Solid-State Spin Register with Quantum Memory up to One Minute". *Physical Review X* 9, p. 031045 (2019).

[180] J. Zhang, S. S. Hegde, and D. Suter. "Efficient Implementation of a Quantum Algorithm in a Single Nitrogen-Vacancy Center of Diamond". *Physical Review Letters* 125, p. 030501 (2020).

[181] J. Wrachtrup and F. Jelezko. "Processing quantum information in diamond". *Journal of Physics: Condensed Matter* 18, S807–S824 (2006).

[182] S. Pezzagna and J. Meijer. "Quantum computer based on color centers in diamond". *Applied Physics Reviews* 8, p. 011308 (2021).

[183] G. Balasubramanian, I. Y. Chan, R. Kolesov, M. Al-Hmoud, J. Tisler, C. Shin, C. Kim, A. Wojcik, P. R. Hemmer, A. Krueger, T. Hanke, A. Leitenstorfer, R. Bratschitsch, F. Jelezko, and J. Wrachtrup. "Nanoscale imaging magnetometry with diamond spins under ambient conditions". *Nature* 455, pp. 648–651 (2008).

[184] J. R. Maze, P. L. Stanwix, J. S. Hodges, S. Hong, J. M. Taylor, P. Cappellaro, L. Jiang, M. V. G. Dutt, E. Togan, A. S. Zibrov, A. Yacoby, R. L. Walsworth, and M. D. Lukin. "Nanoscale magnetic sensing with an individual electronic spin in diamond". *Nature* 455, pp. 644–647 (2008).

[185] C. L. Degen. "Scanning magnetic field microscope with a diamond single-spin sensor". *Applied Physics Letters* 92, p. 243111 (2008).

[186] J. M. Taylor, P. Cappellaro, L. Childress, L. Jiang, D. Budker, P. R. Hemmer, A. Yacoby, R. Walsworth, and M. D. Lukin. "High-sensitivity diamond magnetometer with nanoscale resolution". *Nature Physics* 4, pp. 810–816 (2008).

[187] G. Balasubramanian, P. Neumann, D. Twitchen, M. Markham, R. Kolesov, N. Mizuochi, J. Isoya, J. Achard, J. Beck, J. Tissler, V. Jacques, P. R. Hemmer, F. Jelezko, and J. Wrachtrup. "Ultralong spin coherence time in isotopically engineered diamond". *Nature Materials* 8, pp. 383–387 (2009).

[188] N. Zhao, J.-L. Hu, S.-W. Ho, J. T. K. Wan, and R. B. Liu. "Atomic-scale magnetometry of distant nuclear spin clusters via nitrogen-vacancy spin in diamond". *Nature Nanotechnology* 6, pp. 242–246 (2011).

[189] V. S. Perunicic, C. D. Hill, L. T. Hall, and L. Hollenberg. "A quantum spin-probe molecular microscope". *Nature Communications* 7, p. 12667 (2016).

[190] M. H. Abobeih, J. Randall, C. E. Bradley, H. P. Bartling, M. A. Bakker, M. J. Degen, M. Markham, D. J. Twitchen, and T. H. Taminiau. "Atomic-scale imaging of a 27-nuclear-spin cluster using a quantum sensor". *Nature* 576, pp. 411–415 (2019).

[191] S. Schmitt, T. Gefen, D. Louzon, C. Osterkamp, N. Staudenmaier, J. Lang, M. Markham, A. Retzker, L. P. McGuinness, and F. Jelezko. "Optimal frequency measurements with quantum probes". *npj Quantum Information* 7, p. 55 (2021).

[192] A. Jarmola, V. M. Acosta, K. Jensen, S. Chemerisov, and D. Budker. "Temperature- and Magnetic-Field-Dependent Longitudinal Spin Relaxation in Nitrogen-Vacancy Ensembles in Diamond". *Physical Review Letters* 108, p. 197601 (2012).

[193] N. Bar-Gill, L. Pham, A. Jarmola, D. Budker, and R. Walsworth. "Solid-state electronic spin coherence time approaching one second". *Nature Communications* 4, p. 1743 (2013).

[194] C. Tsallis, S. V. F. Levy, A. M. C. Souza, and R. Maynard. "Statistical-Mechanical Foundation of the Ubiquity of Lévy Distributions in Nature". *Physical Review Letters* 75, pp. 3589–3593 (1995).

[195] D. Prato and C. Tsallis. "Nonextensive foundation of Lévy distributions". *Physical Review E* 60, pp. 2398–2401 (1999).

[196] Y. Kubo, C. Grezes, A. Dewes, T. Umeda, J. Isoya, H. Sumiya, N. Morishita, H. Abe, S. Onoda, T. Ohshima, V. Jacques, A. Dréau, J.-F. Roch, I. Diniz, A. Auffeves, D. Vion, D. Esteve, and P. Bertet. "Hybrid Quantum Circuit with a Superconducting Qubit Coupled to a Spin Ensemble". *Physical Review Letters* 107, p. 220501 (2011).

[197] S. H. Strogatz. *Nonlinear dynamics and chaos: with applications to physics, biology, chemistry, and engineering.* Second edition. ISBN: 978-0-8133-4910-7. Boulder, CO: Westview Press, a member of the Perseus Books Group, 2015. 513 pp.

[198] L. A. Lugiato, P. Mandel, and L. M. Narducci. "Adiabatic elimination in nonlinear dynamical systems". *Physical Review A* 29, pp. 1438–1452 (1984).

[199] P. D. Drummond and D. F. Walls. "Quantum theory of optical bistability. II. Atomic fluorescence in a high- Q cavity". *Physical Review A* 23, pp. 2563–2579 (1981).

[200] S. Barbarino, A. Gozzini, F. Maccarrone, I. Longo, and R. Stampacchia. "Critical slowing-down in microwave absorptive bistability". *Il Nuovo Cimento B* 71, pp. 183–195 (1982).

[201] C. Kuehn. "Scaling of saddle-node bifurcations: degeneracies and rapid quantitative changes". *Journal of Physics A: Mathematical and Theoretical* 42, p. 045101 (2009).

[202] M. Vojta. "Quantum phase transitions". *Reports on Progress in Physics* 66, pp. 2069–2110 (2003).

[203] W. Casteels, R. Fazio, and C. Ciuti. "Critical dynamical properties of a first-order dissipative phase transition". *Physical Review A* 95, p. 012128 (2017).

[204] C. Clausen, I. Usmani, F. Bussières, N. Sangouard, M. Afzelius, H. de Riedmatten, and N. Gisin. "Quantum storage of photonic entanglement in a crystal". *Nature* 469, pp. 508–511 (2011).

[205] E. Saglamyurek, N. Sinclair, J. Jin, J. A. Slater, D. Oblak, F. Bussières, M. George, R. Ricken, W. Sohler, and W. Tittel. "Broadband waveguide quantum memory for entangled photons". *Nature* 469, pp. 512–515 (2011).

[206] N. Maring, P. Farrera, K. Kutluer, M. Mazzera, G. Heinze, and H. de Riedmatten. "Photonic quantum state transfer between a cold atomic gas and a crystal". *Nature* 551, pp. 485–488 (2017).

[207] J. H. Davidson, P. Lefebvre, J. Zhang, D. Oblak, and W. Tittel. "Improved light-matter interaction for storage of quantum states of light in a thulium-doped crystal cavity". *Physical Review A* 101, p. 042333 (2020).

[208] M. Afzelius and C. Simon. "Impedance-matched cavity quantum memory". *Physical Review A* 82, p. 022310 (2010).

[209] S. A. Moiseev, S. N. Andrianov, and F. F. Gubaidullin. "Efficient multimode quantum memory based on photon echo in an optimal QED cavity". *Physical Review A* 82, p. 022311 (2010).

[210] M. Sabooni, Q. Li, S. Kröll, and L. Rippe. "Efficient Quantum Memory Using a Weakly Absorbing Sample". *Physical Review Letters* 110, p. 133604 (2013).

[211] X. Zhang, C.-L. Zou, N. Zhu, F. Marquardt, L. Jiang, and H. X. Tang. "Magnon dark modes and gradient memory". *Nature Communications* 6, p. 8914 (2015).

[212] D. O. Krimer, M. Liertzer, S. Rotter, and H. E. Türeci. "Route from spontaneous decay to complex multimode dynamics in cavity QED". *Physical Review A* 89, p. 033820 (2014).

[213] M. U. Staudt, S. R. Hastings-Simon, M. Nilsson, M. Afzelius, V. Scarani, R. Ricken, H. Suche, W. Sohler, W. Tittel, and N. Gisin. "Fidelity of an Optical Memory Based on Stimulated Photon Echoes". *Physical Review Letters* 98, p. 113601 (2007).

[214] K. Holliday, M. Croci, E. Vauthey, and U. P. Wild. "Spectral hole burning and holography in an Y 2 SiO 5 : Pr 3 + crystal". *Physical Review B* 47, pp. 14741–14752 (1993).

[215] K. Naoe, L. G. Zimin, and Y. Masumoto. "Persistent spectral hole burning in semiconductor nanocrystals". *Physical Review B* 50, pp. 18200–18210 (1994).

[216] G. P. Teja, C. Simon, and S. K. Goyal. "Photonic quantum memory using an intra-atomic frequency comb". *Physical Review A* 99, p. 052314 (2019).

[217] B. T. H. Varcoe, S. Brattke, M. Weidinger, and H. Walther. "Preparing pure photon number states of the radiation field". *Nature* 403, pp. 743–746 (2000).

[218] Z. Leghtas, G. Kirchmair, B. Vlastakis, R. J. Schoelkopf, M. H. Devoret, and M. Mirrahimi. "Hardware-Efficient Autonomous Quantum Memory Protection". *Physical Review Letters* 111, p. 120501 (2013).

[219] B. Vlastakis, G. Kirchmair, Z. Leghtas, S. E. Nigg, L. Frunzio, S. M. Girvin, M. Mirrahimi, M. H. Devoret, and R. J. Schoelkopf. "Deterministically Encoding Quantum Information Using 100-Photon Schrodinger Cat States". *Science* 342, pp. 607–610 (2013).

[220] M. Mirrahimi. "Cat-qubits for quantum computation". *Comptes Rendus Physique* 17, pp. 778–787 (2016).

[221] J. M. Gertler, B. Baker, J. Li, S. Shirol, J. Koch, and C. Wang. "Protecting a bosonic qubit with autonomous quantum error correction". *Nature* 590, pp. 243–248 (2021).

[222] M. H. Michael, M. Silveri, R. T. Brierley, V. V. Albert, J. Salmilehto, L. Jiang, and S. M. Girvin. "New Class of Quantum Error-Correcting Codes for a Bosonic Mode". *Physical Review X* 6, p. 031006 (2016).

[223] L. Hu, Y. Ma, W. Cai, X. Mu, Y. Xu, W. Wang, Y. Wu, H. Wang, Y. P. Song, C.-L. Zou, S. M. Girvin, L.-M. Duan, and L. Sun. "Quantum error correction and universal gate set operation on a binomial bosonic logical qubit". *Nature Physics* 15, pp. 503–508 (2019).

[224] D. Gottesman, A. Kitaev, and J. Preskill. "Encoding a qubit in an oscillator". *Physical Review A* 64, p. 012310 (2001).

[225] P. Campagne-Ibarcq, A. Eickbusch, S. Touzard, E. Zalys-Geller, N. E. Frattini, V. V. Sivak, P. Reinhold, S. Puri, S. Shankar, R. J. Schoelkopf, L. Frunzio, M. Mirrahimi, and M. H. Devoret. "Quantum error correction of a qubit encoded in grid states of an oscillator". *Nature* 584, pp. 368–372 (2020).

[226] T. C. Ralph, A. Gilchrist, G. J. Milburn, W. J. Munro, and S. Glancy. "Quantum computation with optical coherent states". *Physical Review A* 68, p. 042319 (2003).

[227]   S. van Enk and O. Hirota. "Entangled coherent states: Teleportation and decoherence". *Physical Review A* 64, p. 022313 (2001).

[228]   W. J. Munro, K. Nemoto, G. J. Milburn, and S. L. Braunstein. "Weak-force detection with superposed coherent states". *Physical Review A* 66, p. 023819 (2002).

[229]   L. Mandel and E. Wolf. *Optical coherence and quantum optics*. Repr. with corr. Cambridge: Cambridge University Press, 2008. 1166 pp.

[230]   M. A. Hemminga and L. J. Berliner, eds. *ESR spectroscopy in membrane biophysics*. Biological magnetic resonance. New York: Springer, 2007. 379 pp.

[231]   M. Drescher, G. Jeschke, and E. Bordignon, eds. *EPR spectroscopy: applications in chemistry and biology*. Topics in current chemistry. ISBN: 978-3-642-28346-8. Heidelberg: Springer, 2012. 237 pp.

[232]   K. Debnath, G. Dold, J. J. L. Morton, and K. Mølmer. "Self-Stimulated Pulse Echo Trains from Inhomogeneously Broadened Spin Ensembles". *Physical Review Letters* 125, p. 137702 (2020).

[233]   S. Weichselbaumer. "Spin dynamics in strongly coupled spin-photon hybrid systems". Dissertation. Munich: Technische Universität München, 2020.

[234]   E. Zavoisky. "Paramagnetic Relaxation of Liquid Solution for Perpendicular Fields". *J. Phys. U. S. S. R.* 9, 211p (1945).

[235]   T. Prisner, M. Rohrer, and F. MacMillan. "Pulsed EPR Spectroscopy: Biological Applications". *Annual Review of Physical Chemistry* 52, pp. 279–313 (2001).

[236]   S. S. Eaton and G. R. Eaton. "Multifrequency Pulsed EPR and the Characterization of Molecular Dynamics". In: *Methods in Enzymology*. Vol. 563. Elsevier, 2015, pp. 37–58.

[237]   P. G. Baranov, H. J. von Bardeleben, F. Jelezko, and J. Wrachtrup. *Magnetic Resonance of Semiconductors and Their Nanostructures: Basic and Advanced Applications*. Vol. 253. Springer Series in Materials Science. Vienna: Springer Vienna, 2017.

[238]   R. Schirhagl, K. Chang, M. Loretz, and C. L. Degen. "Nitrogen-Vacancy Centers in Diamond: Nanoscale Sensors for Physics and Biology". *Annual Review of Physical Chemistry* 65, pp. 83–105 (2014).

[239]   F. A. Zwanenburg, A. S. Dzurak, A. Morello, M. Y. Simmons, L. C. L. Hollenberg, G. Klimeck, S. Rogge, S. N. Coppersmith, and M. A. Eriksson. "Silicon quantum electronics". *Reviews of Modern Physics* 85, pp. 961–1019 (2013).

[240]   M. H. Devoret and R. J. Schoelkopf. "Superconducting Circuits for Quantum Information: An Outlook". *Science* 339, pp. 1169–1174 (2013).

[241]   J. J. L. Morton, A. M. Tyryshkin, R. M. Brown, S. Shankar, B. W. Lovett, A. Ardavan, T. Schenkel, E. E. Haller, J. W. Ager, and S. A. Lyon. "Solid-state quantum memory using the 31P nuclear spin". *Nature* 455, pp. 1085–1088 (2008).

[242]   C. Grezes, Y. Kubo, B. Julsgaard, T. Umeda, J. Isoya, H. Sumiya, H. Abe, S. Onoda, T. Ohshima, K. Nakamura, I. Diniz, A. Auffeves, V. Jacques, J.-F. Roch, D. Vion, D. Esteve, K. Moelmer, and P. Bertet. "Towards a spin-ensemble quantum memory for superconducting qubits". *Comptes Rendus Physique* 17, pp. 693–704 (2016).

[243]   S. Probst, F. B. Song, P. A. Bushev, A. V. Ustinov, and M. Weides. "Efficient and robust analysis of complex scattering data under noise in microwave resonators". *Review of Scientific Instruments* 86, p. 024706 (2015).

[244]   E. H. Poindexter, P. J. Caplan, B. E. Deal, and R. R. Razouk. "Interface states and electron spin resonance centers in thermally oxidized (111) and (100) silicon wafers". *Journal of Applied Physics* 52, pp. 879–884 (1981).

[245]   A. Stesmans and V. V. Afanas'ev. "Electron spin resonance features of interface defects in thermal (100)Si/SiO2". *Journal of Applied Physics* 83, pp. 2449–2457 (1998).

[246]   G. Feher, R. C. Fletcher, and E. A. Gere. "Exchange Effects in Spin Resonance of Impurity Atoms in Silicon". *Physical Review* 100, pp. 1784–1786 (1955).

[247]   D. Jérome and J. M. Winter. "Electron Spin Resonance on Interacting Donors in Silicon". *Physical Review* 134, A1001–A1007 (1964).

[248]   K. Morigaki and S. Maekawa. "Electron Spin Resonance Studies of Interacting Donor Clusters in Phosphorus-Doped Silicon". *Journal of the Physical Society of Japan* 32, pp. 462–471 (1972).

[249]   S. Shankar, A. M. Tyryshkin, and S. A. Lyon. "ESR measurements of phosphorus dimers in isotopically enriched Si 28 silicon". *Physical Review B* 91, p. 245206 (2015).

[250]   B. C. Hall. *Lie Groups, Lie Algebras, and Representations*. Vol. 222. Graduate Texts in Mathematics. Cham: Springer International Publishing, 2015.

[251]   L. Lugiato, F. Prati, and M. Brambilla. "The adiabatic elimination principle". In: *Nonlinear Optical Systems*. Cambridge University Press, 2015, pp. 105–111.

[252]   K. F. Riley, M. P. Hobson, and S. J. Bence. *Mathematical methods for physics and engineering*. 3rd. ISBN: 978-0-521-67971-8. Cambridge ; New York: Cambridge University Press, 2006. 1333 pp.

Acknowledgments

Above all, however, this work would not have been possible without the help of many people whom I would like to thank explicitly in the following:

- I am sincerely grateful to Stefan Rotter, who enabled me to work on the problems that are now the topic of this thesis. He put a lot of trust in me and allowed me to pursue my studies in the field of quantum optics very independently while always being available when support was needed. His immense professional skills and drive for scientific excellence have sharpened my understanding of what it takes to be successful in science.

- My deepest gratitude goes to Dmitry Krimer. He mentored and supported me not only during his time at TU Wien but also afterward, in addition to new professional challenges. His kind guidance through the first years of my scientific development has left a lasting impression on me. He taught me how to work scientifically and thoroughly, from which I can benefit for the rest of my life.

- Himadri Dhar, during his brief stay as a post-doc in our group, developed the variational renormalization group method, which laid the foundation for many results presented in this thesis. Being one of the kindest persons I have ever worked with, he has not only deepened my understanding of physics but also broadened my cultural horizon.

- Physics without experiments would be much easier but meaningless. Therefore, I would like to thank all experimentalists for their collaboration and contributions to our joint publications. Especially I thank Andreas Angerer,

Curriculum vitae

Personal data

Name:	Dipl.-Ing. Matthias Zens
Address:	Schelleingasse 26/3/21, 1040 Vienna
Date of birth:	19.03.1989
Place of birth:	Wr. Neustadt, Austria
Nationality:	Austrian
Mobile number:	+43 650 3551942
E-mail-address:	matthias.zens@gmail.com

Education

since Oct. 2016   Vienna University of Technology (TU Wien), Institute for Theoretical Physics
Doctoral programme in Engineering Sciences: Technical Physics

Advisor:	Stefan Rotter, web: https://rottergroup.itp.tuwien.ac.at
PhD thesis:	Cavity QED with Spin Ensembles: From the Semiclassical to the Quantum Regime

2012 – 2016   Vienna University of Technology (TU Wien), Institute for Theoretical Physics
Master of Science (Dipl.-Ing.) in Technical Physics
Graduation with distinction (19.09.2016)

Advisor:	Stefan Rotter
Diploma thesis:	Cumulant Expansion Approach to Nonlinear Dynamics of Inhomogeneous Enembles in Cavity QED

2008 – 2012   Vienna University of Technology (TU Wien), Atomic and Subatomic Physics
Bachelor of Science in Technical Physics
Graduation (23.04.2012)

Advisor:	Thorsten Schumm
Bachelor thesis:	Atomic clocks and quantum metrology

1999 – 2007   **High school**, BRG Gröhrmühlgasse, Wr. Neustadt, Austria
Graduation (19.06.2007)   Scientific focus

Work experience

since Sept. 2017   **University assistant (Pre-Doc.)**, Institute for Theoretical Physics
TU Wien, Lecturer in the exercise classes Quantum Mechanics I & II

Aug.– Oct. 2019   **Guest researcher**, Institute for Theoretical Atomic Molecular and Optical Physics, Harvard-Smithsonian Center for Astrophysics, MA 02138, USA

2016 – 2017   **Project assistant**, Institute for Theoretical Physics, TU Wien

2014 – 2016   **Teaching assistant**, Institute for Theoretical Physics, TU Wien
Tutor in Quantum Mechanics I & II

Jan.– Sept. 2008   **Paramedic**, Red Cross
Community service, Pernitz, Austria

120

Awards and additional information

Best talk award (2nd prize) at the International Student Workshop on Quantum Technologies (ISWQT, Shanghai, China, 2019)

Participation in the high-potential-program for students of the Vienna University of Technology (IBM Austria, Infineon Technologies, 2013/14)

Ph.D. grant within the special research program "Next Generation Light Synthesis and Interaction" of the Austrian Science Fund (2016 – 2017)

Participation in the doctoral school "Complex Quantum Systems" (CoQuS) of the Austrian Science Fund (2017 – 2021)

Scientific contributions

7 scientific publication in peer-reviewed journals (including 2 as first author) in *Science Advances, Laser & Photonics Reviews, Physical Review Letters,* and *Physical Review A*
1 invited News & Views article in *Nature Photonics* - see List of Publications

8 contributed talks and 5 poster presentations at national and international conferences, summer schools, and seminar series (USA, China, Russia, Italy, Spain, Germany, Austria)

Conferences and summer schools

Oct. 31, 2019	**Conference**, poster presentation, *"Austrian Quantum Information Conference 2019"*, Vienna, Austria
Oct. 28 – 30, 2019	**Conference**, invited talk, *"Vienna Graduate Conference on Complex Quantum Systems 2019"*, Vienna, Austria
Oct. 02, 2019	**Seminar**, contributed talk (student talk), *"Joint Quantum Science Seminar Harvard"*, Cambridge, USA
Sept. 16 – 17, 2019	**Workshop**, participation, *"ITAMP LabCosmo Workshop: AMO techniques for cosmology"*, Cambridge, USA
May 23 – 24, 2019	**Conference**, contributed talk, *"Polaron Day 2019"*, Vienna, Austria
May 05 – 09, 2019	**Workshop**, contributed talk and poster presentation, *"International Student Workshop on Quantum Technologies (ISWQT)"*, Shanghai, China
Apr. 01, 2019	**Seminar**, contributed talk, *"Colloquium on Complex Quantum Systems (CoQuS)"*, Vienna, Austria
Oct. 09 – 12, 2018	**Conference**, contributed talk, *"Nigmatullin's Readings - 2018"*, Kazan, Russia
Sept. 17 – 21, 2018	**Conference**, poster presentation, *"International Conference for Young Quantum Information Scientists (YQIS)"*, Vienna, Austria
Mar. 26 – 29, 2018	**Conference**, poster presentation, *"Novel Paradigms in Many-Body Physics from Open Quantum Systems"*, Dresden, Germany

Sept. 18 – 22, 2017	**Summer school**, contributed talk, *"Summer School on Complex Quantum Systems (CoQuS)"*, Vienna, Austria
Sept. 12 – 15, 2017	**Conference**, contributed talk, *"10th Italian conference on Quantum Information Science"*, Florence, Italy
Sept. 12 – 16, 2016	**Summer school**, participation, *"Summer School on Complex Quantum Systems (CoQuS)"*, Vienna, Austria

Programming skills

Python:	advanced
Fortran:	advanced
C/C++:	basic knowledge
Mathematica:	basic knowledge
Matlab:	basic knowledge

Languages

German:	native speaker
English:	fluent

Interests and abilities

Training as paramedic, emergency vehicle driver, and lifeguard

Voluntary work:	paramedic for the Red Cross Pernitz (2008-2010)
Sports:	tennis (club level), running, indoor bouldering
Reading:	scientific literature, biographies, realist novels

Board games